Algorithms for Multiphase Motion with Applications to Materials Science

by

Matthew R. Elsey

A dissertation submitted in partial fulfillment
of the requirements for the degree of
Doctor of Philosophy
(Applied and Interdisciplinary Mathematics)
in the University of Michigan
2011

Doctoral Committee:

Associate Professor Selim Esedoḡlu, Co-Chair
Associate Professor Wei Lu, Co-Chair
Professor Robert Krasny
Professor Peter S. Smereka

ACKNOWLEDGEMENTS

First and foremost, thank you to my primary mentors and collaborators, Professors Selim Esedoḡlu and Peter Smereka. You have given me opportunities to learn, travel, speak, write, and work that I could not have imagined when I began this process. Thank you for developing my interest in level set-type techniques for interface motions and for allowing and encouraging me to work primarily on the algorithmic and numerical aspects of the problem that interest me most. I will always be grateful for your continual help and for the time you spent shaping me as an applied mathematician.

Thank you also to the rest of my committee, co-advisor Professor Wei Lu, and Professor Robert Krasny. You always responded quickly whenever I asked, even though you were not involved in the day-to-day business of this project. I have valued your opinions and your broader view on my work, and hope to continue our association in the future.

Thank you to the Admissions Committee for (belatedly) accepting me into the Applied and Interdisciplinary Mathematics program even though I was an undergraduate here at the University of Michigan, as well. I think that I have made the most of my nine years in Ann Arbor, and I trust that you do not regret your decision! Special thanks are due to Professor Smadar Karni for encouraging the committee to do the "right" thing.

I am grateful for financial support received from the National Science Foundation,

the Society for Industrial and Applied Mathematics, and from the Rackham Predoctoral Fellowship. This support has allowed me to attend numerous conferences and workshops, and freed me from other responsibilities, allowing me to focus on my research.

Finally, my most heartfelt thanks go out to my family and friends. Few of you know exactly what I do or why I do it, but you always support me anyhow. I consider myself extremely fortunate to have known so many great people with extraordinarily bright futures in many different fields. Special thanks go out to those of you who know the meaning of "Court 2," "Friday Ball," or "Cowboy Up." The times that we have had and the memories that we have made are priceless to me.

TABLE OF CONTENTS

LIST OF FIGURES

Figure

LIST OF TABLES

Table

LIST OF ALGORITHMS

Algorithm

CHAPTER I

Introduction

The primary goal of this work is to describe and utilize a class of implicit algorithms that are collectively known as the "distance function-based diffusion-generated motion" (DFDGM) algorithms. These algorithms simulate the evolution of multiple phases $\Sigma_k \subseteq \Omega$ under a class of evolution laws for the motion by curvature of the interfaces $\Gamma_{k\ell}$ separating phases Σ_k and Σ_ℓ by normal velocities of the form:

$$v_n(\Gamma_{k\ell}) = f_{k\ell}(\kappa_{k\ell}), \tag{1.1}$$

where $v_n(\Gamma_{k\ell})$ denotes the outward normal velocity from phase Σ_k into phase Σ_ℓ, the $f_{k\ell}$ are affine functions, and $\kappa_{k\ell}$ denotes the mean curvature of the interface $\Gamma_{k\ell}$. It is required that $\bigcup_k \Sigma_k = \Omega$, and that

$$\Sigma_k \cap \Sigma_\ell = \partial\Sigma_k \cap \partial\Sigma_\ell = \Gamma_{k\ell} \tag{1.2}$$

for all $k \neq \ell$. As a natural consequence, we must have that $v_n(\Gamma_{k\ell}) = -v_n(\Gamma_{\ell k})$. This condition prevents vaccuums (regions where no phases are present) and overlaps (regions where multiple phases are present).

The simplest, yet still mathematically interesting case, of (1.1) is pure multiphase motion by curvature,

$$v_n(\Gamma_{k\ell}) = \kappa_{k\ell}, \tag{1.3}$$

where each point p on the interface $\Gamma_{k\ell}$ moves with normal velocity equal to the curvature of the interface at the point p. This normal velocity arises as L_2 gradient descent for the energy

$$E = \frac{1}{2}\sum_k |\partial\Sigma_k|, \tag{1.4}$$

where $|\partial\Sigma_k|$ denotes the length of $\partial\Sigma_k$ in two dimensions, and the surface area of $\partial\Sigma_k$ in three dimensions. This energy corresponds to the total interface length (surface area, in three dimensions) of the system, with the factor of $1/2$ arising due to the double-counting of each interface. This energy arises as the model for isotropic grain growth, a materials science phenomenon arising when polycrystalline materials are annealed. This application is discussed in Chapter III.

Gradient descent for (1.4) defines a natural boundary condition, known as the Herring boundary condition [36] at triple junctions. In this simplest setting, symmetry dictates that the interior angle of each phase at a triple junction (along a triple line, in three dimensions) must be $120°$.

The addition of a bulk term to the normal velocity for pure curvature motion (1.3) leads to a new model,

$$v_n(\Gamma_{k\ell}) = \kappa_{k\ell} + \lambda(e_\ell - e_k), \tag{1.5}$$

where λ sets the scaling between terms, and the e_k are arbitrary constants assigned to each Σ_k. The velocity (1.5) arises as gradient descent for the energy

$$E = \frac{1}{2}\sum_k |\partial\Sigma_k| + \lambda\sum_k e_k|\Sigma_k|, \tag{1.6}$$

where $|\Sigma_k|$ denotes the area of the set Σ_k in two dimensions, and volume in three dimensions. (1.5) and (1.6) arise as a simple model for the recrystallization of polycrystalline materials. See Chapter IV for a full discussion of the model and simulation results obtained using a DFDGM algorithm.

The final case that we consider is that of unequal surface tensions: we associate with each interface $\Gamma_{k\ell}$ a constant surface tension $\gamma_{k\ell}$:

$$v_n(\Gamma_{k\ell}) = \gamma_{k\ell}\kappa_{k\ell}. \tag{1.7}$$

This more general form arises as gradient descent for a slightly different form of energy,

$$E = \sum_k \sum_{\ell \neq k} \gamma_{k\ell} |\Gamma_{k\ell}|, \tag{1.8}$$

where $|\Gamma_{k\ell}|$ denotes the length of the interface in two dimensions, and the surface area in three dimensions. This is a more (though not completely) general description for grain growth than (1.3) and (1.4). Numerical results demonstrating the accuracy and consistency of the DFDGM algorithm for a special case of this motion are presented in Section 2.3.2.

The natural Herring boundary conditions [36] arising from gradient descent for the energy (1.8) state that the forces at a triple junction must vanish. These conditions may be represented either in terms of the tangent vectors $T_{k\ell}$ emanating along the interfaces from the triple junction,

$$\gamma_{12}T_{12} + \gamma_{13}T_{13} + \gamma_{23}T_{23} = 0, \tag{1.9}$$

or, equivalently, in terms of the opening angles θ_k of the phases at the triple junction,

$$\frac{\sin(\theta_1)}{\gamma_{23}} = \frac{\sin(\theta_2)}{\gamma_{13}} = \frac{\sin(\theta_3)}{\gamma_{12}}. \tag{1.10}$$

See Figure 1.1 for a visualization. A condition on the choice of the $\gamma_{k\ell}$ is that

$$\gamma_{jk} + \gamma_{j\ell} > \gamma_{k\ell}, \tag{1.11}$$

for all $j \neq k \neq \ell$, to ensure that it is not energetically beneficial to laminate any $\Gamma_{k\ell}$ interface with a thin layer of Σ_j.

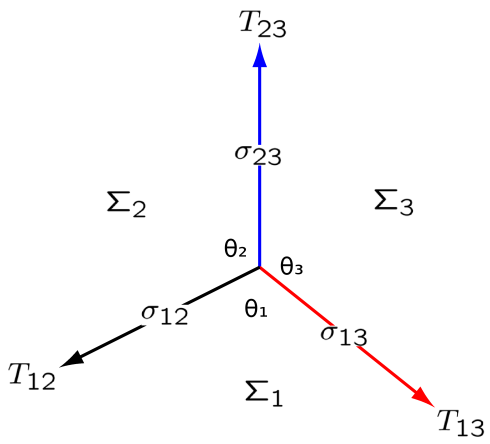

Figure 1.1: A zoom-in on a triple junction. The Herring angle conditions specify that the forces at the triple junction must vanish (1.9), and, equivalently, dictates the angles θ_k.

1.1 Related Algorithms

The remainder of this section will introduce a variety of algorithms used for the simulation of motions of the type given by (1.1). We also indicate some of the benefits and drawbacks of each. Three of these, the phase field method, the threshold dynamics scheme, and the level set method, are precursors to the DFDGM family of algorithms, and will thus be described in greater detail.

We will discuss several of these approaches in the context of pure two-phase curvature motion, using this notation: Let Σ be a connected subset of the domain Ω. In this case, gradient descent for the energy

$$E = |\partial\Sigma| \tag{1.12}$$

gives the normal velocity for the interface $\Gamma = \partial\Sigma$ as

$$v(\Gamma) = \kappa. \tag{1.13}$$

Finally, we introduce the DFDGM algorithm of [22] for motion by pure curvature (1.13) and multiphase motion by curvature (1.3). Chapter II will introduce algorithms for motion by (1.5) and (1.7).

1.1.1 Front Tracking

Front tracking methods directly discretize a parameterization of the interface $\Gamma_{k\ell}$. This parametrization can also be interpreted as representing the interface by a collection of points, such as the vertices of a polygon in the plane or a triangulated surface in three dimensions. The evolution of the interface is then computed by approximating curvature and a normal direction from this discretization. These techniques have been used to simulate multiphase mean curvature motion in both two [45, 48] and three [48, 87] dimensions. A major advantage of these techniques is computational efficiency, as computational resources are all devoted to the interface region. The fundamental difficulty inherent to this approach is managing the topological changes that abound in multiphase motions. With explicit representations of the interface, it is difficult to determine if curves (in two dimensions) or surfaces (in three dimensions) intersect.

In the case of pure two-phase curvature motion in two dimensions, Grayson's Theorem [34] states that any smooth curve evolves without developing singularities and shrinks to a point in finite time. Thus topological changes are not a concern in this setting, and front tracking methods may be appropriate. Even for two-dimensional mean curvature multiphase motion, it is expected (though not fully proven, see [55]) that interfaces interact only through junction–junction collisions. If this conjecture is true, explicitly checking for and handling topological changes may be manageable in this case. However, no such condition is expected to hold in three dimensions. Even for pure two-phase curvature motion in three dimensions, a smooth initial surface may develop singularities. For example, the well-known "dumbbell" example (see Figure 1.2) splits into two pieces under curvature motion. Moreover, under related models including additional driving forces, other topological

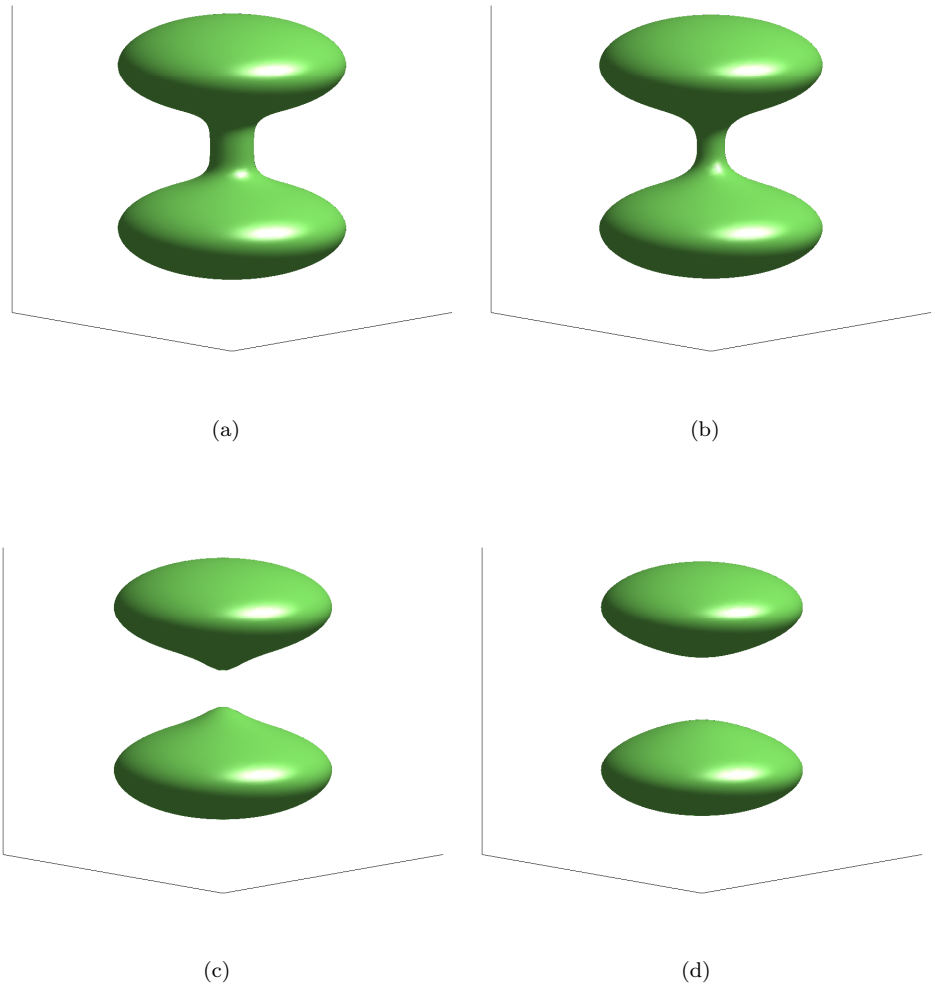

Figure 1.2: The "dumbbell" splits into two pieces under pure curvature motion.

changes (for example, two smooth curves meeting away from triple junctions) become commonplace. The recrystallization model of Srolovitz, et al. [79, 80], introduced in Section 2.2 and carefully studied in Chapter IV, is an important example of such a model. These events are difficult to handle using explicit techniques.

The "dumbbell" example is somewhat contrived; however, topological changes occur naturally and frequently in multiphase motions, as well (see Figure 1.3 for an example). Due to these difficulties, we choose to restrict our further attention to

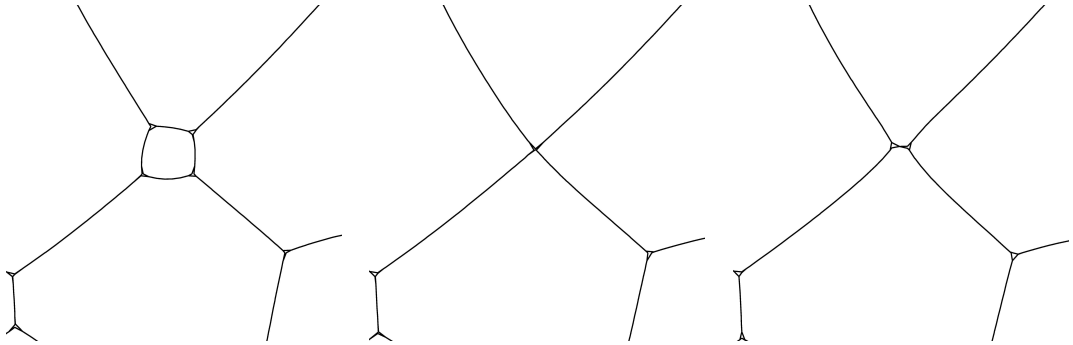

Figure 1.3: The collision of triple junctions and the disappearance of a phase are more easily handled by implicit methods.

methods that represent interfaces implicitly.

1.1.2 Monte Carlo

The basic idea of Monte Carlo methods is simple. For a complete introduction in the context of microstructural evolution in materials, the reader is referred to [43]. First, a state, s, is assigned to each location on a discrete grid, and a discrete energy, E, approximating the continuum energy of interest is defined. Grid locations are randomly chosen one at a time, the change in energy ΔE resulting from changing the state of that grid location is computed, and the state change is accepted with a probability determined by the change in energy.

As an example, consider the energy (1.6). In a Monte Carlo framework on a uniform square grid with spacing Δx, the states could be defined by

$$s_i = k \quad \Leftrightarrow \quad x_i \in \Sigma_k, \tag{1.14}$$

and the discretized approximating energy by

$$E(s) = \sum_i \sum_j^{N(i)} \frac{\Delta x}{2} J(s_i, s_j) \left(1 - \delta(s_i, s_j)\right) + \sum_i H(s_i) \Delta x^2, \tag{1.15}$$

where i indexes all grid locations, $N(i)$ is defined to be the 1–neighborhood of grid location i, and δ denotes the Kronecker delta function. The first term incurs a

penalty equal to $J(s_i, s_j)$ times the length of a grid cell, if neighboring cells i and j have different states (note that the factor of $1/2$ accounts for double-counting), while the second term penalizes $H(s_i)$ times the area of a grid cell. Choosing

$$H(s_i) = \lambda e_k \quad \Leftrightarrow \quad s_i = k, \tag{1.16}$$

and setting $J(s_i, s_j) = 1$ completes the analogy with (1.6).

The Metropolis probability transition function is commonly used, and is defined by

$$\mathbb{P}(\Delta E) = \begin{cases} 1 & \text{if } \Delta E \leq 0, \\ e^{\frac{-\Delta E}{kT}} & \text{if } \Delta E > 0. \end{cases} \tag{1.17}$$

Here, kT is interpreted as a simulation "temperature." The "zero-temperature" limit of this transition function allows transitions only if $\Delta E \leq 0$, and is commonly used to speed up simulations by disallowing state changes which increase the system energy.

Monte Carlo algorithms are simple to implement, and allow for the approximation of very complex energies if states are defined appropriately. However, they are extremely slow and lack sub-grid accuracy. Furthermore, the stochastic nature of the Monte Carlo evolution ensures that some type of averaging is needed to approximate the true continuum motion. For example, the evolution of a simple circle by mean curvature is very difficult to capture accurately using Monte Carlo methods even on a well-resolved grid. Beyond these significant accuracy concerns, it is also difficult to connect the Monte Carlo method with some notion of "real" time beyond reorientation attempts. These algorithms are probably most appropriate for physical simulations where the grid spacing is on the order of atomic spacing. Other limitations of Monte Carlo methods in the context of applications such as grain growth and recrystallization are discussed in Sections 4.3.2 and 4.4.

1.1.3 Phase Field

Modica and Mortola [61, 62] considered the energy

$$E(u) = \int_\Omega \left(\varepsilon |\nabla u|^2 + \frac{1}{\varepsilon} W(u) \right) dx, \tag{1.18}$$

where $W(u)$ is a double-well potential, for example, $W(u) = u^2(u-1)^2$. Then, if the set Σ is defined by $\Sigma = \{x : u(x) \geq 1/2\}$, Modica and Mortola demonstrated that (1.18) converges, up to a constant factor, to (1.12) as $\varepsilon \to 0^+$. Gradient descent for (1.18) in L^2 is the Allen–Cahn equation [2]:

$$u_t = \Delta u - \frac{1}{\varepsilon^2} W'(u). \tag{1.19}$$

Similar equations arise in the multiphase case, where the energy is given by

$$E(\vec{u}) = \sum_k \varepsilon |\nabla u_k|^2 + \frac{1}{\varepsilon} W(\vec{u}) dx, \tag{1.20}$$

with gradient descent given by

$$(u_k)_t = \Delta u_k - \frac{1}{\varepsilon^2} \frac{\partial W}{\partial u_k}. \tag{1.21}$$

In this case, the set $\Sigma_k \approx \{x : u_k(x) > 1/2\}$. The penalty term is often of the form $W(u) = \prod_k \|\vec{u} - \vec{e}_k\|$, where $\vec{u} = (u_1, \ldots, u_k)$, so that $W(u) = 0$ if and only if exactly one $u_k = 1$ and the rest are equal to zero.

The phase field technique has been used extensively in simulations of curvature motion [24, 30, 47, 51, 81]. However, there are two major difficulties with numerical implementations of the evolution described by the PDEs (1.19) and (1.21). First, the ε^2 scaling of the two terms makes the problems stiff: Small time steps must be taken due to the coefficient on the $W'(u)$ term, but the motion of the interface is driven by the slow dynamics of the first term. Second, the interface Γ is represented by a diffuse transition region, in which u changes values from one minimum of W to

another. The width of this region is proportional to ε, and this transition layer must be well-resolved to allow for accurate numerics. For example, Kim, et al. [47] report that at least six grid points are needed in the transition layer to achieve acceptable accuracy. Therefore, a phase needs to be on the order of at least 25 grid points across to be moderately well-resolved.

In contrast, we demonstrate in Section 2.1.3 that we can simulate evolutions quite accurately with phases of approximately ten grid points in each direction, and that we can track them down to half that length with only a few percent relative error via the DFDGM algorithms. Though there is no rigorous notion of generalized solutions with uniqueness through topological changes, we also perform a convergence study there showing that our simulations track grains through topological changes quite consistently as well. The large grain size requirement imposed by the phase field model is a serious impediment to performing very large-scale simulations.

1.1.4 Threshold Dynamics

The threshold dynamics schemes were introduced by Merriman, Bence, and Osher [59, 60] to alleviate some of the difficulties inherent in phase field algorithms. They can be viewed as time-splitting algorithms for the phase field PDEs (1.19) and (1.21). In the two-phase case, one could alternate two steps: (1) evolution by the heat equation $u_t = \Delta u$ and (2) pointwise gradient descent $u_t = \frac{1}{\varepsilon^2} W'(u)$. Efficient and accurate methods are known for solving (1). Furthermore, in the limit $\varepsilon \to 0^+$, the solution to (2) is simple for any fixed $t > 0$:

$$u(x,t) = \begin{cases} 1 & \text{if } u(x,0) > \frac{1}{2}, \\ 0 & \text{if } u(x,0) < \frac{1}{2}. \end{cases} \tag{1.22}$$

Input: $u^0(x) = \mathbf{1}_{\Sigma^0(x)}$, discrete time step Δt, and number of time steps $j_{\max}$.
Output: $\Sigma^j = \{x : u^j(x) = 1\}$, for $j = 1, \ldots, j_{\max}$.

For: $j = 1, \ldots, j_{\max}$, do steps 1–2.

1. Convolve: Let $u(x, \Delta t)$ be the solution of $u_t = \Delta u$, $u(x, 0) = u^j(x)$, at time Δt.
2. Threshold: Set
$$u^j(x) = \begin{cases} 1 & \text{if } u(x, \Delta t) > \frac{1}{2}, \\ 0 & \text{otherwise.} \end{cases}$$

Algorithm 1.1: Threshold Dynamics for two-phase curvature motion.

Input: $u_k^0(x) = \mathbf{1}_{\Sigma_k^0(x)}$, for $k = 1, \ldots, k_{\max}$, discrete time step Δt, and number of time steps $j_{\max}$.
Output: $\Sigma_k^j = \{x : u_k^j(x) = 1\}$, for $k = 1, \ldots, k_{\max}$ and $j = 1, \ldots, j_{\max}$.

For: $j = 1, \ldots, j_{\max}$, do steps 1–2 for $k = 1, \ldots, k_{\max}$

1. Convolve: Let $u_k(x, \Delta t)$ be the solution of $u_t = \Delta u$, $u(x, 0) = u_k^j(x)$, at time Δt.
2. Threshold: Set
$$u_k^j(x) = \begin{cases} 1 & \text{if } u_k(x, \Delta t) = \max_\ell u_\ell(x, \Delta t), \\ 0 & \text{otherwise.} \end{cases}$$

Algorithm 1.2: Threshold Dynamics for multiphase curvature motion.

These results suggest the scheme of Algorithm 1.1, which approximates the evolution of an input set Σ^0 by mean curvature motion (1.13).

Algorithm 1.1 has a very simple extension to the multiphase case, described in Algorithm 1.2. In this case, let the domain Ω be partitioned into an initial set of phases Σ_k^0. Then Algorithm 1.2 describes the threshold dynamics evolution for the normal velocity (1.3). The extension is obviously equivalent to Algorithm 1.1 in the two-phase case, and is shown in [57] to generate the correct, symmetric angles at triple junctions.

The threshold dynamics scheme is unconditionally stable, so that accuracy is the only concern in choosing the size of the time step Δt. It is also fast, with only $O(M \log M)$ complexity, where M is the total number of grid points used ($M = m^N$

for a square grid with m grid points in each direction in N dimensions). As with the phase field method, the interfaces $\Gamma_{k\ell}$ are implicitly represented. This allows for changes in topology (which occur frequently in the multiphase evolution) to be handled naturally, a major advantage over front tracking-type techniques.

However, the threshold dynamics algorithm has many notable drawbacks, as well. It is quite inaccurate on uniform grids. Also, if the time step is small with respect to grid resolution Δx, $\Delta t \approx (\Delta x)^2$, the interface will not be able to move. This is due to the represention $u(x) = \mathbf{1}_{\Sigma(x)}$. As u is 0 or 1 at each grid point at the beginning of each time step, it is not possible to interpolate to locate the interface with any subgrid resolution. Ruuth explored threshold dynamics on non-uniform, adaptively refined grids [73] to alleviate these problems; however, it is much easier to work on uniform grids. The Fast Fourier Transform can be applied to perform convolution on uniform grids easily, but the extension to non-uniform grids is nontrivial. Esedoḡlu, Ruuth, and Tsai proposed a new algorithm that replaced the characteristic function by the signed distance function to allow for interpolation with subgrid accuracy [22]. This method is described in Section 1.2.

1.1.5 Level Sets

Level set methods are popular for interface motion problems. For any two-phase interface motion problem, one can define a level set function ϕ with the property that

$$\phi(x) > 0 \quad \Leftrightarrow \quad x \in \Sigma. \tag{1.23}$$

The zero-level set of ϕ coincides with the boundary $\partial\Sigma$. Then basic level set theory explains that the solution $\phi(x,t)$ of the partial differential equation

$$\phi_t = v_n|\nabla\phi|, \tag{1.24}$$

with the initial condition

$$\phi(x,0) = \phi_0(x), \tag{1.25}$$

where $\phi_0(x)$ corresponds to an initial interface Γ_0, gives the evolution of the interface Γ under normal velocity v_n.

For a level set function, curvature is simply the divergence of the outward-pointing unit normal vector,

$$\kappa = -\nabla \cdot \left(\frac{\nabla \phi}{|\nabla \phi|} \right), \tag{1.26}$$

where the negative sign arises as a consequence of the chosen sign convention. Thus (1.24)–(1.26) provide a simple prescription for a level sets algorithm for two-phase motion by curvature. Topological changes are again handled naturally.

In the multiphase case, the sets Σ_k can each be represented by level set functions ϕ_k, and the evolution can be constrained so that exactly one ϕ_k is positive away from interfaces. Zhao et al. [96] present an implementation of the level sets method for multiphase motion of the form (1.1). However, in this work, the condition that exactly one ϕ_k is positive at every spatial location is imposed as a pointwise constraint, which leads to stiffness. The DFDGM algorithms are also closely related to level set techniques but resolve this problem.

1.2 Distance Function-Based Diffusion-Generated Motion

The distance function-based diffusion-generated motion (DFDGM) algorithm for two-phase curvature motion was originally proposed by Esedoḡlu, Ruuth, and Tsai [22]. It can be thought of as either a modification of the threshold dynamics algorithm or of the level set method for motion by curvature.

The major hallmark of the DFDGM algorithms is their reliance on the signed

Input: Signed distance function d^0 to $\partial\Sigma^0$, discrete time step size Δt, and number of time steps $j_{\max}$.
Output: Signed distance functions d^j, for $j = 1, \ldots, j_{\max}$.

For: $j = 1, \ldots, j_{\max}$, do steps 1–2.

1. CONVOLVE: Compute $A(x) := K_{\Delta t} * d^{j-1}$, where $K_{\Delta t}$ is

$$K_{\Delta t} = G_{\Delta t} \qquad \text{or} \qquad K_{\Delta t} = \frac{1}{4}\left(4G_{\frac{3}{2}\Delta t} - G_{3\Delta t}\right),$$

   and $G_{\Delta t}$ is the fundamental solution of the heat equation:

$$G_{\Delta t}(x) = \frac{1}{(4\pi\Delta t)^{\frac{N}{2}}} e^{-\frac{|x|^2}{4\Delta t}}.$$

2. REDISTANCE: Set $d^j(x)$ to be the signed distance function to the zero-level set of $A(x)$.

Algorithm 1.3: DFDGM of [22] for two-phase curvature motion.

distance function $d_\Sigma(x)$, defined by

$$d_\Sigma(x) = \begin{cases} dist(x, \Sigma^c) & \text{if } x \in \Sigma, \\ -dist(x, \Sigma) & \text{if } x \in \Sigma^c, \end{cases} \tag{1.27}$$

where $dist(x, S) = \inf_{y \in S}|x - y|$.

The two-phase algorithm is simple. Similar to threshold dynamics, two operations are alternated: Convolution of the signed distance function with a radially symmetric kernel, and a redistancing operation which reconstructs the signed distance to the zero-level set of the convolution output. See Algorithm 1.3 for details.

The signed distance function may be thought of as a particular type of level set function, with the restriction that $d_\Sigma(x)$ satisfies the eikonal equation,

$$|\nabla d_\Sigma| = 1, \tag{1.28}$$

everywhere that the gradient of d_Σ is well-defined. Indeed, the basic equations for curvature motion in the level set framework, (1.24) and (1.26), reduce to the heat equation, $\phi_t = \Delta\phi$ in the case that $|\nabla\phi| = 1$. Convolution of $\phi(x, 0)$ with the

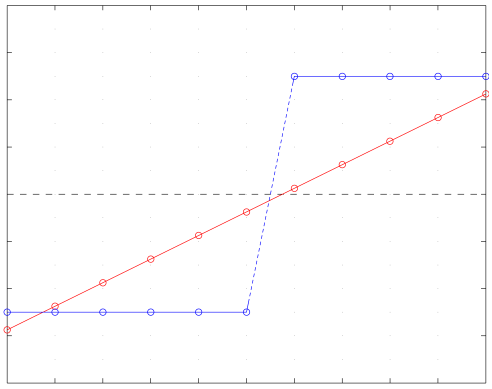

Figure 1.4: The function $\left(\mathbf{1}_\Sigma - \frac{1}{2}\right)$ (blue) provides no subgrid information about the location of the interface. In one dimension, the signed distance function (d_Σ)(red) can be interpolated to exactly capture the interface location.

fundamental solution of the heat equation, $G_{\Delta t}$, gives the solution to (1.28), $\phi(x, \Delta t)$. Then, the second step of Algorithm 1.3 generates the signed distance function to the zero-level set of this new solution.

The DFDGM algorithm is also quite similar to the threshold dynamics algorithm. The characteristic functions of threshold dynamics are replaced by the signed distance function. The second step of Algorithms 1.1 and 1.3 serve the same purpose: Return the convolution outputs to the form needed as input to the next step (a characteristic function and a signed distance function, respectively), while preserving the location of the interface. The major improvement of the DFDGM algorithms over threshold dynamics algorithms is the additional subgrid accuracy attainable with the signed distance function, as shown in Figure 1.4.

The extension of the DFDGM algorithm to multiphase motion by mean curvature (1.3) was also proposed in [22], and is reproduced for completeness as Algorithm 1.4. The following notation is used: Let the domain Ω be partitioned into an initial set of phases Σ_k^0, $k = 0, \ldots, k_{\max}$. The set of points contained in the kth phase at time $t = j\Delta t$ will be denoted as Σ_k^j. The signed distance function to the boundary $\partial\Sigma_k^j$ is

Input: Signed distance functions d_k^0, for $k = 1, \ldots, k_{\max}$,
discrete time step size Δt, and number of time steps $j_{\max}$.
Output: Signed distance functions d_k^j, for $k = 1, \ldots, k_{\max}$ and $j = 1, \ldots, j_{\max}$.

For: $j = 1, \ldots, j_{\max}$, do steps 1–3 for $k = 1, \ldots, k_{\max}$.

1. CONVOLVE: Compute $A_k(x) := K_{\Delta t} * d_k^{j-1}$, where $K_{\Delta t}$ is

$$K_{\Delta t} = G_{\Delta t} \qquad \text{or} \qquad K_{\Delta t} = \frac{1}{4}\left(4G_{\frac{3}{2}\Delta t} - G_{3\Delta t}\right),$$

   and $G_{\Delta t}$ is the fundamental solution of the heat equation:

$$G_{\Delta t}(x) = \frac{1}{(4\pi\Delta t)^{\frac{N}{2}}} e^{-\frac{|x|^2}{4\Delta t}}.$$

2. REDISTRIBUTE: Construct $B_k(x) = (A_k(x) - \max_{\ell \neq k} A_\ell(x))/2$ to remove overlaps and vacuums from the previous step.

3. REDISTANCE: Set $d_k^j(x)$ to be the signed distance function to the zero-level set of $B_k(x)$.

Algorithm 1.4: DFDGM of [22] for multiphase curvature motion.

denoted as d_k^j. Full details are provided in Section 2.1.

The evolution generated by Algorithm 1.4 can be shown to generate motion by mean curvature along smooth interfaces and to enforce the symmetric Herring angle condition at triple junctions in two dimensions (and hence also along triple lines in three dimensions) [22]. The key results are summarized here for completeness.

1.2.1 Consistency along Smooth Interfaces

Let $\Gamma = \partial\Sigma$ be smooth, and rotate and translate Σ so that Γ crosses the origin and may be locally described by a function $g(x)$ with $g'(0) = 0$, as in Figure 1.5 Then $d_\Sigma(x, y)$ may be expressed in terms of the curvature κ and its derivatives by the expansion:

$$\begin{aligned} d_\Sigma(x,y) =& y + \frac{1}{2}\kappa(0)x^2 + \frac{1}{6}\kappa_x(0)x^3 - \frac{1}{2}\kappa^2(0)x^2 y \\ &+ \frac{1}{24}\left(\kappa_{xx}(0) - 3\kappa^3(0)\right)x^4 - \frac{1}{2}\kappa(0)\kappa_x(0)x^3 y + \frac{1}{2}\kappa^3(0)x^2y^2 \\ &+ O\left((\sqrt{x^2+y^2})^5\right). \end{aligned} \tag{1.29}$$

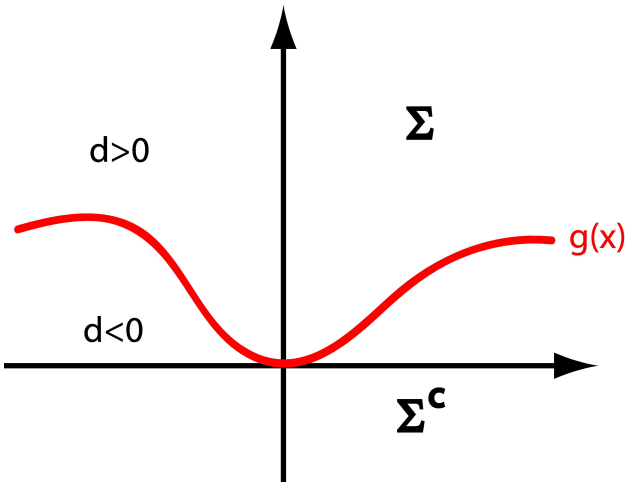

Figure 1.5: Setup for smooth interface consistency check.

The expansion (1.29) is convolved with the Gaussian

$$G_t(x,y) = \frac{1}{4\pi t} e^{-\frac{x^2+y^2}{4t}} \tag{1.30}$$

to obtain

$$(d_\Sigma * G_t)(0,y) = y + \kappa(0)t - \kappa^2(0)yt + \frac{1}{2}\left(\kappa_{xx}(0) + \kappa^3(0)\right)t^2 + O(t^3), \tag{1.31}$$

for $y = O(t)$, demonstrating that the normal velocity of the interface at $(0,0)$ is $v_n = \kappa(0) + O(t)$. Thus Algorithms 1.3 and 1.4 are expected to be first-order accurate in time. Versions of Algorithm 1.3 with higher-order accuracy in time are also presented in [22].

1.2.2 Consistency at Triple Junctions

Let three C^2 curves meet at a triple point at the origin. In a small neighborhood of the origin, these curves will appear to determine three sectors, as shown in Figure 1.6. An explicit formula for the signed distance to a sector S defined by

$$S = \left\{(x,y) : y < \tan\left(\frac{3\pi}{2} - \theta\right) \text{ and } y < \tan\left(\frac{3\pi}{2} + \theta\right)x\right\} \tag{1.32}$$

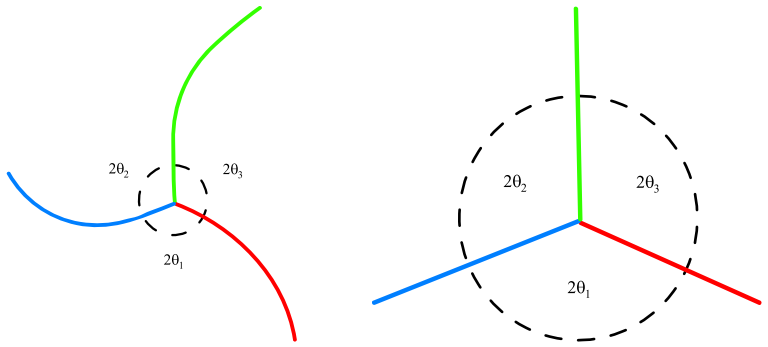

(a) (b)

Figure 1.6: A triple junction (a) looks like the meeting of three sectors (b) in a small neighborhood of the junction.

is given by

$$d_\Sigma(x,y) = \begin{cases} -x\cos\theta - y\sin\theta & \text{if } x \geq 0 \text{ and } y \leq x\tan\theta, \\ x\cos\theta - y\sin\theta & \text{if } x \leq 0 \text{ and } y \leq -x\tan\theta, \\ -\sqrt{x^2+y^2} & \text{if } y \geq |x|\tan\theta. \end{cases} \tag{1.33}$$

The convolution of (1.33) with (1.30) results in

$$\begin{aligned} (d_\Sigma * G_t)(x,y) =& \frac{\sqrt{t}}{\pi}\left(\theta - \frac{\pi}{2} - \cos\theta\right) \\ &+ \frac{1}{2\pi}\left(4\cos^3\theta - \pi\sin\theta - 2\theta\sin\theta - 6\cos\theta\right) y \\ &+ \frac{1}{\sqrt{t}}\frac{1}{16\sqrt{\pi}}\left(2\theta - 4\cos\theta - \sin 2\theta - \pi\right) x^2 \\ &+ \frac{1}{\sqrt{t}}\frac{1}{16\sqrt{\pi}}\left(\sin 2\theta + 2\theta - \pi\right) y^2 + O\left(\frac{\sqrt{x^2+y^2}^3}{t}\right). \end{aligned} \tag{1.34}$$

This expansion can be rotated appropriately for each sector of Figure 1.6, and leads to the following observations, made in [22]:

- If $\theta_1 = \theta_2 = \theta_3 = \frac{\pi}{3}$, then the triple junction moves with speed at most $O(1)$ in a time step of size Δt.

- If $|\theta_j - \frac{\pi}{3}| = O(1)$ for any $j \in \{1, 2, 3\}$, then the triple junction moves with speed at least $O(\Delta t^{-\frac{1}{2}})$ in a time step of size Δt.

Furthermore, the authors define the mapping T such that

$$T \begin{pmatrix} \theta_1 \\ \theta_2 \end{pmatrix} = \begin{pmatrix} \bar{\theta}_1 \\ \bar{\theta}_2 \end{pmatrix}, \tag{1.35}$$

where (θ_1, θ_2) are the angles of the sectors input to a single step of Algorithm 1.4, and $(\bar{\theta}_1, \bar{\theta}_2)$ are the resulting angles, and observe that

$$T \begin{pmatrix} \pi/3 \\ \pi/3 \end{pmatrix} = \begin{pmatrix} \pi/3 \\ \pi/3 \end{pmatrix} + O(\sqrt{\Delta t}), \tag{1.36}$$

and

$$(DT) \begin{pmatrix} \pi/3 \\ \pi/3 \end{pmatrix} \approx \begin{pmatrix} -0.31 & 0 \\ 0 & -0.31 \end{pmatrix}, \tag{1.37}$$

so the mapping T is a contraction about $(\pi/3, \pi/3)^T$. Thus Algorithm 1.4 imposes the natural Herring angle conditions at triple junctions with $O(\sqrt{\Delta t})$ error.

1.3 Summary

The DFDGM algorithm presented in Section 1.2 constitutes the basis for the new work presented in this thesis, much of which has been published as [19–21] or is currently in preparation for submission. Chapter II will introduce extensions and modifications of this basic algorithm allowing for more general motions of the form 1.1. Chapters III and IV demonstrate applications of the algorithms to materials science, for the simulation of grain growth and recrystallization.

CHAPTER II

Distance Function-Based Diffusion-Generated Motion Algorithms

The original DFDGM algorithm of Esedoḡlu, Ruuth, and Tsai [22] is presented in Section 1.2. Here, the algorithm is significantly refined and extended. It is made appropriate for many-phase (hundreds of thousands of phases) simulations of pure curvature motion, and extended to more general velocities of the form (1.1). These new algorithms and numerical tests verifying the accuracy and suggesting the convergence of the algorithms to certain known solutions are presented here.

2.1 Algorithm for Many-Phase Pure Curvature Motion

Algorithm 1.4 uses one distance function per phase. The first improvement to the algorithm proposed in this work stems from the observation that a single phase can contain many connected components. Rather than maintaining two phases for spatially separated components, we can maintain both — or many — components in a single phase. Furthermore, if we demand that only components which are sufficiently far apart share the same phase, component mergings will not occur, and potential interactions that could occur during the convolution step will be negligible.

2.1.1 Algorithm

The first extension of Algorithm 1.4 is for the same motion, but allows the use of the same distance function for multiple phases. This improvement allows for simulations containing over 100,000 components initially to be performed using only a limited number of distance functions. Empirically, we observe that 32 signed distance functions in two dimensions and 64 in three dimensions are more than sufficient; however, the algorithm can introduce new signed distance functions as necessary. The setting for this algorithm is slightly different than the previous one. We begin with n_0 components Σ_ℓ^0 for $\ell = 1, \ldots, n_0$, but initialize only $k_{\max}$ signed distance functions, d_k^0 with $k = 1, \ldots, k_{\max}$, where $k_{\max} \leq n_0$. These d_k^0 have the property that they are the signed distance function for a collection of disjoint components, and the union of these collections consists of all the components. As the algorithm proceeds, it must check to be sure that this disjointness property is maintained. If it appears that it is about to fail (i.e. two distinct components in one of the collections become too close), various components will need to be reassigned to different distance functions and if need be a new distance function will be introduced. We call this operation *swapping*. A crucial point is that $k_{\max} \ll n_0$ unless one considers some pathological initial conditions. Even then, since the evolutions considered here are regularizing with a preference towards components with small isoperimetric ratios, $k_{\max}$ is expected and observed to be fairly small at subsequent times during the evolution.

The computational complexity of Algorithm 2.1 is formally $O(k_{\max} M \log M)$, where $k_{\max}$ is the number of level set functions used, and M is the total number of grid points in each set. For a single signed distance function, both the convolution step and the redistancing operation are $O(M \log M)$. The algorithm is second-order

Input: Signed distance functions d_k^0 to $\partial\Sigma_k^0$, for $k = 1, \ldots, k_{\max}$, discrete time step Δt, and number of time steps $j_{\max}$.
Output: Signed distance functions d_k^j, for $k = 1, \ldots, k_{\max}$ and $j = 1, \ldots, j_{\max}$.

For: $j = 1, \ldots, j_{\max}$, do steps 1–4 for $k = 1, \ldots, k_{\max}$.

1. Convolve: Compute $A_k(x) := K_{\Delta t} * d_k^{j-1}$, where $K_{\Delta t}$ is

$$K_{\Delta t} = G_{\Delta t} \qquad \text{or} \qquad K_{\Delta t} = \frac{1}{4}\left(4G_{\frac{3}{2}\Delta t} - G_{3\Delta t}\right),$$

   and $G_{\Delta t}$ is the fundamental solution of the heat equation:

$$G_{\Delta t}(x) = \frac{1}{(4\pi\Delta t)^{\frac{N}{2}}} e^{-\frac{|x|^2}{4\Delta t}}.$$

2. Redistribute: Construct $B_k(x) = (A_k(x) - \max_{\ell \neq k} A_\ell(x))/2$ to remove overlaps and vacuums from the previous step.

3. Redistance: Set $C_k(x)$ to be the signed distance function to the zero-level set of $B_k(x)$.

4. Swap: If necessary swap appropriate components between signed distance functions $C_k(x)$ to ensure that all the components associated to given signed distance function remain well separated. Redistance around swapped components and denote the resulting signed distance functions as d_k^j.

Algorithm 2.1: DFDGM for multiphase curvature motion with swapping.

accurate in space and first-order accurate in time away from triple points. At triple points, analysis and experiment in [22] suggest that the error is $O(\sqrt{\Delta t})$.

2.1.2 Details

We now describe the steps of the above algorithm in more detail in the fully discrete setting. For convenience, the formulas are written down in the 2D setting, but extend trivially to all dimensions.

Convolution

We define the convolution kernels $G_{\Delta t}$ and $K_{\Delta t}$ in terms of the space–discretized solution to the heat equation $u_t = u_{xx} + u_{yy}$. Suppose the grid discretizes $[0, 1]^2$, with equal grid spacing ($\Delta x = \Delta y$). Let $u_{i,j}(t)$ be the space–discretized approximation to

$u(x, y, t)$ at $(i\Delta x, j\Delta y, t)$. Using centered differencing in space, we obtain:

$$\frac{d}{dt}u_{i,j}(t) = \frac{1}{\Delta x^2}\left((u_{i+1,j} - 2u_{i,j} + u_{i-1,j}) + (u_{i,j+1} - 2u_{i,j} + u_{i,j-1})\right). \tag{2.1}$$

Apply the discrete Fourier transform in space to obtain,

$$\frac{d}{dt}\widehat{u}_{r,s} = \frac{2}{\Delta x^2}\left(\cos(2\pi s\Delta x) + \cos(2\pi r\Delta x) - 2\right)\widehat{u}_{r,s}. \tag{2.2}$$

Given initial data $\widehat{u}_{r,s}(t)$, this ODE has solution $\widehat{u}_{r,s}(t + \Delta t)$

$$\widehat{u}_{r,s}(t + \Delta t) = \widehat{u}_{r,s}(t)\exp\left(\frac{-2\Delta t}{\Delta x^2}(2 - \cos(2\pi r\Delta x) - \cos(2\pi s\Delta x))\right). \tag{2.3}$$

Therefore the discrete heat equation (2.1) has solution $u_{i,j}(t + \Delta t) = u_{i,j} * (G_{\Delta t})_{i,j}$ where $*$ denotes the discrete convolution and $(G_{\Delta t})_{i,j}$ is defined via its discrete Fourier transform:

$$(\widehat{G}_{\Delta t})_{r,s} = \exp\left(\frac{-2\Delta t}{\Delta x^2}(2 - \cos(2\pi r\Delta x) - \cos(2\pi s\Delta x))\right). \tag{2.4}$$

Finally, we implement a Richardson extrapolation–like procedure to improve the accuracy of the kernel, (as described in [22]), and define:

$$K_{\Delta t} = \frac{1}{3}\left(4G_{\frac{3}{2}\Delta t} - G_{3\Delta t}\right). \tag{2.5}$$

Redistribution

The convolution step gives diffusion generated motion along simple interfaces, but may create overlaps or vacuums at junctions where multiple interfaces meet. To enforce the desired no–overlap / no–vacuum condition, we apply a comparison step to obtain the updated level set functions

$$B_k(x) = \frac{1}{2}\left(A_k(x) - \max\{A_\ell : \ell \neq k\}\right), \tag{2.6}$$

This formulation guarantees that exactly one of the $B_k(x)$ (for $k = 1, \ldots, M$) is positive at any given location x. Furthermore, this procedure ensures that the symmetric Herring angle condition is maintained at all triple points [22].

Redistancing

At each time step, we need to compute the signed distance function C_k to a union Ξ_k of disjoint components; we need the distance function only in a tubular neighborhood of the boundary $\partial\Xi_k$ of Ξ_k. The width of the tubular neighborhood is proportional to the kernel width, which in turn is proportional to $\sqrt{\Delta t}$. We make use of a two–phase redistancing algorithm that depends only on the input values $B_k(x) = \frac{1}{2}(A_k(x) - \max\{A_\ell : \ell \neq k\})$ at grid points within two grid points of the interface. For the remainder of the discussion of redistancing, we drop the subscript k for convenience, as each set is updated independently of the others.

Define the set of boundary points β to be

$$\beta = \{(i,j) : (|\mathrm{sgn}(B_{i+1,j}) - \mathrm{sgn}(B_{i-1,j})| + |\mathrm{sgn}(B_{i,j+1}) - \mathrm{sgn}(B_{i,j-1})|) > 0\}\,, \quad (2.7)$$

where $B_{i,j} = B(i\Delta x, j\Delta y)$ and

$$\mathrm{sgn}(x) = \begin{cases} 1 & \text{if } x > 0, \\ 0 & \text{if } x = 0, \\ -1 & \text{if } x < 0. \end{cases} \quad (2.8)$$

These boundary values are set initially to respect the condition that $|\nabla C| = 1$, while moving the interface as little as possible. Specifically, we set

$$C_{ij} = \frac{B_{ij}}{|\nabla B_{ij}|}, \qquad \forall (i,j) \in \beta. \quad (2.9)$$

Typically, the centered difference approximation is appropriate for $|\nabla B_{ij}|$, but does not work well on small components. See Figure 2.1 for an illustration in one dimension. The solid line is the exact signed distance function to the thick bar shown at the bottom of the plot. The dashed line shows the centered difference approximation to the gradient of the signed distance function at the indicated point. Upwind

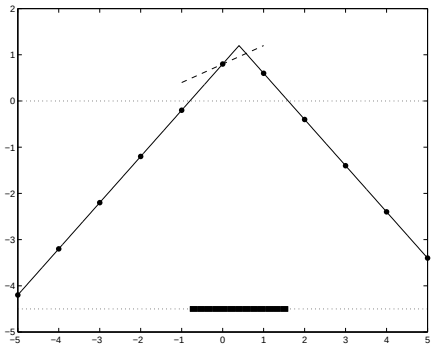

Figure 2.1: Failure of centered differencing on small components. The thick black line indicates the set $\Sigma = \{x : d(x) > 0\}$. The slope of the dashed line indicates the centered difference approximation to $|\nabla d|_1$ at the specified point. The upwind differencing finds $|\nabla d|_2$=1, the correct value for $|\nabla d|$.

differencing is only first–order accurate in general, but gives a more accurate value for the gradient at this point. We define

$$|\nabla B_{ij}|_1 = \sqrt{\left(\frac{B_{i+1,j} - B_{i-1,j}}{2\Delta x}\right)^2 + \left(\frac{B_{i,j+1} - B_{i,j-1}}{2\Delta y}\right)^2}, \tag{2.10}$$

$$|\nabla B_{ij}|_2 = \left(\left[\max\left(\frac{|B_{i+1,j} - B_{i,j}|}{\Delta x}, \frac{|B_{i,j} - B_{i-1,j}|}{\Delta x} \right) \right]^2 + \left[\max\left(\frac{|B_{i,j+1} - B_{i,j}|}{\Delta y}, \frac{|B_{i,j} - B_{i,j-1}|}{\Delta y} \right) \right]^2 \right)^{1/2}, \tag{2.11}$$

and define

$$|\nabla B_{ij}| = \begin{cases} |\nabla B_{ij}|_1 & \text{if } \frac{1}{2}|\nabla B_{ij}|_2 \le |\nabla B_{ij}|_1 \le 2|\nabla B_{ij}|_2, \\ |\nabla B_{ij}|_2 & \text{otherwise.} \end{cases} \tag{2.12}$$

We fix the values C_{ij} for all $(i, j) \in \beta$, and first generate a first–order in space accurate approximation of the signed distance function using fast sweeping as described in [85, 95]. Then we perform an iterative second–order accurate method (described in [72]) for a limited number of iterations on this output. The input $B(x)$ may be far from a distance function near junctions. Performing the fast sweeping initially allows us to perform only a limited number of iterations with the second–order method, which is the most time–intensive part of the algorithm.

Swapping

The swapping step allows each signed distance function to store many components safely. Without this step, it would be necessary to maintain each individual component in a separate set to guarantee that coalescence could not occur. For example, in a calculation performed on a 4096^2 grid, we begin with over $n_0 = 160,000$ components and use only $k_{\max} = 32$ sets to track them all. The algorithm introduces new signed distance functions if needed to ensure that inter–component spacing is maintained. In our experience, the algorithm typically does not require more than $k_{\max} = 32$ sets in two dimensions, and not more than $k_{\max} = 64$ sets in three dimensions. As the network evolves we find it will rarely, if ever, introduce new signed distance functions. Without the savings of both memory and computational time permitted by this additional step (allowing the number of sets, $k_{\max}$, to satisfy $k_{\max} \ll n_0$, the total number of components), such a large scale computation would be impossible.

Our approach, described below, is similar to that of Krill and Chen [51]. They reassign components to prevent any particular component from being maintained in the same set as any of its nearest or second–nearest neighbors. We, instead, make sure that any two components described by the same signed distance function are not too close (we will be more precise shortly). This distinction is significant for our algorithm, as spatial separation is key to prevent distinct components, described by the same signed distance function, from interacting during the convolution step (the width of the kernel is of course related to the time step size, which can be large thanks to the unconditional stability of the proposed algorithms).

To describe this algorithm we must first outline some notation. Let the set $\Xi_k = \{x : d_k(x) > 0\}$ correspond to a collection of disjoint components. We say that two components, say, Σ_a and Σ_b, in Ξ_k are τ–close if their union is completely contained

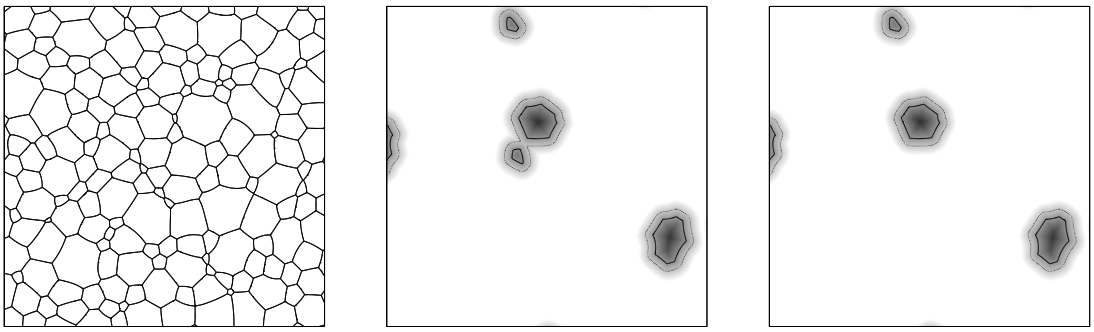

(a) (b) (c)

Figure 2.2: (a) Part of a network. (b) Overlay of the boundary of $d^{n+\frac{1}{2}} > 0$ (solid line) and $d^{n+\frac{1}{2}} > -\tau$ (dotted line) on the signed distance function $d^{n+\frac{1}{2}}$. (c) Same for d^{n+1} after a component is removed and d^{n+1} is recalculated.

in the same connected component of $\{x : d_k(x) > -\tau\}$ (which is trivially checked by comparing the $(-\tau)$–super level set membership of any two grid points belonging to Σ_a and Σ_b). We choose $\tau > 0$ to be proportional to $\sqrt{\Delta t}$ to prevent distinct components in Ξ_k from interacting during the convolution step. See Figure 2.2 for illustration of the selection process. The swapping step of Algorithm 2.1 is described in greater detail in Algorithm 2.2.

2.1.3 Numerical Convergence Tests

In this section, two types of numerical results are presented. First, we display the convergence of our algorithm to an exact solution known for two–phase motion, demonstrate that we match a known solution well in three–phase motion, and show that exact formulae for the evolution of the area of the phases are satisfied. Finally, we examine the spatial and temporal convergence of our algorithm in a multiphase case with many topological changes for which no exact solution is known.

Input: Signed distance functions $C_k(x)$, for $k = 1, \ldots, k_{\max}$.
Output: Updated signed distance function $d_k^n(x)$, for $k = 1, \ldots, k_{\max}$.

Do steps 1–2 for $k = 1, \ldots, k_{\max}$.

1. Initialize $d_k^j = C_k$.
2. While there are at least two components in any d_k^j that are τ–close, select any τ–close pair of components in $d_{k^*}^j$, and perform steps (a)–(e).
   (a) Select the smaller component from the pair (measured by the number of grid points contained in each component). Let $d_G(x)$ be the signed distance function to the boundary of the selected component and define the set $X = \{x : d_G(x) > -\tau\}$.
   (b) Find a d_ℓ^j, such that $\ell \neq k^*$ and $d_\ell^j(x) \leq -\tau \ \forall \ x \in X$. If such a set cannot be found, increment $k_{\max} \leftarrow k_{\max} + 1$, initialize $d_{k_{\max}}^j = -\tau$, and select $\ell = k_{\max}$.
   (c) Add the component to d_ℓ^j by setting $d_\ell^j(x) = d_G(x) \ \forall \ x \in X$.
   (d) Remove this same component from $d_{k^*}^j$ by setting $d_{k^*}^j = -\tau \quad \forall x \in X$.
   (e) Redistance $d_{k^*}^j$ and d_ℓ^j on the set X.

Algorithm 2.2: Swapping for Step 4 of Algorithm 2.1.

Convergence to Exact Solutions in Two Phase Motion

We begin by verifying that our algorithm accurately simulates two phase motion by mean curvature on the simplest examples in two and three dimensions: the circle and the sphere. In each case, the motion reduces to the simple ordinary differential equation,

$$\dot{r}(t) = \kappa = \frac{-C}{r}, \tag{2.13}$$

where $C = 1$ for the circle and $C = 2$ for the sphere. Eq. (2.13) has the solution

$$r(t) = \sqrt{r(0)^2 - 2Ct}. \tag{2.14}$$

In our tests, we chose $r(0) = .25$. For the circle, we took as our stopping time $t^\star = 3/128$, and for the sphere $t^\star = 3/256$, so that the exact solution has $r(t^\star) = .125$. While the evaluation of the curvature is second–order accurate in space and time, the method as a whole is expected to show linear convergence in both space and

Resolution	Iterations	$r(t^\star)$	% Error	Exact Redist Result	% Error
8×8	7	0.143812	15.0493%	0.068539	45.1687%
16×16	15	0.124301	0.5595%	0.112370	10.1040%
32×32	30	0.123497	1.2022%	0.123544	1.1649%
64×64	60	0.123918	0.8653%	0.124435	0.4520%
128×128	120	0.124246	0.6110%	0.124562	0.3501%
256×256	240	0.124585	0.3323%	0.124751	0.1996%
512×512	480	0.124797	0.1627%	0.124870	0.1043%
1024×1024	960	0.124900	0.0800%	0.124934	0.0532%
2048×2048	1920	0.124952	0.0383%	0.124966	0.0268%

Table 2.1: Convergence check: Motion by curvature of a circle.

Resolution	Iterations	$r(t^\star)$	% Error	Exact Redist Result	% Error
$8 \times 8 \times 8$	7	0.153862	23.0896%	0.113474	9.2212%
$16 \times 16 \times 16$	15	0.128935	3.1484%	0.120004	3.9964%
$32 \times 32 \times 32$	30	0.124040	0.7682%	0.123044	1.5648%
$64 \times 64 \times 64$	60	0.123881	0.8951%	0.124010	0.7923%
$128 \times 128 \times 128$	120	0.124289	0.5688%	0.124481	0.4150%
$256 \times 256 \times 256$	240	0.124627	0.2988%	0.124735	0.2121%

Table 2.2: Convergence check: Motion by curvature of a sphere.

time. This is due to the time integration, which operates under the assumption that curvature remains constant through each iteration. See Tables 2.1 and 2.2 for numerical results. The results labeled "Exact Redist Result" were obtained by replacing the distance function at the redistancing step by the exact distance function for a circle or sphere with the same 0—level set at each step. We note that the linear convergence rate is strongly indicated by the exact redistancing results for resolutions $\geq 256 \times 256$ for the circle and $\geq 64 \times 64 \times 64$ for the sphere. Our redistancing technique causes some cancellations of error at low resolutions, but follows the linear convergence trend shown by the exact redistancing results well at higher resolutions.

Comparison to Known Profile in Three Phase Motion

In this test of three phase motion, we choose homogenous Neumann boundary conditions and consider a T–junction initial condition as shown in Figure 2.3. It was shown in [30] that there is an exact solution for this initial T–junction geometry consisting of a steady profile moving at constant speed. The profile is given for

$0 \leq x \leq 0.5$ by:

$$y(x,t) = \frac{3}{\pi}\log\left(\cos\left(\frac{\pi x}{3}\right)\right) + (y_0 - vt), \tag{2.15}$$

where v is the velocity of the profile and y_0 is determined by the initial location of the T–junction. Figure 2.3 shows the close agreement between the predicted profile where vt was chosen to match the computed profile at $x = 0$. These results were computed on a 128×128 grid. In (a), the predicted profile and computed profiles are indistinguishable. Parts (b), (c), and (d) zoom in successively on the final computed profile and the associated prediction. We see that the results differ by less than 10^{-3} for all x. The triangular "split" in the profile seen in the zoomed views is purely a visualization artifact.

Convergence of Area Calculations

The von Neumann area law [86] states that, under multiphase motion by curvature (1.3), the area A of a phase with n triple junctions evolves through time with

$$\frac{dA}{dt} = \frac{\pi}{3}(n-6). \tag{2.16}$$

Thus phases with less than six sides shrink, and phases with more than six sides grow. This result applies only in two spatial dimensions; a much more complicated result was recently found in three dimensions [54].

In [22], the authors apply Algorithm 1.4 to the initial condition shown in Figure 2.4 as the grid and time step are refined. The results are summarized in Table 2.3 and are suggestive of the $O(\sqrt{t})$ error at triple junctions suggested by (1.36).

Convergence of Multiphase Motion

There are no explicit solutions available for the evolution of a general network, especially through topological changes. Furthermore, there is no rigorous notion

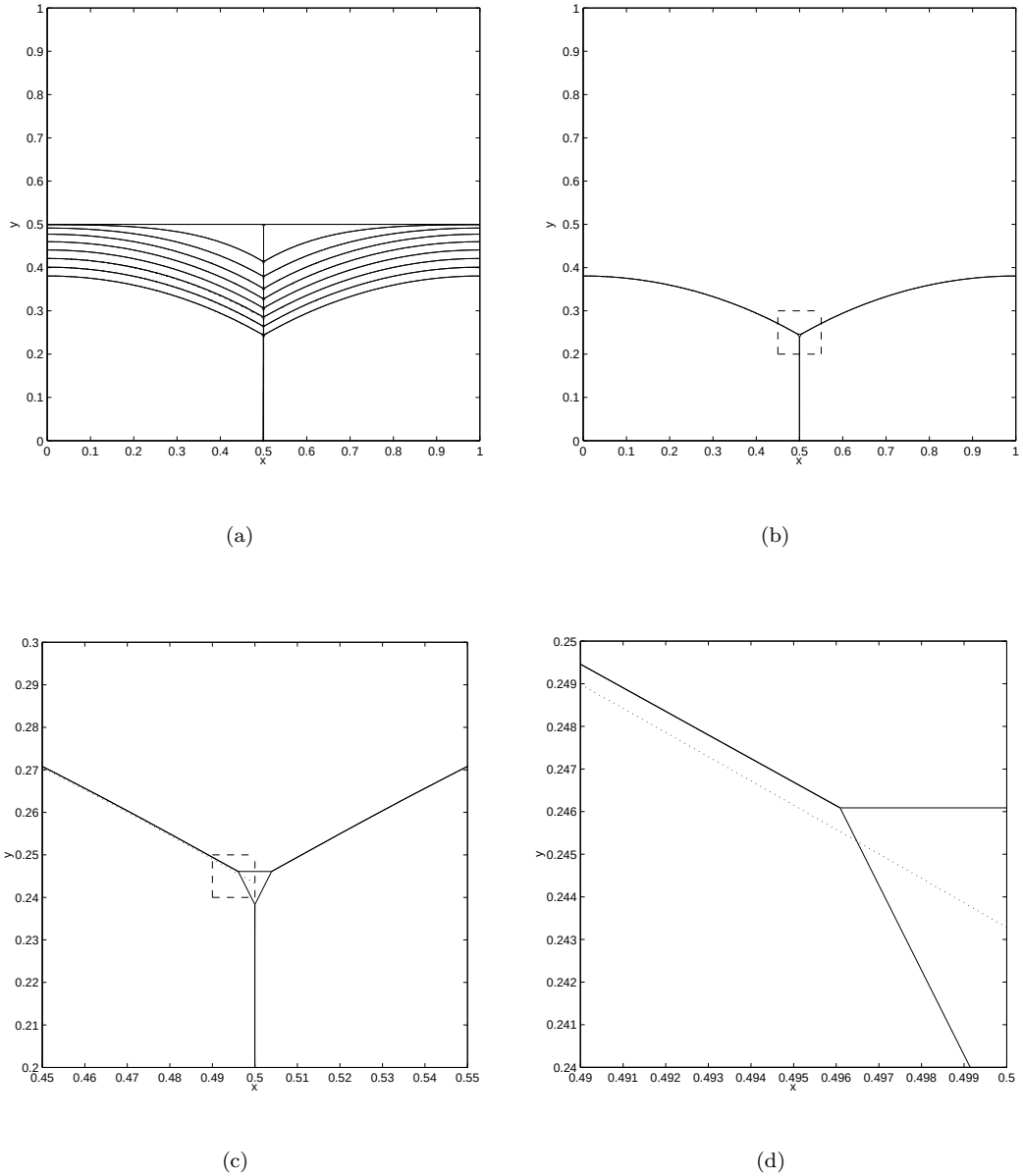

Figure 2.3: (a) Interface shown at various times in evolution (solid). The exact profile is overlaid (dotted) once a constant profile is attained. (b), (c), (d) Successive zoom in to the computed profile (solid) and exact profile (dotted). The triangular region visible in (c) and (d) is a visualization artifact.

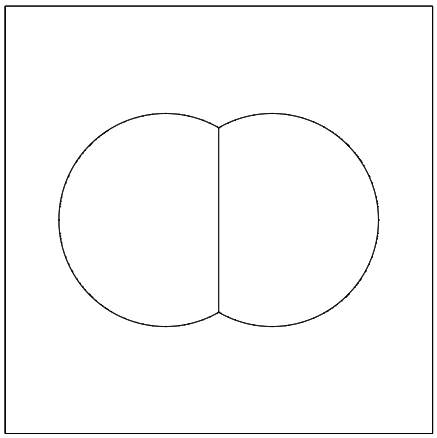

Figure 2.4: Initial condition for overlapped circle area convergence tests. The von Neumann law predicts that $dA/dt = -4\pi/3$ for the partial circles. Table 2.3, reproduced from [22], demonstrates the convergence to this prediction as the grid and time step are refined.

Simulation	Δt	nt	Relative Error	Order
32×32	1/1920	30	3.91%	—
64×64	1/3840	60	2.07%	0.918
128×128	1/7680	120	1.28%	0.693
256×256	1/15360	240	0.84%	0.608
512×512	1/30720	480	0.53%	0.664

Table 2.3: Input parameters and relative error in time rate of area change for overlapped circles test. Time step indicated by Δt, nt indicates the number of time steps used, and Order calculated as $\log_2$((previous relative error)/(current relative error)).

of a weak solution with uniqueness through such events. However, it is reasonable to expect that at least the statistical descriptors of the network (for example, the distribution of component sizes) to be eventually independent of further spatial or temporal resolution under refinement. To test this expectation, we choose an initial condition containing $11,217$ components and sample on grids of 1024×1024, 2048×2048 and 4096×4096, refining the discretization in both space and time. We keep the ratio between Δx and Δt constant to refine both spatial discretization and the effective sampling rate of the Gaussian kernel. Table 2.4 describes the simulations.

The simulation runs for total time $80/1024^2$. Approximately 6000 components disappear during this evolution, corresponding to many thousands of topological transitions (i.e. elimination of edges). Less than half the original number of components remain at the end of the simulation. The number of components remaining after each simulation varies (shown in Table 2.4), but this is not a good measure of the convergence, because there is a lower limit on the size of components that can be accurately represented by a given time step. Instead, it is more appropriate to look at statistical quantities (such as the distribution of component sizes) and the actual microstructure resulting from the simulations. These are shown in Figure 2.5. The histogram of component sizes demonstrates that each simulation has a very similar distribution of component sizes for components with areas larger than approximately 10^{-4}. The deviation in the total number of components remaining in each of the simulations can be attributed almost fully to the differences in the first bin alone (corresponding to the smallest grains) of the histogram.

A small section of the microstructure is shown in Figure 2.5(c), one twenty–fifth of the entire computational domain for each simulation. There are very few differences between the evolution with $\Delta x = 1/4096$ and with $\Delta x = 1/2048$. There

Simulation	Δx	Δt	nt	$n(nt \cdot \Delta t)$
1024×1024	$1/1024$	$0.8/1024^2$	100	5177
2048×2048	$1/2048$	$0.4/1024^2$	200	5286
4096×4096	$1/4096$	$0.2/1024^2$	400	5398

Table 2.4: Input parameters and final number of components for simulations testing convergence of multiphase motion. nt indicates the number of time steps used, and $n(nt \cdot \Delta t)$ indicates the number of components remaining at the end of the simulation.

are considerably more differences between these simulations and the result with $\Delta x = 1/1024$, but even there, the majority of the microstructure exactly matches that computed at higher resolutions. The agreement between the results is remarkable considering the great disparity between the initial condition (Figure 2.5(b)) and the simulation results and the thousands of topological changes occurring in the evolution.

2.2 Algorithm for Motion by Curvature Plus Constant Velocity

As discussed in Chapter I, the addition of a constant velocity term to (1.3) gives a new model (1.5) with significantly different properties. Only a small modification to Algorithm 2.1 is needed to adapt the algorithm (1.5). For completeness, the adapted algorithm is presented as Algorithm 2.3. Only the update step differs from that of Algorithm 2.1. The algorithm is applied to simulations of recrystallization in polycrystalline materials in Chapter IV.

2.3 Algorithms for Weighted Curvature Motion

The original DFDGM algorithm (Algorithm 2.1) is demonstrated to be accurate, efficient, and unconditionally stable for equal surface tensions ($\gamma_{k\ell} = 1 \ \forall k, l$) in Chapter III. Furthermore, it is shown in [22] that this algorithm imposes the Herring angle conditions [36], which require in this special case that the opening angle of each grain at a triple junction must be 120°.

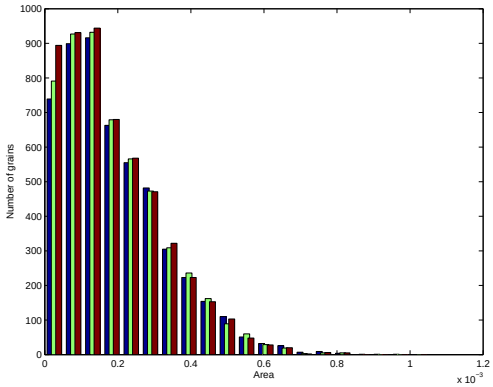

(a)

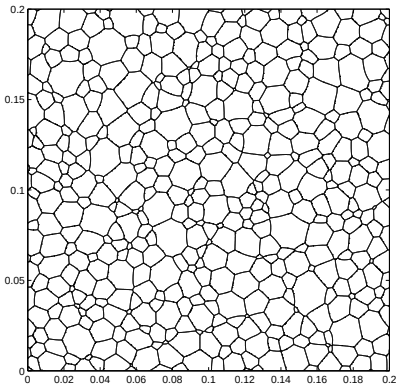

(b)

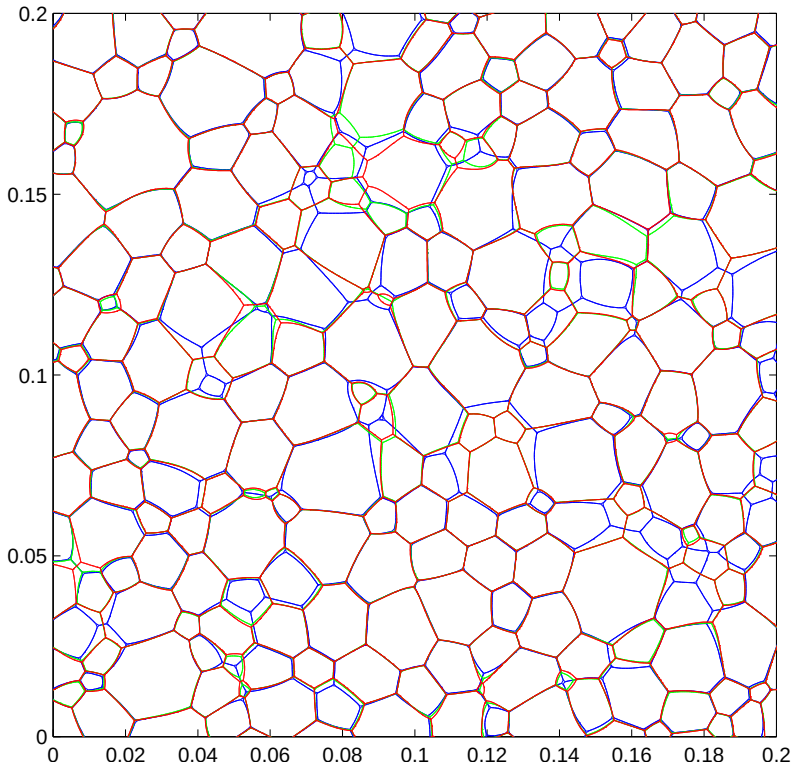

(c)

Figure 2.5: Multiphase motion convergence test results. Each test was run for total time $80/1024^2$. $\Delta x = 1/1024$, $\Delta t = 0.8/1024^2$ corresponds to blue, $\Delta x = 1/2048$, $\Delta t = 0.4/1024^2$ corresponds to green, and $\Delta x = 1/4096$, $\Delta t = 0.2/1024^2$ corresponds to red in (a) and (c). (a) The histogram of component sizes for the various simulations. Note that significant differences in the histograms occur only for very small components. (b) A subsection of the initial condition for these simulations containing $1/25$ of the simulation domain. Approximately 6000 components disappear between this state and the final states pictured in (c), corresponding to many thousand topological transitions. (c) The same subsection of the domains at time $80/1024^2$. Note that the agreement between the red and green microstructure is better than the agreement between blue and either red or green microstructure.

Input: Signed distance functions d_k^0, for $k = 1, \ldots, k_{\max}$, discrete time step size Δt, and number of time steps $j_{\max}$.
Output: Signed distance functions d_k^j, for $k = 1, \ldots, k_{\max}$ and $j = 1, \ldots, j_{\max}$.

For: $j = 1, \ldots, j_{\max}$, do steps 1–4 for $k = 1, \ldots, k_{\max}$.

1. UPDATE: Compute $A_k(x) := K_{\Delta t} * d_k^{j-1} - 2\lambda \Delta t e_k$, where $K_{\Delta t}$ is

$$K_{\Delta t} = G_{\Delta t} \qquad \text{or} \qquad K_{\Delta t} = \frac{1}{4}\left(4G_{\frac{3}{2}\Delta t} - G_{3\Delta t}\right),$$

   and $G_{\Delta t}$ is the fundamental solution of the heat equation:

$$G_{\Delta t}(x) = \frac{1}{(4\pi\Delta t)^{\frac{N}{2}}} e^{-\frac{|x|^2}{4\Delta t}}.$$

2. REDISTRIBUTE: Construct $B_k(x) = (A_k(x) - \max_{\ell \neq k} A_\ell(x))/2$ to remove overlaps and vacuums from the previous step.

3. REDISTANCE: Set $C_k(x)$ to be the signed distance function to the zero-level set of $B_k(x)$.

4. SWAP: If necessary swap appropriate components between signed distance functions $C_k(x)$ to ensure that all the components associated to given signed distance function remain well separated. Redistance around swapped components and denote the resulting signed distance functions as d_k^j.

Algorithm 2.3: DFDGM for multiphase motion by curvature plus bulk velocity.

It is easily shown that replacing $K_{\Delta t}$ by $K_{\gamma_k \Delta t}$ in Algorithm 2.1 leads to normal velocities of the form

$$v_n(\Gamma_{k\ell}) = \frac{\gamma_k + \gamma_\ell}{2}\kappa_{k\ell}, \tag{2.17}$$

however, no simple modification of Algortihm 2.1 enforces the physically-correct Herring angle conditions (1.9-1.10) for this setup where $\gamma_{k\ell} = (\gamma_k + \gamma_\ell)/2$. In the remainder of this section, we first describe an idea of Almgren, Taylor, and Wang [3] based on *minimizing motions*, then describe our DFDGM algorithm based on this idea for normal velocities of the form (2.17), and finally, extend the algorithm to the more general motion of (1.7).

2.3.1 Algorithm for $\gamma_{k\ell} = (\gamma_k + \gamma_\ell)/2$

The Almgren-Taylor-Wang algorithm for approximating the motion by mean curvature of an interface [3] requires the solution of a variational problem at each time step. This algorithm is generalized to multiphase motion by curvature in [13, 23, 82, 83]. We use the simple formulation described in [23]. The variational problem

$$\vec{\Sigma}^{j+1} = \underset{\substack{\vec{\Sigma},\ \bigcup_k \Sigma_k = \Omega \\ \Sigma_k \cap \Sigma_\ell = \emptyset \quad \forall k \neq \ell}}{\operatorname{argmin}} \sum_{k=1}^{M} \left\{ \gamma_k (\text{Length of } \Sigma_k) + \frac{1}{\Delta t} \int_{\Sigma_k \triangle \Sigma_k^j} |d_k^j(x)| dx \right\}, \tag{2.18}$$

where $\triangle$ denotes the symmetric difference operator for two sets, is solved to advance the solution $\vec{\Sigma}^j = (\Sigma_1^j, \ldots, \Sigma_M^j)$ by a time step Δt to the new solution $\vec{\Sigma}^{j+1} = (\Sigma_1^{j+1}, \ldots, \Sigma_M^{j+1})$. Almgren, Taylor, and Wang [3] prove that the solution of this variational problem generates the normal velocity (2.17) and satisfies the Herring angle conditions (1.9) and (1.10). As shown in [23], the formulation (2.18) is equivalent to:

$$\vec{\Sigma}^{j+1} = \underset{\substack{\vec{\Sigma},\ \bigcup_k \Sigma_k = \Omega \\ \Sigma_k \cap \Sigma_\ell = \emptyset \quad \forall k \neq \ell}}{\operatorname{argmin}} \sum_{k=1}^{M} \left\{ \gamma_k (\text{Length of } \Sigma_k) - \frac{1}{\Delta t} \int_{\Sigma_k} d_k^j(x) dx \right\}. \tag{2.19}$$

Input: Signed distance functions d_k^0 and weights γ_k, for $k = 1, \ldots, k_{\max}$, discrete time step size Δt, number of time steps $j_{\max}$, inner discrete time step δt, and number of inner time steps $\tau_{\max}$.
Output: Signed distance functions d_k^j, for $k = 1, \ldots, k_{\max}$ and $j = 1, \ldots, j_{\max}$.

For $j = 1, \ldots, j_{\max}$, do steps 1–3:

1. For $k = 1, \ldots, k_{\max}$, set $d_k^{j,0} = d_k^{j-1}$.
2. For $\tau = 1, \ldots, \tau_{\max}$ and $k = 1, \ldots, M$, do steps (a)–(c):
   (a) UPDATE: Perform either update **U1** or **U2**, where
   U1: Compute
   $$A_k(x) = \left\{ \left(d_k^{j,\tau-1} \right)^{\wedge} R(\xi, \zeta)^{-1} \right\}^{\vee} + \frac{\delta t}{\Delta t} d_k^{j,0}, \tag{2.20}$$
   where
   $$R(\xi, \zeta) = 1 + \frac{2\gamma \delta t}{\Delta x^2} \left(2 - \cos(2\pi\xi) - \cos(2\pi\zeta) \right), \tag{2.21}$$
   $\cdot^{\wedge}$ and $\cdot^{\vee}$ indicate the discrete two-dimensional Fourier and inverse Fourier transforms, respectively, Δx is the grid spacing, δt is an "inner" time step associated with the minimization of (2.19) and ξ and ζ are the Fourier variables.
   U2: Compute
   $$A_k(x) = \left\{ \left(d_k^{j,\tau-1} + \frac{\delta t}{\Delta t} d_k^{j,0} \right)^{\wedge} \left(\frac{\delta t}{\Delta t} + R(\xi, \zeta) \right)^{-1} \right\}^{\vee}. \tag{2.22}$$
   (b) REDISTRIBUTE: Construct $B_k(x) = \left(A_k(x) - \max_{\ell \neq k} A_\ell(x) \right)/2$ to remove overlaps and vacuums from the previous step:
   (c) REDISTANCE: Set $d_k^{j,\tau}(x)$ to be the signed distance function to the zero-level set of $B_k(x)$.
3. Set $d_k^j(x) = d_k^{j,\tau_{\max}}(x)$.

Algorithm 2.4: DFDGM for motion by weighted mean curvature, with additive surface tensions.

We solve the sub-problem (2.19) at each time step via diffusion generated motion, to obtain Algorithm 2.4, for motion by (2.17).

The motivation for (2.20) and (2.22) is as follows: The normal velocity

$$v_n(\Gamma_k) = \gamma_k \kappa + \frac{1}{\Delta t} d_k^j \tag{2.23}$$

arises as gradient descent for the unconstrained version of (2.19). The PDE

$$d_t = \gamma \nabla^2 d + \frac{1}{\Delta t} F \tag{2.24}$$

will generate this normal velocity for the level sets of a signed distance function $d = d_k$, and where we denote $\gamma = \gamma_k$, and $F = d_k^j$.

For update **U1**, we split the right-hand side operator. We solve the discretized system for $d_t = \gamma \nabla^2 d$ implicitly via the discrete Fourier transform for the solution $d^{n+1/2}$,

$$\frac{d^{n+1/2} - d^n}{\delta t} = \gamma \nabla^2 d^{n+1/2}, \tag{2.25}$$

which simplifies to

$$(1 - \gamma \delta t \nabla^2) d^{n+1/2} = d^n, \tag{2.26}$$

with solution

$$d^{n+1/2} = \left\{ (d^n)^\wedge \, R(\xi, \zeta)^{-1} \right\}^\vee, \tag{2.27}$$

where $R(\xi, \zeta)$ is given by (2.21), then explicitly add the bulk term to generate the updated solution d^{n+1}:

$$d^{n+1} = d^{n+1/2} + \frac{\delta t}{\Delta t} F. \tag{2.28}$$

For update **U2**, we observe that adding a new term of the form $-(1/\Delta t)d$ does not affect the velocity of d at the interface (where $d = 0$), but, when handled implicitly, stabilizes the numerical update of the solution:

$$\frac{d^{n+1} - d^n}{\delta t} = \gamma \nabla^2 d^{n+1} + \frac{1}{\Delta t} F - \frac{1}{\Delta t} d^{n+1}, \tag{2.29}$$

which simplifies as

$$\left(1 + \frac{\delta t}{\Delta t} - \gamma \delta t \nabla^2 \right) d^{n+1} = d^n + \frac{\delta t}{\Delta t} F, \tag{2.30}$$

and has a solution similar to (2.27), as displayed in (2.22).

As in the standard diffusion-generated motion algorithm, step (b) serves to enforce the constraints $\bigcup_k \Sigma_k = D$ and $\Sigma_k \cap \Sigma_\ell = \emptyset, \;\; k \neq \ell$, and to ensure that the correct

(constrained) normal velocity

$$v_n(\Gamma_{k\ell}) = \frac{\gamma_k + \gamma_\ell}{2}\kappa + \frac{1}{\Delta t}\frac{d_k^j + d_\ell^j}{2} \tag{2.31}$$

is attained. Step (c) ensures that the following update step receives signed distance functions as input, which is necessary to generate the correct normal velocity.

2.3.2 Numerical Results

To verify Algorithm 2.4, we consider an initial condition of two overlapped circles (Σ_1 and Σ_2) on a background third phase Σ_3. The γ_i are chosen via (2.35) so that $\gamma_{13} = \gamma_{23} = 1$ and $\gamma_{12} \in (0, 2)$, to respect (1.11). Then (1.10) can be evaluated to find that

$$\theta_3 = 2\pi - 2\,\mathrm{acos}(-\gamma_{12}/2), \tag{2.32}$$

and a generalized version of the von Neumann relation (2.16) gives the time rate of change of area for the circular phases to be

$$\frac{dA}{dt} = 2\pi - \theta_3 - 2\pi = -2\,\mathrm{acos}(-\gamma_{12}/2). \tag{2.33}$$

We perform three sets of tests, with $\gamma_{12} = 1/2,\ 1\ \sqrt{2}$, respectively. Initial conditions are chosen so that the initial area of each circular phase is 0.18 and to satisfy (2.32). See Figure 2.6 to see sample initial conditions and final states for each surface tension. The evolution is simulated for $t = [0, \frac{1}{128}]$. The grid and time step are refined as described in Table 2.5, and 25 tests are performed at each resolution / surface tension combination. Initial conditions are rotated and translated for each test to mitigate grid effects. The change area of the circular phases is calculated at the end of each simulation and results are averaged to generate the relative errors presented in Table 2.5.

The results of Table 2.5 indicate that the algorithm is accurate, even for moderate resolution. Indeed, though larger time steps are taken than in the results using

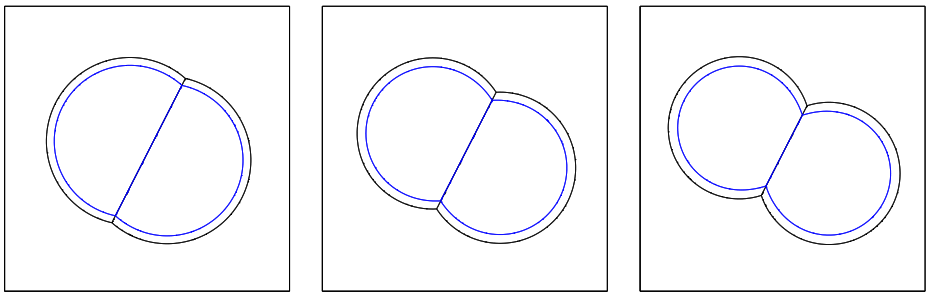

(a) (b) (c)

Figure 2.6: Sample initial conditions and final configurations for overlapping circle tests. Surface tensions are (a) $\gamma_{12} = 1/2$, (b) $\gamma_{12} = 1$, and (c) $\gamma_{12} = \sqrt{2}$.

Grid Size	Δt	nt	$\gamma_{12} = 0.5$	$\gamma_{12} = 1$	$\gamma_{12} = \sqrt{2}$
32×32	$1/1280$	10	6.0541%	1.2328%	2.7305%
64×64	$1/2560$	20	1.2946%	1.0811%	1.7712%
128×128	$1/5120$	40	0.3672%	0.8108%	1.0643%
256×256	$1/10240$	80	0.3414%	0.5082%	0.5146%
512×512	$1/20480$	160	0.3295%	0.3417%	0.1279%

Table 2.5: Relative error in measured dA/dt for overlapping circles. Column labeled as $\gamma_{12} = x$ gives the relative error in measured dA/dt for given surface tension. Results are very accurate, but do not show a clear indication of convergence.

Algorithm 1.4 presented in Table 2.3, relative errors are smaller. However, the current results do not indicate the nice convergence rate seen in Table 2.3. It is possible that the algorithm used to measure areas is not accurate enough to demonstrate the convergence of the method.

For this specialized problem, the evolution of the Γ_{13} and Γ_{23} interface can be simulated very accurately using an explicit representation of the interface. At the boundaries, endpoints of the interfaces are constrained to lie along the initial Γ_{12} interface and to respect the angle condition (2.32). Explicit solutions were calculated using front tracking techniques with $10,000$ points initially (additional points were added to reparameterize the curve whenever the gap between the boundary points and their neighbors grew large) and two million time steps to simulate the evolution for $t = [0, \frac{1}{128}]$.

	$\gamma_{12} = 0.5$		$\gamma_{12} = 1$		$\gamma_{12} = \sqrt{2}$	
Grid Size	$\text{dist}(\Gamma_{13}, X)$	Order	$\text{dist}(\Gamma_{13}, X)$	Order	$\text{dist}(\Gamma_{13}, X)$	Order
32×32	1.0579×10^{-2}	—	1.0739×10^{-2}	—	1.1504×10^{-2}	—
64×64	5.1555×10^{-3}	1.0370	5.3616×10^{-3}	1.0019	5.6943×10^{-3}	1.0145
128×128	2.5806×10^{-3}	0.9984	2.6988×10^{-3}	0.9904	2.8675×10^{-3}	0.9897
256×256	1.3001×10^{-3}	0.9891	1.3466×10^{-3}	1.0030	1.4290×10^{-3}	1.0048
512×512	6.6157×10^{-4}	0.9746	6.8884×10^{-4}	0.9671	7.1392×10^{-4}	1.0011

Table 2.6: Distance between Γ_{13} and exact solution X. Δt and nt are the same as in Table 2.5. $\text{dist}(\Gamma_{13}, X)$ is measured by (2.34), and Order is calculated as $\log_2$((dist at previous grid size)/(dist at current grid size)). Linear convergence is observed.

We take this parameterized curve $X(s)$ to be the exact solution and measure the distance between the exact solution and the solution Γ_{13} computed via Algorithm 2.4 as

$$\text{dist}(\Gamma_{13}, X) = \int_X |d_1(x)| ds. \tag{2.34}$$

The results are ensemble averaged over the 25 runs and presented in Table 2.6. Linear convergence of Γ_{13} to X in this sense is clearly indicated. The numerical results presented here for the numerical convergence of Algorithm 2.4 to the motion of (2.17) demonstrate good accuracy on moderately refined grids and provide strong suggestion that this algorithm creates the desired motion.

2.3.3 Algorithm for Arbitrary $\gamma_{k\ell}$

Algorithm 2.4 limits the choice of $\gamma_{k\ell}$ in (1.7) to $\gamma_{k\ell} = (\gamma_k + \gamma_\ell)/2$. The real goal is to allow for $\gamma_{k\ell}$ to be chosen arbitrarily, up to simple conditions such as (1.11). We begin by noting that in the three-phase case, arbitrary surface tensions γ_{12}, γ_{13}, and γ_{23} can be mapped to γ_1, γ_2, γ_3 so that $\gamma_{12} = (\gamma_1 + \gamma_2)/2$, etc., by the mapping:

$$\begin{pmatrix} \gamma_1 \\ \gamma_2 \\ \gamma_3 \end{pmatrix} = \begin{pmatrix} 1 & 1 & -1 \\ 1 & -1 & 1 \\ -1 & 1 & 1 \end{pmatrix} \begin{pmatrix} \gamma_{12} \\ \gamma_{13} \\ \gamma_{23} \end{pmatrix}. \tag{2.35}$$

Thus, the algorithm of Section 2.3.1 is sufficient to generate three-phase motion with arbitrarily chosen surface tensions.

For k-phase motion, we note that there is, in general, no assignment of surface tensions γ_k so that the arbitrary $\gamma_{k\ell}$ can be written as $\gamma_{k\ell} = (\gamma_k + \gamma_\ell)/2$. Instead, a proposed numerical approach is to attempt to solve the Almgren, Taylor, and Wang optimization problem at each physical time step by performing alternating minimization over triples of adjacent grains $T = \{T_1, T_2, T_3\}$ using the correct surface tensions γ_k defined by (2.35). As each triple is updated, we take care to enforce the condition

$$\Sigma_{T_1} \cup \Sigma_{T_2} \cup \Sigma_{T_3} = \Sigma'_{T_1} \cup \Sigma'_{T_2} \cup \Sigma'_{T_3}, \tag{2.36}$$

that is, that the region covered by the union of the input sets Σ_{T_i} matches the region covered by the union of the output sets Σ'_{T_i} after this triple is updated. Algorithm 2.5 describes this extension.

We make two important observations about Algorithm 2.5. First, while the loop over triples of adjacent grains proceeds, *two* sets of signed distance functions must be maintained — both the data from the beginning of the time step, $\{D_k\}$, and the current data $\{d_k^j\}$. The data $\{D_k\}$ is maintained so that the updated set Σ_k^j cannot move too far from the set Σ_k^{j-1} at the previous *outer* time step, while the more current data $\{d_k^j\}$ is used as the starting point for the inner update. Second, the redistribution step is the minimum of the standard (three-phase) redistribution step and a new term, $(d_k^{j,\tau-1} - d_\beta)$, which ensures that condition (2.36) is fulfilled. This algorithm is a generalization of Algorithm 2.4 to try to allow for normal velocities of the more general form (1.7). It has not been carefully tested, and currently is included only as an indication of how such a generalization might be achieved. Much work remains to be done before this algorithm can be seriously presented as a good

Input: Signed distance functions d_k^0 for $k = 1, \ldots, k_{\max}$, surface tensions $\gamma_{k\ell}$ for $k, \ell = 1, \ldots, k_{\max}$ and $\ell \neq k$, discrete time step size Δt, number of time steps $j_{\max}$, inner discrete time step δt, and number of inner time steps $\tau_{\max}$.
Output: Signed distance functions d_k^j, for $k = 1, \ldots, k_{\max}$ and $j = 1, \ldots, j_{\max}$.

For $j = 1, \ldots, j_{\max}$, do steps 1–3:

1. For $k = 1, \ldots, k_{\max}$, set $D_k = d_k^{j-1}$ and $d_k^j = d_k^{j-1}$.
2. For each triple of adjacent grains $T = \{T_1, T_2, T_3\}$, do steps (a)–(d):
   (a) Define $d_\beta = -\mathbf{Dist}\left(\Sigma_{T_1}^j \cup \Sigma_{T_2}^j \cup \Sigma_{T_3}^j\right)$.
   (b) Apply Equation (2.35) to compute γ_{T_1}, γ_{T_2}, and γ_{T_3} from $\gamma_{T_1T_2}$, $\gamma_{T_1T_3}$, and $\gamma_{T_2T_3}$.
   (c) For $\tau = 1, \ldots, \tau_{\max}$, and $k = T_1, T_2, T_3$, do steps (i)–(iii):
      i. UPDATE: Perform either update **U1** or **U2**, where
      U1: Compute

$$A_k(x) = \left\{ \left(d_k^{j,\tau-1}\right)^\wedge \left(1 + \frac{2\gamma_k \delta t}{\Delta x^2}\left(2 - \cos(2\pi\xi) - \cos(2\pi\zeta)\right)\right)^{-1} \right\}^\vee + \frac{\delta t}{\Delta t} D_k, \tag{2.37}$$

      and
      U2: Compute

$$A_k(x) = \left\{ \left(d_k^{j,\tau-1} + \frac{\delta t}{\Delta t} D_k\right)^\wedge \left(1 + \frac{\delta t}{\Delta t} + \frac{2\gamma_k \delta t}{\Delta x^2}\left(2 - \cos(2\pi\xi) - \cos(2\pi\zeta)\right)\right)^{-1} \right\}^\vee. \tag{2.38}$$

      ii. REDISTRIBUTE: Construct

$$B_k(x) = \min\left(A_k(x) - \max_{\ell \neq k} A_\ell(x), \quad d_k^{j,\tau-1} - d_\beta\right)/2 \tag{2.39}$$

      to remove overlaps and vacuums from the previous step:
      iii. REDISTANCE: Set $d_k^{j,\tau}(x)$ to be the signed distance function to the zero-level set of $B_k(x)$.
   (d) Set $d_k^j(x) = d_k^{j,\tau_{\max}}(x)$.

Algorithm 2.5: DFDGM for motion by weighted mean curvature.

candidate for the evolution defined by (1.7).

CHAPTER III

Application: Isotropic Grain Growth

Grain growth is an important process by which the microstructure of a polycrystalline material (including most metals and ceramics) evolves during manufacturing processes. Statistical measures of the resultant microstructure affect important macroscale properties of the material, such as its conductivity and brittleness. Manufacturing processes must typically be tuned to provide for an optimal blend of desired material properties; however, performing such tuning experimentally is costly and time consuming. As a result, simulations of grain growth have been attempted using a variety of numerical techniques. Several common techniques are described in Section 1.1.

Grain growth occurs when polycrystalline materials are annealed. The well-known model for grain growth [9, 35, 63] gives the normal velocity (outward from phase Σ_k) of the interface $\Gamma_{k\ell}$ by

$$v_n(\Gamma_{k\ell}) = \mu\gamma_{k\ell}\kappa_{k\ell}, \tag{3.1}$$

Here, μ denotes the boundary mobility, $\gamma_{k\ell}$ the grain boundary energy per unit area for the interface $\Gamma_{k\ell}$, and $\kappa_{k\ell}$ the mean curvature of the boundary separating two grains. We use the convention that if phase Σ_k is a spherical grain of radius r surrounded by phase Σ_ℓ, then $\kappa_{k\ell} = -2/r$.

Here, we specialize to the case where all surface tensions are constant and equal: $\gamma = \gamma_{k\ell}$, often called "isotropic grain growth." The theory for this extension is complete in two dimensions in the absence of topological events. Additional study of topological events such as the division of four junctions following grain disappearence is still incompletely developed. Here, we nondimensionalize the normal velocity using the mean initial grain radius $\langle r_0 \rangle$, derived from the mean initial grain volume $\langle V_0 \rangle$ by $\langle r_0 \rangle = (3\langle V_0 \rangle/(4\pi))^{1/3}$. We define the nondimensionalized curvature as $\kappa^\star_{k\ell} = \langle r_0 \rangle \kappa_{k\ell}$. We further nondimensionalize the velocity as $v_n(\Gamma_{k\ell}) = V \cdot v^\star_n(\Gamma_{k\ell})$, with velocity $V = \langle r_0 \rangle / T$ and time $T = \langle r_0 \rangle^2/(\mu\gamma)$, so that

$$v^\star_n(\Gamma_{k\ell}) = \kappa^\star_{k\ell}. \tag{3.2}$$

Note that this equation matches (1.3) exactly.

As shown in [68] and [96], this nondimsionalized normal speed arises as gradient descent for the nondimensional energy

$$E^\star = \sum_{k<\ell} (\text{area of } \Gamma_{k\ell}). \tag{3.3}$$

We note that the time scale T is chosen so that $t^\star = 1/4$ is the time required for an isolated grain of radius $\langle r_0 \rangle$ to disappear under pure curvature motion in the nondimensional system. Hereafter, we drop the $\star$ notation and refer solely to the nondimensionalized quantities, e.g. the nondimensionalized energy $E^\star$ will be referred to as E.

Algorithm 2.1 is used for the simulations in this chapter. We present large-scale two- and three-dimensional simulations of grain growth, far beyond the scale of simulations presented previously. These simulations are performed on a parallelized version of the code executing on a large cluster. The results are analyzed in great

detail and compared to numerous theoretical predictions, results from experiments and smaller simulations performed with various numerical methods.

The two-dimensional simulation of grain growth is presented in Section 3.1. Statistics including the mean grain area, and number of edges and relative grain size distributions are computed and compared with theoretical results. A large-scale simulation of three-dimensional grain growth is presented and analyzed in Section 3.2. The initial condition contains over $130,000$ fully resolved grains, and the evolution is simulated until only about $14,000$ remain. We present various statistics collected throughout this simulation. In particular, we demonstrate the anticipated self-similar character of the grain size distribution as it evolves in time. Furthermore, our results show good agreement with other three-dimensional predictions for grain growth, such as power law growth of the mean grain volume, and three-dimensional version of the Aboav–Weaire law [1, 89] and the Mullins extension of the two-dimensional von Neumann–Mullins relationship [64].

3.1 Two-Dimensional Simulation

We concern ourselves with the standard case, in which all interfaces move with normal velocity equal to the curvature of the interface. In future work we will investigate varying surface tensions and bulk energies. As previously shown in [22], this algorithm naturally imposes the symmetric angle condition (all triple junctions meet at 120° angles).

We let $\Omega = [0,1]^2$, and discretize this domain with $\Delta x = \Delta y = 1/4096$. We use periodic boundary conditions, which is natural as the interactions between grains are short–ranged. Our initial condition contains 166,927 grains, and was obtained by constructing the Voronoi diagram for random points with a uniform distribution

in the computational domain; this is common practice for the initialization of grain growth simulations. We take 1,500 time steps with time step $\Delta t = .8/4096^2$, at the end of which 11,217 grains remain and the evolution of the system has slowed considerably. (An adaptive time stepping strategy would therefore be prudent, and is entirely feasible given the unconditional stability of our algorithms, but this was not carried out: All experiments in this work were generated using uniform time steps). We maintain just 32 sets to track all the grains throughout this evolution, though the algorithm is able to add new sets whenever needed. For snapshots of the evolution, see Figure 3.1. These all show 1/64 of the full grain pattern. Figure 3.2 shows the final full grain pattern. Earlier time steps contain too many grains for the full pattern to be viewable on a single page.

Recall that the energy of the system is given by

$$E = \sum_{k<\ell} (\text{length of } \Gamma_{k\ell})$$

in two spatial dimensions (and by summing the interfacial area in three dimensions). In terms of the signed distance functions $d_k(x)$, this energy can be written in terms of the Dirac delta function, δ, as

$$E = \frac{1}{2} \sum_{k=1}^{k_{\max}} \int_\Omega \delta(d_k(x)) dx.$$

The factor 1/2 arises since this formula counts interfaces two times. We can discretize E, in two space dimensions, as

$$E = \frac{\Delta x^2}{2} \sum_k \sum_{i,j} \tilde{\delta}(d_k(x_i, y_j)). \tag{3.4}$$

We use a first–order discretization of the delta function, $\tilde{\delta}$, as proposed in [75]. The discrete version of Eq. (3.4) in three dimensions is similar. The energy, E, is evaluated at each iteration and found to be strictly decreasing at every time step.

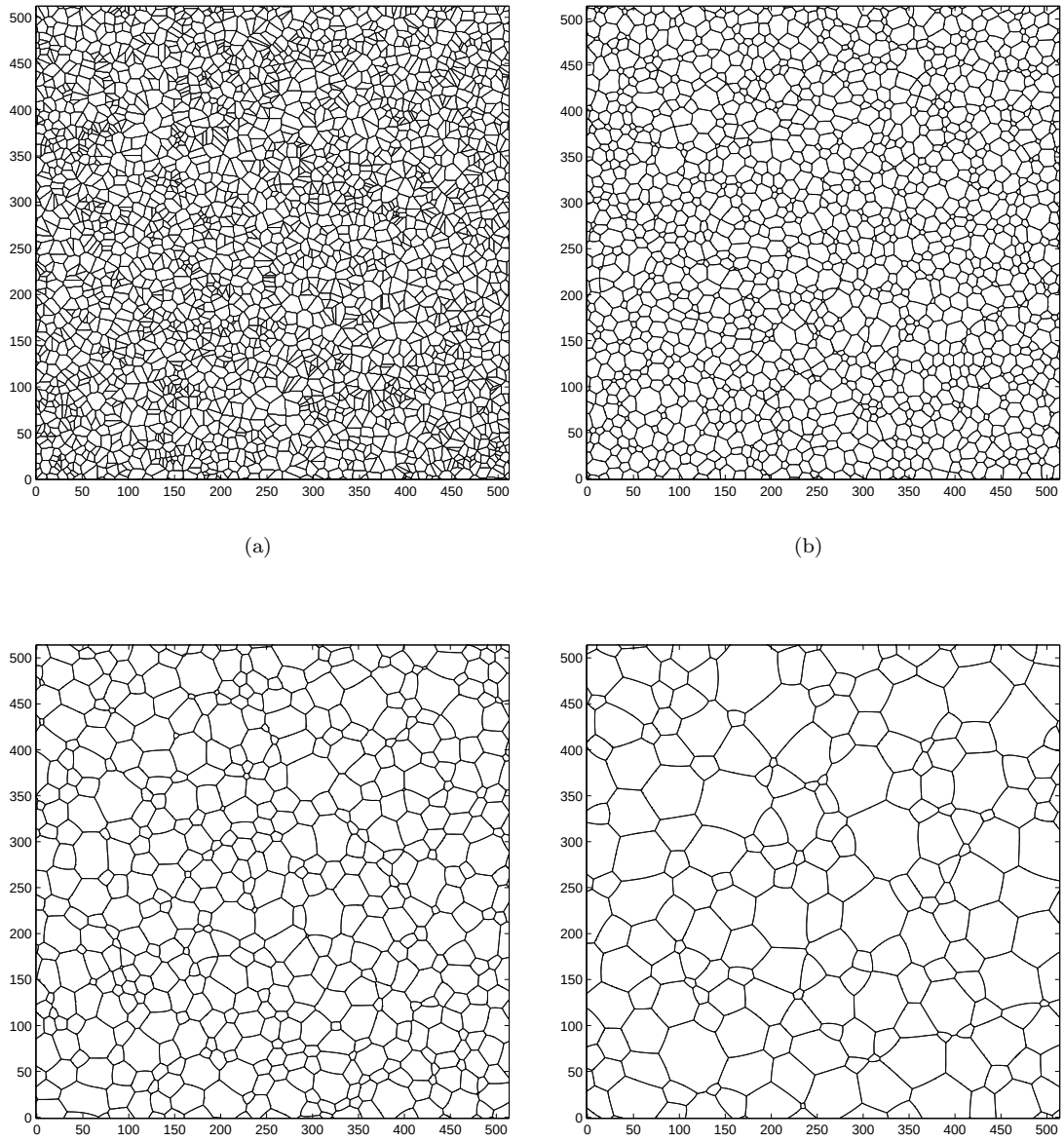

Figure 3.1: One 512×512 section of the full 4096×4096 grid. (a) Initial condition, $N(0) = 166,927$, (b) after 100 iterations, $N(100) = 97,000$, (c) after 500 iterations, $N(500) = 30,842$, (d) after 1500 iterations, $N(1500) = 11\,217$.

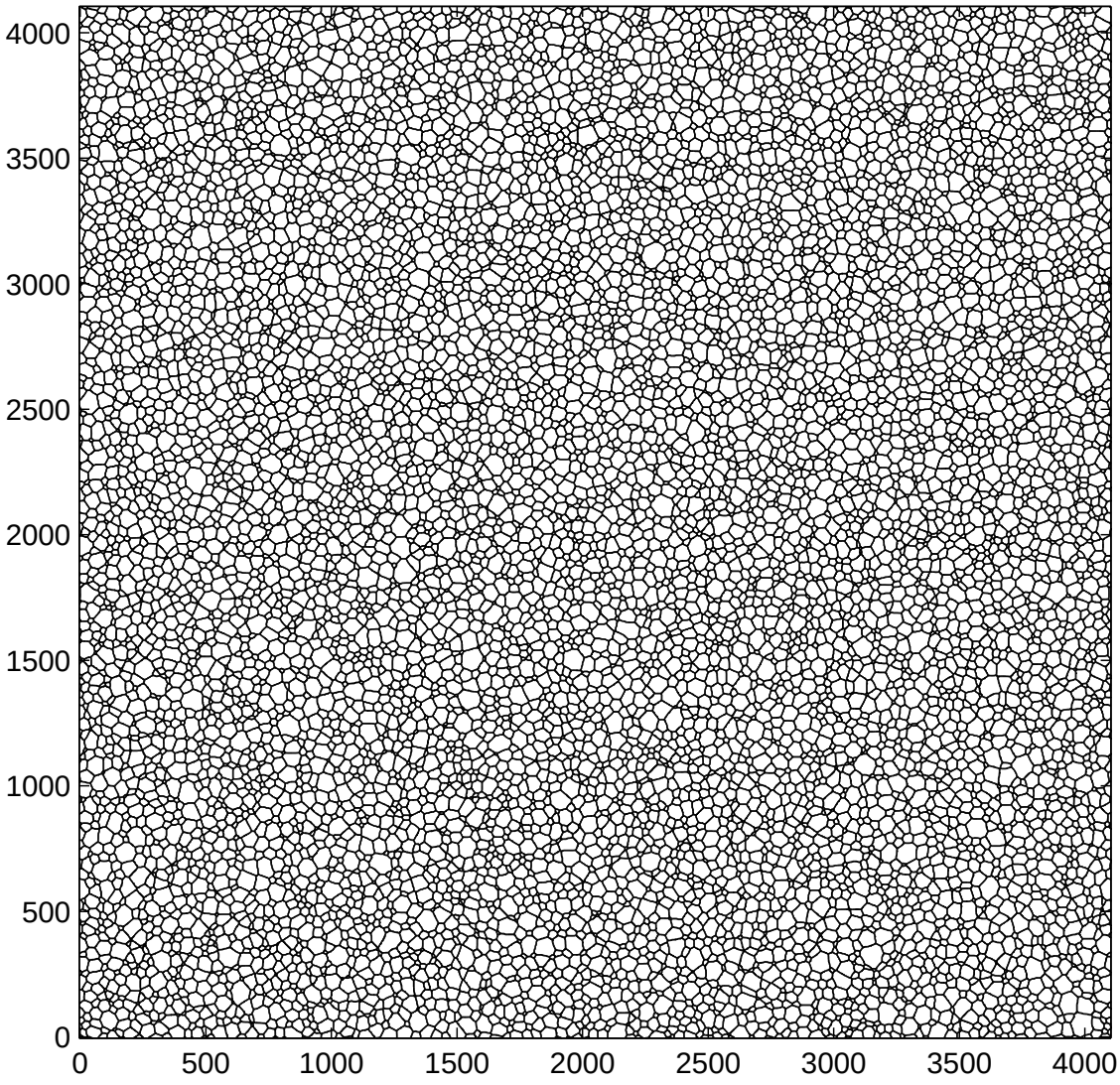

Figure 3.2: The full grain pattern after 1500 iterations for the simulation with $N(0) = 166,927$ grains initially. At the time shown, $N(1500) = 11,217$ grains remain.

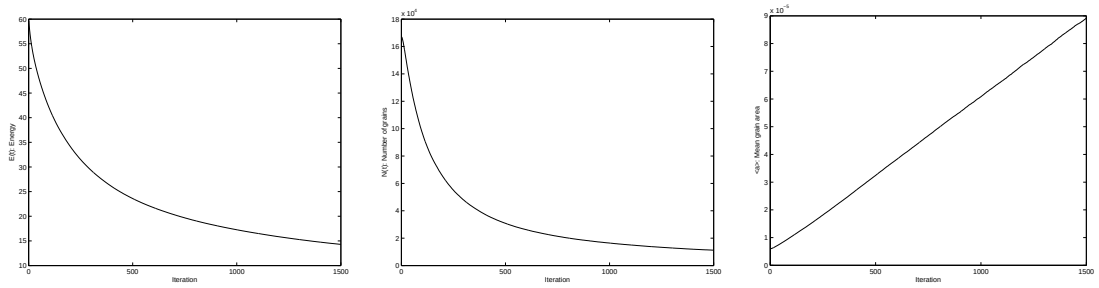

(a) (b) (c)

Figure 3.3: (a) The energy E decreases at every time step. (b) The number of grains $N(t)$ decreases such that (c) average grain area $\langle a \rangle$ grows linearly.

See Figure 3.3(a). Note that our method handles topological changes naturally, and that the energy of the system decreases even as more than 150,000 grains disappear throughout 1,500 iterations.

Several analytical approaches predict the mean grain radius $\langle r \rangle$ to grow as $\langle r \rangle \approx Ct^{1/2}$ (for example, see [26, 39, 53]). In normal grain growth, characterized by self–similarity of the distribution of $r/\langle r \rangle$, it immediately follows that the average grain area $\langle a \rangle$ is predicted to grow linearly as a function of time. We compute the average grain area as

$$\langle a \rangle = \frac{1}{N(t)},$$

where $N(t)$ is the number of grains surviving at time t, and see linear growth following a short relaxation time. This relaxation time is due to the initial condition, which we chose to be the Voronoi diagram for points distributed uniformly at random throughout the domain. Such an initial condition contains very few small grains and does not respect the Herring angle condition. Initially the evolution corrects the angle conditions and some time must pass before the smallest grains are found in the correct proportion so as to allow the mean grain area to increase linearly. See Figure 3.3, (b) and (c).

Two other measures of interest are the relative grain area distribution and the number of edges distribution, as defined in [49]. Let $G(n,t)$ be the proportion of grains with n grain boundaries at time t, and $F(\xi,t)d\xi$ be the number of grains with relative area in $[\xi, \xi + d\xi]$ at time t, with $\xi = a/\langle a \rangle$. Normal grain growth is characterized by the self–similarity of F as t varies. See Figure 3.4, which suggests that F is approximately self–similar for $t \geq 300\Delta t$.

Figure 3.5 shows the evolution of the number of edges distribution. Note that the maximum of this distribution is initally at 6 sides, then shifts to 5 sides and back to 6 sides as the evolution proceeds. This behavior was seen in multiple simulation runs. The number of edges distribution is of general interest and has been reported for both simulations [29, 45, 49, 74] and experiments [28]. The maximum has been found at both 5 and 6 sides. It is not known if this distribution should be self–similar through time as the relative grain area distribution is predicted to be.

3.2 Three-Dimensional Simulation

In this section, a large-scale simulation of normal grain growth in three dimensions is described and a wide variety of statistical measures on the resulting microstructure are reported. Here, and in subsequent simulations, we choose to set the mean initial grain volume $\langle V_0 \rangle = 1$. The simulation begins with 133,110 grains in the domain $\Omega = [0, 82.306]^3$ with periodic boundary conditions. The evolution runs for time $t = 6.2021$, allowing for over 90% of the initial grains to disappear. Ω is discretized as a regular cubic lattice of size $512 \times 512 \times 512$, and three hundred time steps are taken, ensuring adequate spatial and temporal resolution. The coarsening rate is shown to agree well with theoretical predictions. The grain size distribution is calculated; it exhibits self-similarity. This distribution is compared with a number of

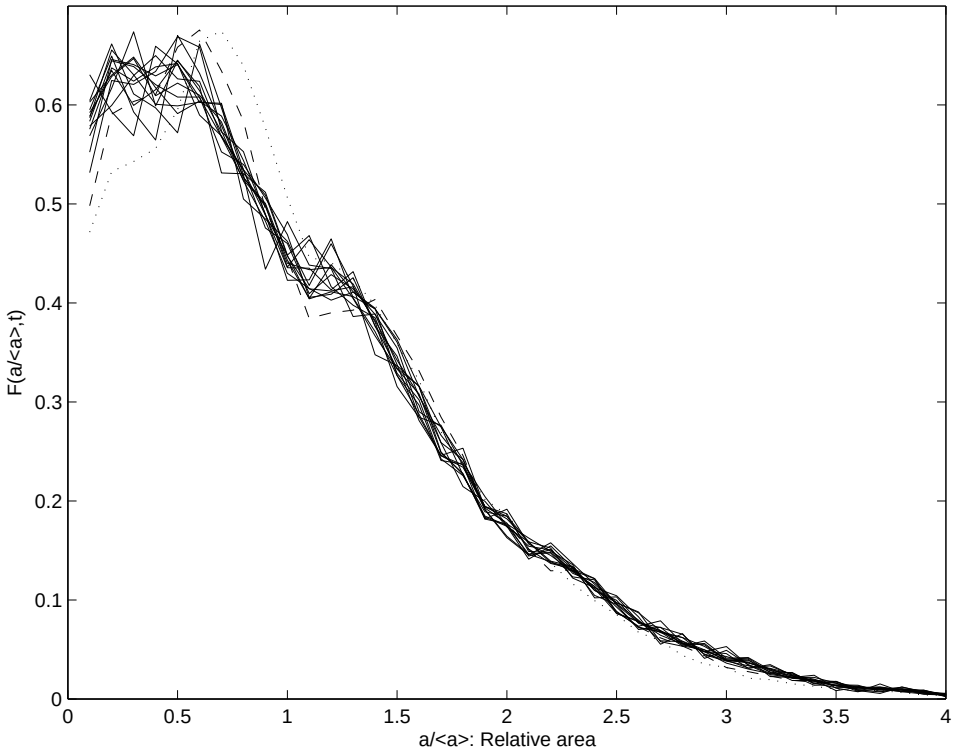

Figure 3.4: Relative area probability densities at 100, 200, ..., 1500 iterations. $G(n, 100\Delta t)$ is dotted, $G(n, 200\Delta t)$ is dashed, and the rest are plotted as solid lines.

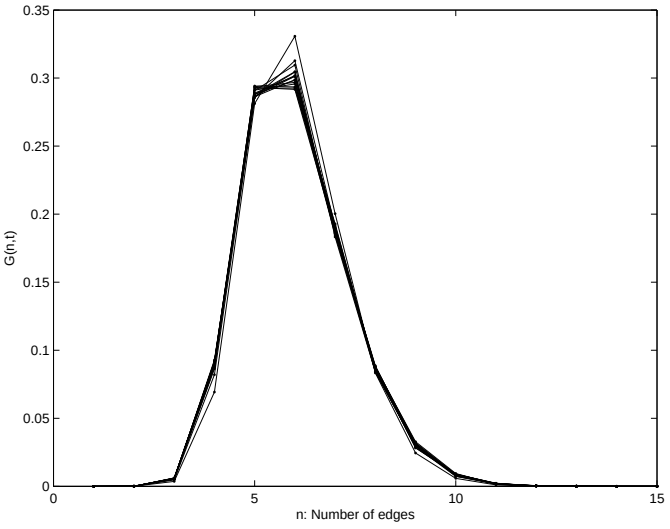

(a)

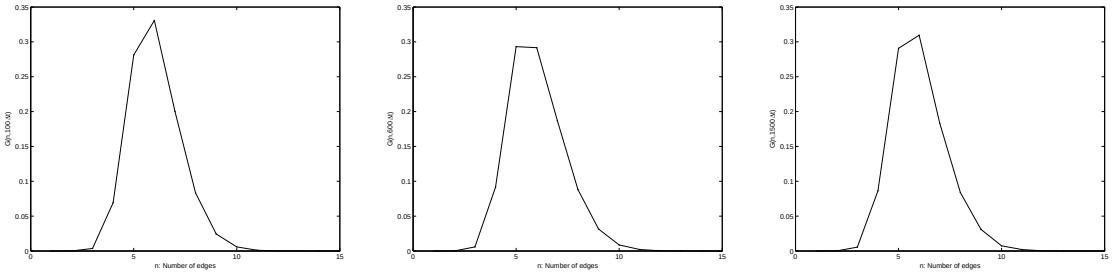

(b) (c) (d)

Figure 3.5: (a) Number of edges distribution at 100, 200, ..., 1500 iterations. (b)–(d) Number of edges distribution at 100, 600, and 1500 iterations. The proportion of grains with 6 edges falls off to a minimum at 600 iterations, then rises again through the end of the simulation.

different predictions from the literature. In addition, average numbers of grain edges, faces, and corners are computed and compared with other computational approaches and experimental data.

3.2.1 Qualitative Microstructure

We present a three-dimensional simulation with an initial condition containing 133,110 grains. The initial condition is taken to be the Voronoi diagram for 133,110 seeds placed uniformly at random in the computational domain Ω. Figure 3.6(a) shows a single grain of average size taken from the simulation at $t = 6.2021$. At this time, $\langle r \rangle = 2.11$ and $\langle V \rangle = 39.40$, indicating that mean grain radius has more than doubled the initial value and the mean grain volume is over 9 times the initial mean grain volume. The grain appears to be very well resolved. Its faces, edges, and corners are easy to see. The faces are smooth, and most appear to be concave. Thus this particular grain, which is of average size at this stage in the evolution, must be growing due to the curvature of its interfaces. Overall, the grain resembles what is observed in real materials, such as the beta brass grain shown in Figure 3.6(b).

The coarsening of the grain pattern is demonstrated by Figure 3.7. Here we display the grains intersecting the $x = 0$, $y = 0$ and $z = 82.306$ surfaces in the initial condition (a) and after 300 iterations (b). Different colors correspond to different grains. By volume, the average grain at the end of the simulation is nearly ten times as large as the average grain at initial condition. In Figure 3.8 we show all the grains from five of the sixty-four total set functions Ξ at $t = 2.0674$ and $t = 6.2021$. There is a great variability in the size of grains seen in this figure, from grains contained within a single grid cell (equivalent radius $r \approx 0.08$) which are about to disappear, to grains with radius $r \approx 4$.

Cross-sections of successive slices at $t = 6.2021$ are shown in Figure 3.9(a). Com-

(a) (b)

Figure 3.6: (a) Two views of a single grain (corresponding to a 180° rotation in the xy-plane) chosen from the evolution after 300 iterations. This grain has nondimensional size $\langle r \rangle = 2.11$, equal to the average grain size at this point in the evolution. The grain is very well resolved, with faces, edges, and corners all easily distinguished. (b) A single grain of beta brass, approximately 2 cm in diameter, from the collection of W.W. Mullins. The photograph is due to K. Barmak and D. Kinderlehrer. The grain compares well to the simulated grain shown in (a).

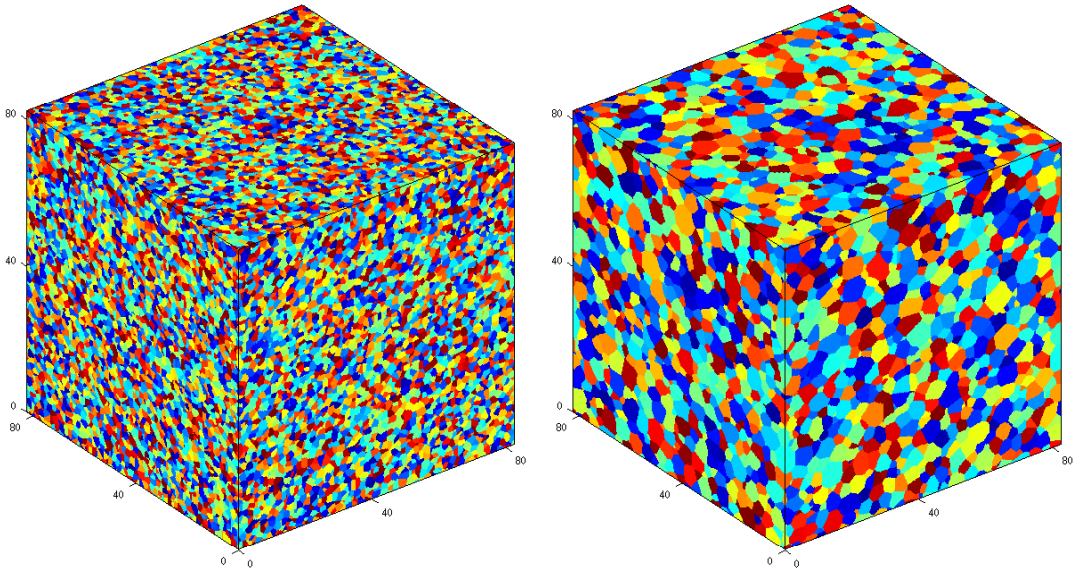

(a) (b)

Figure 3.7: Visualization of the grain pattern (a) at initial condition and (b) after 300 iterations. The initial condition contains 133,110 grains. At $t = 6.2021$, 14,150 grains remain.

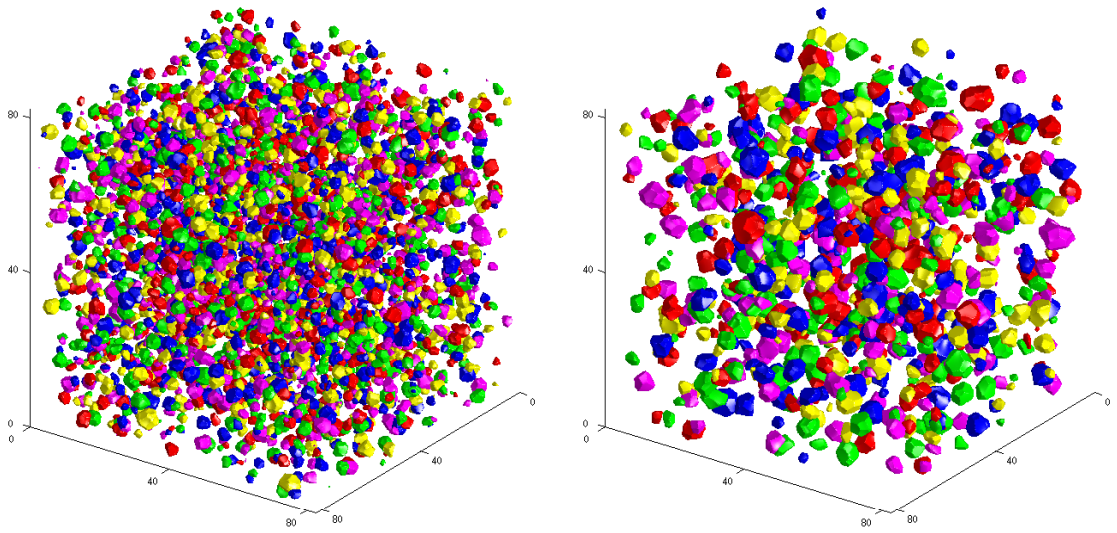

(a) (b)

Figure 3.8: Grains from five of sixty-four level set functions in the simulation with initially 133,110 grains, after (a) $t = 2.0674$ and (b) $t = 6.2021$. There are 54,197 and 14,150 total grains (in all sixty-four sets), respectively. Only a subset of grains is shown, as otherwise the entire volume would be filled.

pare to Figure 3.9(b), showing results from a fully two-dimensional simulation, in which all three junctions must have 120° angles. The cross-sectional views also feature more grains that are long in one dimension and short in the other as compared to the two-dimensional simulation results, where grains tend to be more regularly shaped.

3.2.2 Energetics

It is shown in [48] that, at least in the absence of topological changes, the surface energy E given by (3.3) decreases in time under mean curvature motion subject to the Herring angle condition at junctions. It is natural to expect that E would continue to decrease even through topological changes (critical events). We verified that our numerical scheme respects this fundamental behavior by evaluating the energy at every time step. We note that the energy E can be written in terms of the signed

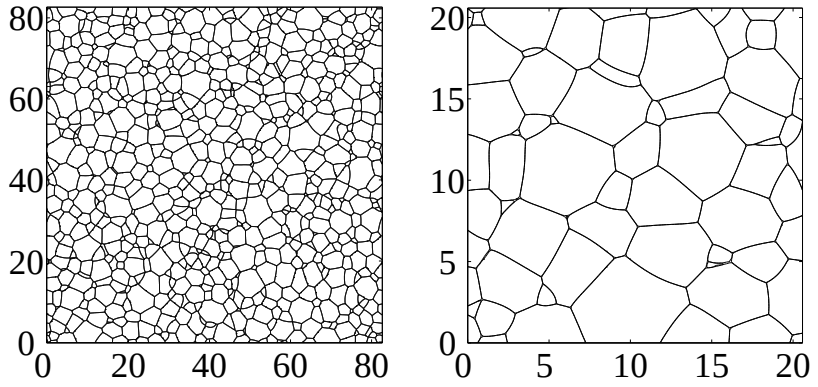

(a)

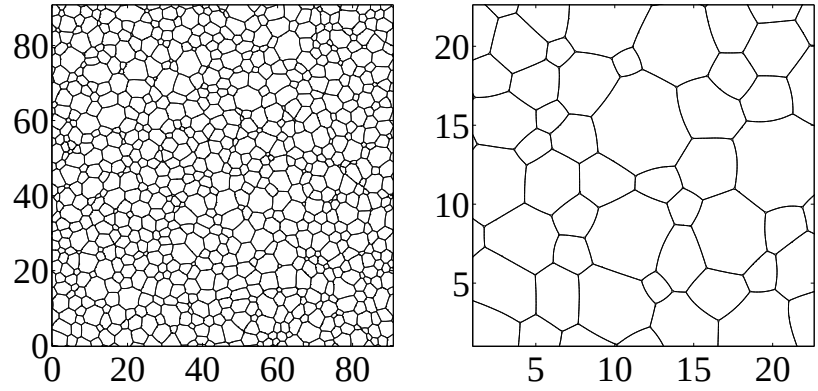

(b)

Figure 3.9: (a) A cross-sectional slice taken from simulation at $t = 6.2021$. The full slice is shown at left and zoomed in on at right. The curved nature of the interfaces is easily seen. The angles observed at triple junctions need not be 120° as the cross-section need not be oriented along the triple lines. (b) Two-dimensional simulation results. Triple junctions all meet at 120° angles and grain are more equiaxed, in contrast to the results seen in three-dimensional cross-section in (a).

distance functions $d_k(x)$ and the Dirac delta function, $\delta(x)$, as the following sum of integrals over the computational domain Ω:

$$E = \frac{1}{2} \sum_{k=1}^{k_{\max}} \int_{\Omega} \delta(d_k(x)) dx. \tag{3.5}$$

The factor of $\frac{1}{2}$ arises as this formula counts each interface twice. We discretize E as

$$E = \frac{\Delta x^2}{2} \sum_{k} \sum_{i,j,\ell} \tilde{\delta}(d_k(x_i, y_j, z_\ell)). \tag{3.6}$$

We utilize a first-order discretization of the delta function, $\tilde{\delta}$, following [75]. The energy E is measured at each time step and is found to decrease monotonically at every time step (see Figure 3.10(a)) even as the evolution naturally handles the topological changes involved in the disappearance of over 100,000 three-dimensional grains through $t = 6.2021$. The evolution of the number of grains is shown in Figure 3.10(b). After a short transition period (approximately $t = 0.4$), the number of grains in the system decreases steadily. Notice that even during this transition period, the energy of the system is decreasing quickly. The explanation for this transition period seen in the number of grains is that the initial condition is approximately Voronoi and so there are very few small grains present initially, as demonstrated in the distribution shown in Figure 3.12(a). The system must evolve significantly before many grains are small enough to disappear.

3.2.3 Grain Growth Rate and Grain Size Distribution

The average grain size, $\langle R_V \rangle$, and the grain size distribution function, $f(R_V/\langle R_V \rangle)$, are probably the most important statistical quantities used to characterize an isotropic polycrystalline material. Texture distributions are also of primary importance for anisotropic polycrystalline materials, but texture is not considered in this model. Here, $R_V = (3V/4\pi)^{1/3}$ where V is the volume of a grain. Analytical approaches

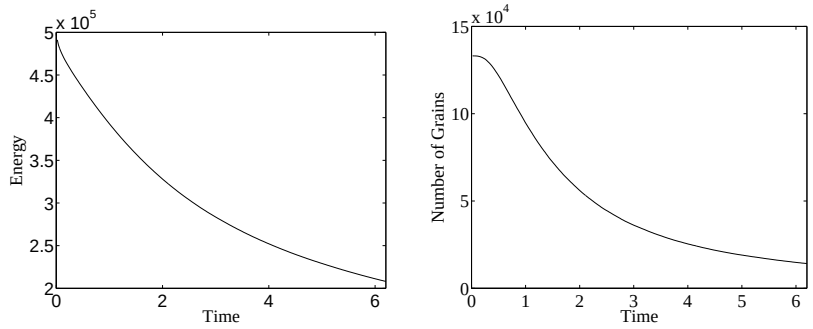

(a) (b)

Figure 3.10: (a) The energy $E = \sum_{i<j}(\text{area of } \Gamma_{ij})$ decreases monotonically at every iteration. (b) The number of grains N undergoes a short transition phase of slow decrease then decreases steadily from an initial value $N(0) = 133,110$ to a final value of $N(6.2021) = 14,150$.

[26,39,53], experimental results (as reported in [4]), and simulation results, e.g. [4,87], suggest that the average grain radius $\langle R_V \rangle$ exhibits power law growth as a function of time: $\langle R_V \rangle \approx Ct^n$, for t large. Analytically, the prediction $n = 1/2$ has been made using a variety of considerations. The experimental results reported in [4] find $1/4 \leq n \leq 1/2$. In their own simulation, [4] report that $n = 0.48 \pm 0.04$ for fits to long-time data (obtained by discarding data from the initial transition phase of the simulation). In [87], the authors show approximately linear long-time dependence of $\langle R_V \rangle^2$ on t. This simulation contains just 1000 grains initially, so the statistical precision of this measure is low. Furthermore, three-dimensional simulations via front tracking require that explicit assumptions be made on the types of topological changes that can occur.

As normal grain growth is characterized by the self-similarity of the distribution of $R_V/\langle R_V \rangle$, it follows that $\langle V \rangle \propto t^{3n}$. In Table 3.1, we fit $\langle V \rangle$ to the function $at^b + c$, where $c \approx \langle V_0 \rangle$ and mollifies the effect of the initial grain size distribution on the fit. The fits are quite tight, with all reliability factors $< 0.7\%$. Equating $b = 3n$, we

Time Interval	a	b	c	χ_1	χ_2	χ_3
$0 < t \leq 6.2021$	2.105	$1.550 \pm .004$	3.8617	3.79×10^{-3}	2.98×10^{-3}	2.29×10^{-3}
$1.0337 < t \leq 6.2021$	2.220	$1.524 \pm .003$	3.608	4.38×10^{-3}	2.28×10^{-3}	2.18×10^{-3}
$2.0674 < t \leq 6.2021$	2.260	$1.515 \pm .005$	3.496	4.86×10^{-3}	1.88×10^{-3}	1.57×10^{-3}
$3.1010 < t \leq 6.2021$	2.241	$1.517 \pm .013$	3.5144	6.05×10^{-3}	3.22×10^{-3}	2.89×10^{-3}

Table 3.1: c
onfidence interval] Fit of the data $\langle V(t) \rangle$, taken from the specified time interval, to $at^b + c$. b is given with 95% confidence interval. The reliability factor $\chi \equiv \sum_i |x_i^{obs} - x_i^{calc}| / \sum_i |x_i^{obs}|$, where *obs* denotes the observed value and *calc* denotes the calculated value from the fitted function. χ_1 gives the reliability factor computed over the interval $0 < t \leq 6.2021$, χ_2 over the interval $1.0337 < t \leq 6.2021$, and χ_3 over the interval $2.0674 < t \leq 6.2021$.

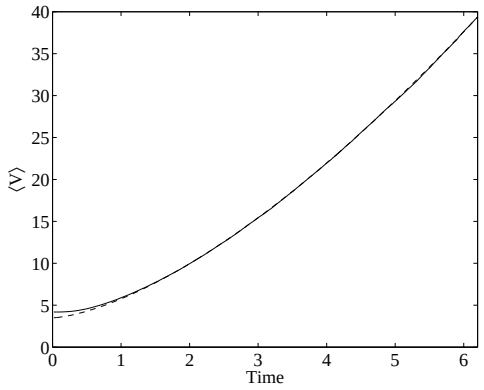

Figure 3.11: The average grain volume $\langle V \rangle$ compared to the best-fit power function $at^b + c$ fitted by non-linear least squares to the data from $2.0674 < t \leq 6.2021$ (see Table 3.1). Aside from the brief transition period, the fit is indistinguishable from the simulation results.

find that our simulation predicts $0.501 \leq n \leq 0.518$ with 95% confidence. The fit of $2.260t^{1.515} + 3.496$ to $\langle V \rangle$ is plotted in Figure 3.11.

The grain size distribution function $f(R_V/\langle R_V \rangle)$ is defined by

$$f(\xi)d\xi = \text{Proportion of grains with normalized radius } R_V/\langle R_V \rangle \in [\xi, \xi + d\xi). \tag{3.7}$$

In Figure 3.12, we show histograms for this distribution at a variety of stages in the simulation. The distribution changes greatly throughout the evolution. The initial condition is approximately the Voronoi diagram for a randomly distributed set of points. The initial distribution of grain sizes is very narrow and sharply peaked. The distribution flattens out rapidly and appears to approach a self-similar state,

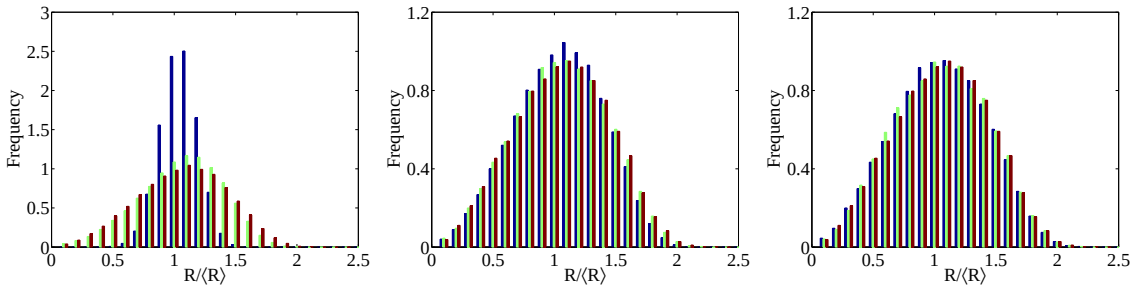

(a) (b) (c)

Figure 3.12: The distribution of $R_V/\langle R_V\rangle$ is shown at various times. (a) The distribution at $t = 0$ (blue), $t = 1.0337$ (green), and $t = 2.0674$ (red). The distribution is initially quite narrow but rapidly broadens. (b) At $t = 2.0674$, 4.1347, 6.2021. The distributions at $t = 4.1347$ and 6.2021 are slightly wider than at $t = 2.0674$ and exhibit self-similarity. (c) At $t = 4.1347$, 5.1684, and 6.2021, the grain size distributions appear to be self-similar, as expected in the long-term, though the number of grains in the system decreases from 24,395 to 14,150 in this timespan. Note that the scale in (a) differs from that in (b) and (c).

characteristic of normal grain growth. This self-similar distribution appears to be attained by approximately $t = 4.1347$ and is maintained thereafter, through over 10,000 grain disappearance events to the end of the simulation.

Another way to assess the self-similarity of the distribution of the grain size distribution function across iterations is to look at the evolution of the central moments of the various distributions obtained. For these distributions, the first moment is by definition 1 and the first central moment is always 0. The variance and skewness ($\mathbf{E}[(X - \mathbf{E}[X])^j]$, for $X = R_V/\langle R_V\rangle$ and $j = 2$ and 3, respectively) are plotted in Figure 3.13. These measures appear to be approximately constant for $t \geq 4.1347$, agreeing with the visual impression of self-similarity obtained from Figure 3.12(c).

Many closed-form distributions have been suggested as appropriate fits for the distribution $f(R/\langle R\rangle)$, including the Louat distribution [53], the Hillert distribution [39], the Rios distribution (a modification of the Hillert distribution) [70], the Weibull distribution (for two-dimensional grain growth) [25], and the log–normal distribution

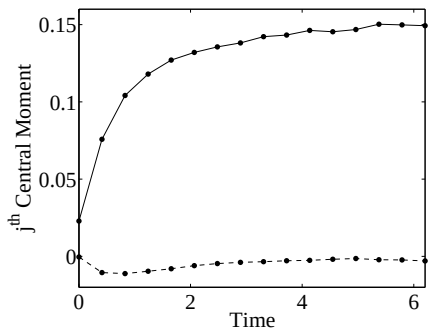

Figure 3.13: The variance (solid) and skewness (dashed) of the distribution of $R_V(t)/\langle R_V(t)\rangle$ are compared across iterations. While the variance of the distribution in particular changes rapidly early in the evolution, the variance and the skewness of the distribution are approximately constant for $t \geq 4.1347$, demonstrating the self-similarity of the distribution.

Grain size	log–normal			generalized Louat		Hillert	Rios		Weibull	
measure	μ	σ	χ	α	χ	χ	ν	χ	β	χ
R_A	0.074	0.574	0.335	0.685	0.152	0.389	2.14	0.221	2.07	0.171
R_V	0.056	0.417	0.282	0.741	0.330	0.128	3.34	0.031	2.80	0.104

Table 3.2: Least squares best-fit parameters and reliability factor χ for simulation data at $t = 6.2021$ (with 14,150 grains) to various distributions. The Rios distribution, with $\nu = 3.34$, fits the fully three-dimensional data very well. The observations made from two-dimensional cross-sections do not fit any of the distributions as well, but are best predicted by the generalized Louat distribution, with $\alpha = 0.685$. Note that the Weibull distribution does not fit the simulation distribution of $R_A/\langle R_A\rangle$ well, as the grain size distributions for two-dimensional growth and cross-sections of three-dimensional grain growth are known to disagree (for example, in [19]).

(for the distribution of grain radii in cross-sections of three-dimensional experiments) [26]. These distributions are compared to the distribution of $R_V/\langle R_V\rangle$ in Figure 3.14(a). The Rios distribution, with $\nu = 3.34$, appears to fit our simulation data the best. The log–normal and Louat distributions fit quite poorly, showing the wrong behavior near $R_V/\langle R_V\rangle = 0$, for large $R_V/\langle R_V\rangle$, and also peaking at $R_V/\langle R_V\rangle < 1$, all in disagreement with the simulation results. The Weibull and Hillert distributions show a better fit but can be seen both visually and by reliability factor (Table 3.2) to be inferior to the fit of the Rios distribution.

We also fit these distributions to data from cross-sections of the three-dimensional simulation. This is of interest as experimentally it is difficult to slice materials

thinly enough for the experiments to be two-dimensional in nature, though carefully conducted thin film experiments are possible for polycrystalline grains of sufficient size. Recent progress in x-ray and and focused ion beam techniques have made measurement of grain volumes more feasible. However, it is still easiest to take cross-sections of three-dimensional grains and measure areas and effective radii in cross-section. Defining $R_A = \sqrt{A/\pi}$, where A is the area of a grain in cross-section, we generate the distribution of $R_A/\langle R_A \rangle$ from the simulation data at $t = 6.2021$. We take 512 cross-sections of constant z-value and aggregate the grain slice area data across all these cross-sections to create the simulation distribution. These cross-sections contain a total of 368,138 two-dimensional grain slices. In Figure 3.14(b), we fit this distribution to the closed-form distributions discussed previously. None of these distributions fit the cross-sectional data as well as the Rios distribution fit the fully three-dimensional data taken from grain volumes. The Louat distribution fits the data the best with $\alpha = 0.685$ but with a reliability factor of $\chi = 0.152$. For comparison, the Rios distribution fits the three-dimensional data with $\chi = 0.031$. The distribution of $R_A/\langle R_A \rangle$ is seen in Figure 3.14 to be much flatter and wider than the distribution of $R_V/\langle R_V \rangle$, reemphasizing the importance of interpreting these distributions separately.

3.2.4 Topology

Interesting topological characteristics of the grain network include the number of faces, corners and edges of individual grains in three dimensions, and the number of edges of grains viewed in cross-section. Such characteristics have been the subject of numerous experimental studies (e.g. [15, 40, 69, 93, 94]). Here we compare the topological measures extracted from our large 3D simulation to those obtained from experimental data as well as to those from other simulations. In all the following

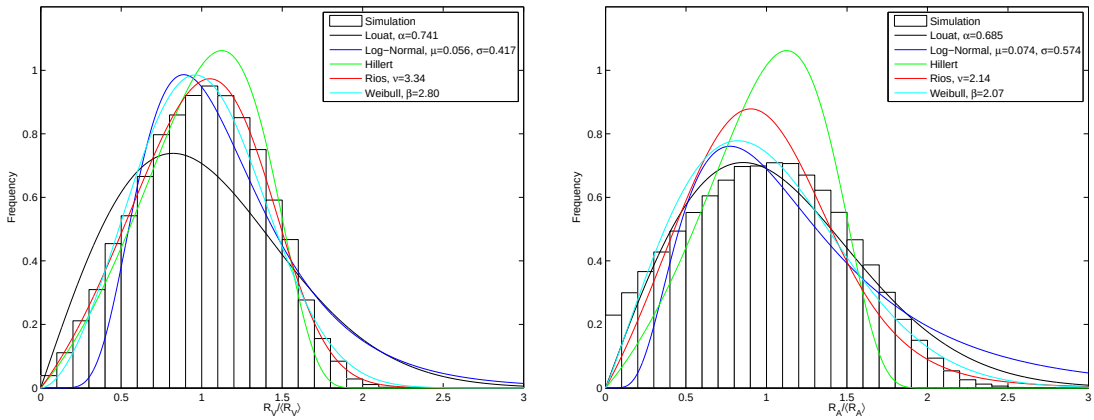

(a) (b)

Figure 3.14: (a) Comparison of the distribution of $R_V/\langle R_V\rangle$ at $t = 6.2021$ (with 14,150 grains) to least squares best-fit predictions to Louat, log–normal, Hillert, Rios and Weibull distributions. Note that the Louat, log–normal and Weibull distributions predict the peak of the distribution to occur at $R_V/\langle R_V\rangle < 1$, while the simulation distribution peaks to the right of 1. The peak of Hillert's distribution occurs at $R_V/\langle R_V\rangle = 9/8$, agreeing well with our simulation results. However, the Hillert's distribution predicts a higher peak and narrower distribution than we find in the normal grain growth phase. The Rios distribution is a modification of the Hillert distribution and matches the simulation results well. (b) Comparison of the distribution of $R_A/\langle R_A\rangle$ at 300 iterations (with 368,138 grains taken from the 512 cross-sections of constant z-value) to least squares best-fit predictions under the same distributions. In cross-section, the data best fits the generalized Louat distribution, though the fit is not tight. The distribution is much flatter and wider for cross-sectional data than for the full three-dimensional data.

results, we take data from $t = 6.2021$. At this time, 14,150 grains remain. In the 512 cross-sections of constant z-value, there are a total of 368,138 grain slices.

Unlike front tracking methods, methods using implicit representation of surfaces do not explicitly track topological features. The locations of these features are still well-defined: A location x is on a face, edge, or corner if for every $\varepsilon > 0$, there exist $m = 2, 3$ or 4, respectively, distinct subsets $c_1, \ldots, c_m$ and locations $x_1, \ldots, x_m$ satisfying $|x_i - x| < \varepsilon$ and $d_{c_i}(x_i) > 0$. The numerical implementation which allows association of topological descriptors to individual grains is described below. In order to count faces, corners and edges of individual grains at any fixed time T in the evolution, each grid point in the discretization is assigned a value from the set $\{1, \ldots, N(T)\}$ corresponding to the grain at that location. The number of faces of grain i is then the number of unique identifiers different from i contained in a 1-neighborhood of the set of grid points that have identifier i. Counting corners is more challenging. In three dimensions, corners are characterized as being locations where four or more grains come together. We denote the set of all such locations as C. Because adjacent grid locations may, as part of a highly resolved corner, be marked as each being such a location, we take the number of connected components of C (as opposed to simply the number of points in C) within a single grain to be the number of corners possessed by that grain. However, this procedure will cause two corners connected by a short edge to be counted as one. To alleviate this problem, we subdivide the grid twice before applying the above procedure (so that a grid of size $n \times n \times n$ is subdivided to size $4n \times 4n \times 4n$ before counting vertices). Having thus counted the number f of faces and the number c of corners as described above, we appeal to the well-known formula $c - e + f = 2$ of Euler to infer the number e of edges of each grain. This formula holds for all polyhedra that are topologically

equivalent to the sphere, which appears by inspection to be true for all the grains in our simulations of grain growth.

Data for the mean number of edges per face, mean number of faces, and mean number of corners is presented in Table 3.3 and compared to other simulations, to data reported for some regular polyhedrally-based grain models, and experimental results. The summary statistics vary some with the simulation technique. Ours are well within the range of values found with other simulation techniques (though the other simulations were smaller and must be less statistically valid whether due to a smaller number of grains or the potential effects of ensemble averaging). Regular polyhedra such as the pentagonal dodecahedron and the tetrakaidecahedron have been proposed as space-filling approximations for grain shapes [46, 58, 76, 92], though experimentally it is well-known that grains come in a variety of shapes and sizes. The tetrakaidecahdron matches the mean values we found well, but cannot explain more complex features of grain growth, such as the grain size distribution function (3.7). The Voronoi model is generated by distributing seeds uniformly at random and growing crystals simultaneously and isotropically from these seeds. The Johnson–Mehl model grows crystals isotropically but allows for varying nucleation times [58]. Both these models ignore grain boundary motion due to interface curvature, holding grain boundaries stationary once crystals meet. These are in fact models for primary recrystallization, a different annealing phenomenon occurring when cold-worked metals are annealed. The experimental data contains a wide range of values, clearly demonstrating the difficulty of computing these measures in three dimensions and also suggesting that other higher-order effects (such as variable surface tension and mobility due to grain boundary misorientation and inclination) play an important role in the evolution of polycrystalline grain systems. In future work, we will

	$2\langle e\rangle/\langle f\rangle$	$\langle f\rangle$	$\langle c\rangle$	Reference
Simulation	5.12	13.79	23.52	
Potts model Monte Carlo simulation	5.14	12.85	22.19	[4]
Potts model Monte Carlo simulation	—	13.7	—	[90]
Vertex dynamics	5.01	13.8	—	[91]
Phase field simulation	5.07	13.7	23.1	[51]
Surface Evolver simulation	5.05	13.5	22.6	[88]
Pentagonal dodecahedron	5	12	20	[77]
Tetrakaidecahedron	5.143	14	24	[76, 92]
Voronoi model	5.27	15.54	27.07	[58]
Johnson–Mehl model	5.10	13.27	22.56	[58]
Austenite grains	—	12.6–13.4	—	[52]
1015 α–iron grains	—	12.1	—	[94]
30 β-brass grains	5.142	14.5	24.852	[15]
β-brass grains	4.92	11.16	—	[40]
100 Al–Sn alloy grains	5.06	12.48	21.04	[93]

Table 3.3: Summary of topological data for simulations, regular polyhedra, and experiments. $2\langle e\rangle/\langle f\rangle$ gives the mean number of edges per face, while $\langle f\rangle$ and $\langle c\rangle$ give the mean number of faces and corners, respectively. In [52], the authors report that $\langle f\rangle$ increases as a function of annealing time, through 50 minutes.

investigate extending our algorithm so that such effects can be simulated.

In Figure 3.15, we plot the frequency with which grains with f faces occur. The distribution is skewed towards grains with many faces. The peak occurs at $f = 12$ faces and the mean number of faces is $\langle f\rangle = 13.79$. It is natural to expect that larger grains will have more faces, on average. However, the exact nature of this relationship is unknown. Figure 3.16 shows the relationship between the mean value of $R_V/\langle R_V\rangle$ for grains with f faces and f, as determined from our simulation data. We also compare with measurements made by Rhines and Patterson [69] on aluminum, by Zhang, et al. [94], on α-iron, and with simulation data generated by Anderson, et al. [4], using a Potts model and kinetic Monte Carlo techniques. The fit, particularly to the data for aluminum, is quite good and appears to describe the experimental data better than the linear fit posited in [4]. The simulation results of Anderson, et al., do appear to fit the measurements of Zhang, et al., well for small f, but poorly for large f.

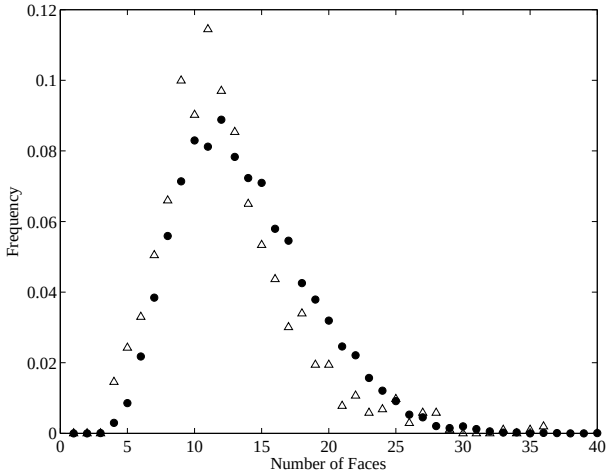

Figure 3.15: The proportion of grains with a given number of faces is plotted (solid circles). The peak occurs at $f = 12$ faces. Experimental data from [94] is also plotted (triangles). Note that this experimental data predicts a smaller mean number of faces (12.1) than other experimental and simulation data. See Table 3.3.

Stable corners occur where three triple lines come together on the surface of a grain. Under the assumption that every corner is stable, $3c = 2e$. Together with Euler's formula, we can then calculate the number of corners and edges as a function of the number of faces f as $c(f) = 2(f-2)$ and $e(f) = 3(f-2)$. This prediction of a linear relationship between c and f is plotted in Figure 3.17(a) against the values obtained from our simulation data, suggesting acceptable accuracy in our algorithm for counting corners and that our method does produce stable corners. Note that Figure 3.15 illustrates that very few grains have less than 4 or more than 30 faces, so small inaccuracies in the count or the presence of only a few unstable corners will cause the small deviations from the prediction shown.

The three-dimensional version of the Aboav–Weaire law [1, 89], proposed by Edwards and Pithia in [18] provides a relationship between the number of faces f exhibited by a grain and the mean number of faces of its neighboring grains, M_f:

$$M_f = \langle f \rangle - 1 + \frac{\langle f \rangle + \mu_f}{f}, \tag{3.8}$$

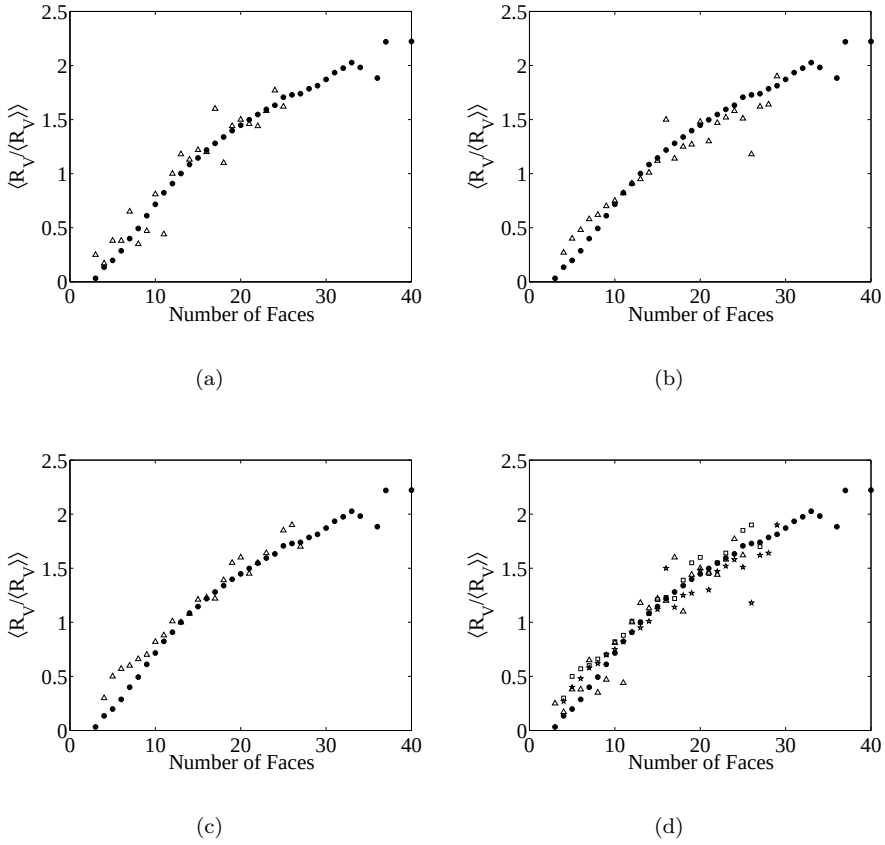

Figure 3.16: The relationship between the number of faces f and the mean value of $R_V/\langle R_V \rangle$ for grains with f faces is plotted (solid circles) and compared to (a) measurements for Al [69], reproduced from [4], (b) measurements reconstructed from serial sections of α-iron [94], (c) simulation data of Anderson, et al. [4]. In (d), all three are shown for comparison, with Al data marked by triangles, α-iron data by stars, and Anderson, et al. simulation data by squares.

where μ_f is the variance of f. Following Wakai, et al., [87], we plot the mean value of $\langle fM_f \rangle$ against f and find the linear relationship predicted by Edwards and Pithia, but find the best linear fit to be $fM_f = 13.6f + 25.4$. This is in good agreement with the results of Wakai, et al., who found $fM_f = 13.3f + 23.4$. Based on their experimental data, Zhang, et al. [94] found $fM_f = 13.97f + 12.61$. Equation (3.8) predicts $fM_f = 12.8f + 37.7$, using the values of $\langle f \rangle$ and μ_f determined by our simulation data. Thus simulation, experiment, and theory for the three-dimensional Aboav–Weaire law agree well up to an additive constant. See Figure 3.17(b) for simulation data and best fit line.

In two dimensions, the well-known von Neumann–Mullins relationship [63] states that grains with more than six sides grow, and grains with fewer than six sides shrink:

$$\frac{dA}{dt} = \frac{\pi}{3}(n-6), \tag{3.9}$$

where n is the number of sides of the grain. Mullins [64] proposed the following relationship for three dimensions, relating the mean growth rate of three-dimensional grains to their number of faces f:

$$\left\langle \frac{1}{R_V}\frac{dV}{dt} \right\rangle = F(f)G(f), \tag{3.10}$$

where

$$F(f) = \frac{\pi}{3} - 2\tan^{-1}\left(\frac{1.86\sqrt{f-1}}{f-2}\right) \tag{3.11}$$

and

$$G(f) = 5.35 f^{2/3}\left(\frac{f-2}{2\sqrt{f-1}} - \frac{3}{8}F(f)\right)^{-1/3}. \tag{3.12}$$

In Figure 3.17(c), we plot the simulation results for $\langle (dV/dt)/R_V \rangle$, taken from $5.9953 \leq t \leq 6.2021$. For $t = 6.0367$, 6.0780, 6.1194 and 6.1607, and $\delta t = 0.0413$ we approximate $dV/dt = (V(t+\delta t) - V(t-\delta t))/(2\delta t)$. The simulation results follow the same curve as the predictions but appear to differ by a constant additive

value of approximately 2.2. Our simulation results agree well with those of Wakai, et al. [87] (using Surface Evolver, a front-tracking software package), and Weygand and Bréchet [91] (via vertex dynamics). Other generalizations have been proposed by [90] and [38]. The Weaire relationship gives a linear relationship between f and $\langle (dV/dt)/R_V \rangle$ which does not appear to fit the data presented here or in other simulations well. The Hilgenfeldt relationship agrees closely up to a scaling constant with the von Neumann–Mullins extension for 10 and greater faces and is thus not shown.

Recently, MacPherson and Srolovitz [54] published a generalization of the von Neumann–Mullins relationship to three dimensions; however the quantities involved in their formula (mean width and total edge length) are not topological in nature, unlike the two-dimensional von Neumann–Mullins relation. Furthermore, mean width is quite difficult to calculate for grains. Simplifications are known for convex polyhedra ([12]) and for regular polyhedra ([32]), but grains are irregular and may possess both convex and concave faces. We elect to compare only to the Mullins generalization, which is a topological relationship depending only on the number of faces f.

3.3 Discussion

Algorithm 2.1 is applied to to two- and three-dimensional simulations of isotropic grain growth. This approach naturally captures the Herring condition at triple junctions. In addition, numerical evidence unequivocally shows that the energy of the simulated system decays, even through topological changes. The efficiency of this algorithm allows us to compute the accurate evolution of over 130,000 grains until less than 15,000 grains remain. To the best of our knowledge, this evolution contained at least twice as many grains as any other currently published to date. In

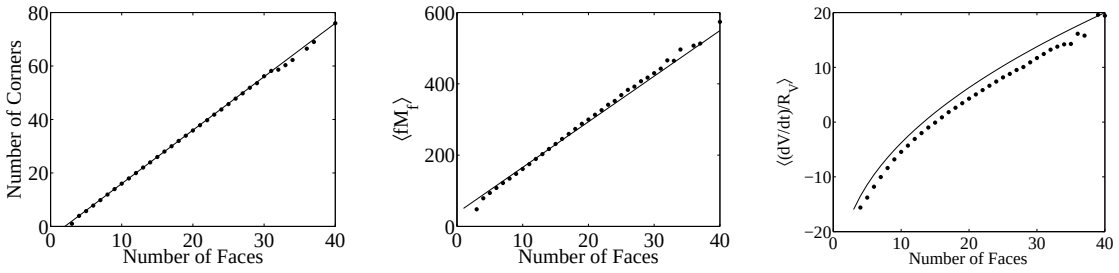

(a) (b) (c)

Figure 3.17: (a) There appears to be a linear relationship between the number of faces f and the mean number of corners among grains with f faces, suggesting that simulation corners are the stable meeting points of triple lines. (b) $\langle fM_f \rangle$, the mean of the product of the number of faces of a grain and the mean number of faces of its neighbors grows linearly as a function of f, matching well with the simulation results of Wakai, et al. [87]. (c) Comparison of the number of faces, f, to the mean growth rate $\langle (dV/dt)/R_V \rangle$ for grains with f faces. Simulation data from $5.9953 \leq t \leq 6.2021$ is plotted. The three-dimensional von Neumann-Mullins prediction is plotted as a solid line for comparison.

the next largest simulation, [81], the authors implement a phase field model initially containing 50,000 grains on a $512 \times 512 \times 512$ grid. Grains have an average initial size of approximately $14 \times 14 \times 14$ grid points, with a diffuse interface width ϵ of 3 grid points. This suggests that the initial resolution of their system is quite low. We are able to verify, with greater confidence, that the coarsening rate for normal grain growth is $\langle r \rangle \sim t^{1/2}$ and that the grain size distribution function is self-similar. We are also able to provide accurate average values of the number of edges, corners and faces of individual grains. We observe that in many cases these are in agreement with experimental results. This provides further validation that approximately normal grain growth is present in experimental settings.

CHAPTER IV

Application: Recrystallization

Recrystallization is an important process for microstructural development in polycrystals, occurring when cold-worked metals are annealed. This process has been studied for over seventy years. Burke and Turnbull [11] gave a classic review of recrystallization in 1952. For a more recent review, see, e.g., Doherty et al. [17]. The cold work stores energy in the form of dislocations which are then eliminated by the growth of undeformed recrystallized grains. Recrystallization occurs in the processing of metals, both as a deliberate attempt to improve macroscale properties (such as ductility) and as a byproduct of other processing steps. As such, it is important to develop numerical techniques to simulate this phenomenon well.

In this chapter, our focus is on careful numerics for a simple model of recrystallization, so that inherent, genuine features of the model can be understood in isolation from potential numerical artifacts that plague certain popular algorithms. We consider the simple, but influential, model of Srolovitz et al. [79, 80]. We present an analysis of the role of parameters in this model, and carry out detailed, large-scale, fully resolved simulations using Algorithm 2.3. We accomplish the following:

1. Determine the dependence of growth behavior of nuclei on distribution of nucleus sizes and nucleation rate for the model of Srolovitz et al.

2. Compare and contrast with Monte Carlo simulation results of [79, 80].

3. Simulate physical parameter regimes for this model unachievable with previous numerical methods in both two and three dimensions.

4. Show the formation of a very fine structure of elongated grains at the completion of recrystallization, unlike any other results from simulations of the model of Srolovitz et al.

5. Demonstrate agreement of our simulations with the growth behavior analysis we perform in Section 4.2.3, which describes the role played by the parameters of the nucleation and recrystallization models we employ in determining the resulting microstructure.

6. Show good agreement with some pre-existing theoretical predictions.

4.1 Recrystallization and Nucleation Models

The recrystallization and nucleation models studied in this work are identical to the models used in the landmark papers [79, 80] by Srolovitz et al. Recrystallized grains are differentiated from unrecrystallized grains by a lower bulk energy. In three dimensions, the total energy of the system is given by:

$$E = \gamma \sum_{k<\ell} (\text{area of } \Gamma_{k\ell}) + \rho \sum_{k} e_k (\text{volume of } \Xi_k), \tag{4.1}$$

where Ξ_k denotes a grain indexed by k, $\Gamma_{k\ell}$ denotes the interface between grains Ξ_k and Ξ_ℓ, γ denotes the grain boundary energy per unit area, ρ denotes the stored energy per unit volume, and e_k is a dimensionless parameter measuring the density of dislocations within the grain Ξ_k. For simplicity, we set $e_k = 1$ for unrecrystallized grains and $e_k = 0$ for recrystallized grains, though both the model and our imple-

mentation allow for varying dislocation densities. Normal grain growth occurs in the case that e_k is equal for all grains.

For the energy given by Equation (4.1), the normal velocity (outward from collection k) of the interface $\Gamma_{k\ell}$ can then be written as

$$v_n(\Gamma_{k\ell}) = \mu\left(\gamma\kappa_{k\ell} + \rho(e_\ell - e_k)\right). \tag{4.2}$$

Here, μ denotes the grain boundary mobility. $\kappa_{k\ell}$ denotes the curvature of the interface $\Gamma_{k\ell}$, with the convention that if Σ_k were a single spherical grain of radius r surrounded by a grain Σ_ℓ, then $\kappa_{k\ell} = -2/r$. The natural, energy-minimizing boundary condition is the Herring angle condition [36]. For constant γ, the Herring condition states that triples of grains (along triple lines in three dimensions and at triple junctions in two dimensions) meet with symmetric 120° opening angles. Commonly accepted values for the stored energy and the grain boundary energy densities are $\rho = 10\,MPa$ and $\gamma = 0.5\,J/m^2$ (see, for example, the texts of Gottstein and Shvindlerman [33], page 130, and Humphreys and Hatherly [41], page 8). When recrystallization nuclei are on the length scale of $0.05\,\mu m$ (so that $\kappa \approx 2 \times 10^7\,m^{-1}$), these two contributions to the normal velocity are on the same scale. However, at all length scales, the curvature term *always* has a definite, $O(1)$ effect on the evolution of the system. This effect is described further in Section 4.2.1.

We nondimensionalize the normal velocity using the mean initial grain radius $\langle r_0\rangle$, derived from the mean initial grain volume $\langle V_0\rangle$ by $\langle r_0\rangle = (3\langle V_0\rangle/(4\pi))^{1/3}$. We define the nondimensionalized curvature as $\kappa^\star_{k\ell} = \langle r_0\rangle\kappa_{k\ell}$. Then

$$v_n(\Gamma_{k\ell}) = \frac{\mu\gamma}{\langle r_0\rangle}\left(\kappa^\star_{k\ell} + \lambda(e_\ell - e_k)\right), \tag{4.3}$$

with

$$\lambda = \langle r_0\rangle\rho/\gamma. \tag{4.4}$$

λ is a dimensionless parameter which weights the relative contribution of the curvature and bulk energy terms. λ then may be interpreted as choosing the physical size of the unrecrystallized grains by $\langle r_o \rangle = \lambda \cdot 0.05\,\mu m$, for the physical values of ρ and γ discussed previously. We further nondimensionalize the velocity as $v_n(\Gamma_{k\ell}) = V \cdot v_n^\star(\Gamma_{k\ell})$, with velocity $V = \langle r_0 \rangle / T$, and time $T = \langle r_0 \rangle^2 / (\mu\gamma)$, so that

$$v_n^\star(\Gamma_{k\ell}) = \kappa_{k\ell}^\star + \lambda(e_\ell - e_k). \tag{4.5}$$

The normal velocity given by Equation (4.5) agrees with Equation (1.5) and arises as gradient descent for the energy of Equation (1.6) We note that the time scale T is chosen so that $t^\star = 1/4$ is the time required for an isolated spherical grain of radius $\langle r_0 \rangle$ to disappear under pure curvature motion. Hereafter, we drop the $\star$ notation and refer solely to the nondimensionalized quantities, e.g. the energy $E^\star$ will be referred to as E. The majority of the simulations presented in this work are in two dimensions. In this case, the energy of Equation (1.6) still applies, with "area" replaced by "length" and "volume" by "area."

An important feature of all recrystallization models is nucleation. In this respect, too, we shall follow the models proposed in [79] in which each spatial location is equally likely to be chosen as a nucleation site for a circular (spherical, in three dimensions) grain with a size probabilistically determined (but chosen to be small relative to the mean grain size). We observe that heterogeneities in the recrystallization pattern can arise as a consequence of the dynamics in certain length scales (in agreement with [80]). Further we shall consider two possible models for the nucleation, namely *site-saturated* and *continuous*. For site-saturated recrystallization a fixed number of grains are nucleated at the initial time and at random locations, while for continuous recrystallization grains are nucleated at a constant temporal rate at randomly chosen locations.

Since the work of Srolovitz et al. in [79, 80], more elaborate models for recrystallization have been proposed and implemented (for example, [42, 56, 65, 66]). These models include features such as modeling of the nucleation process in greater detail, inclusion of texture-dependent grain boundary mobility and energies, and spatially dependent stored energies. Extending our numerical algorithms to such models is a direction for future work. However, our improved capacity to faithfully simulate partial differential equation (PDE) models of the form of Equation (4.5) using Algorithm 2.3 already sheds new light on simulations of recrystallization. The properties of our algorithm allow for large-scale simulations far beyond those already performed, in physical parameter regimes that other algorithms cannot attain.

4.2 Importance of Surface Tension to the Model

In this section, we explain how the surface tension term in Equation (4.5) *always* makes a significant contribution to the evolution of the system, even when the bulk energy term would seem to dominate (i.e. as $\lambda \to \infty$). We discuss three major consequences:

1. In the absence of surface tension, it has been demonstrated by Reitich and Soner [68] that the evolution is not uniquely defined. In Section 4.2.1, we discuss two possible solutions for a given initial condition under pure bulk energy motion. Reitich and Soner note that one of these solutions naturally arises from Equation (4.5) as $\lambda \to \infty$ (with time appropriately rescaled).

2. For any choice of λ, no matter how large, the surface tension and bulk energy contributions of Equation (4.5) are comparable at some length scale, possibly at the length scale on which nucleation occurs in primary recrystallization. We discuss the relationship between λ and critical sizes for nuclei survival in Section

4.2.2.

3. The terms "homogeneous" and "heterogeneous nucleation" are used in [79,80] to describe the resulting spatial arrangement of surviving nuclei in simulations of primary recrystallization. We emphasize that nuclei are *always* placed uniformly at random among unrecrystallized sites; any "heterogeneities" in the location of *surviving* nuclei are determined by the parameters of the nucleation and evolution models of [79, 80] at we discuss here. In Section 4.2.3, we present analytical predictions for the location of successful nuclei as a function of λ (which scales the surface tension and bulk energy terms of Equation (4.5)) and distribution of nuclei sizes.

4.2.1 Importance of Curvature for Large λ

In the absence of the surface tension term in Equation (4.5), there is no need for the evolution to respect the Herring angle condition. However, Reitich and Soner [68] demonstrate that the evolution is not uniquely defined in this case. For example, consider Figure 4.1 in the case of pure bulk energy motion. Let $e_1 = 0$ and $e_2 = e_3 = 1$, so that set Σ_1 (as labelled in Figure 4.1(a)) grows symmetrically into sets Σ_2 and Σ_3. Figure 4.1(b) shows two potential solutions. The original interfaces Γ_{12} and Γ_{13} move outwards in their respective normal directions with constant velocity λ. Between the dotted lines, the classical solution does not exist. There is more than one reasonable way to propagate the solution in this region. The red path connects the unique regions by a circular arc. We call this the *arrival time dynamics* solution, and was proposed and investigated by Taylor in [82]. On the other hand, the blue path indicates another possible solution to gradient flow under pure bulk energy. Unlike in arrival time dynamics, this one maintains the initial angle at the triple

		$\lambda = 8$			$\lambda = 16$			$\lambda = 32$		
Δx	nt	Y_f	% Err.	C.R.	Y_f	% Err.	C.R.	Y_f	% Err.	C.R.
1/32	50	0.5630	3.28%	—	0.6259	6.04%	—	0.7323	7.62%	—
1/64	100	0.5599	2.72%	0.27	0.6094	3.25%	0.90	0.7090	4.21%	0.86
1/128	200	0.5539	1.60%	0.76	0.6016	1.92%	0.76	0.6989	2.72%	0.63
1/256	400	0.5504	0.97%	0.72	0.5973	1.20%	0.68	0.6922	1.73%	0.65
1/512	800	0.5485	0.61%	0.67	0.5947	0.76%	0.67	0.6881	1.13%	0.62

Table 4.1: Errors in approximating the vanishing surface tension limit using diffusion generated motion. The grid discretizes $[0,1]^2$ with steps of Δx, and nt denotes the number of time steps used to simulate the total time 5/1024. Y_f denotes the final vertical position of the interface. % Err. denotes the percentage error from the predicted location. C.R. denotes the convergence rate, computed as $\log_2$(Error using $n/2$ grid points/Error using n grid points).

junction throughout the evolution. In [68], Reitich and Soner show that this second solution arises as the limit of unique (well-defined) flows under the interfacial velocity of Equation (4.5) in the limit that $\lambda \to \infty$ (and with time appropriately rescaled). In other words, this second solution, called the *vanishing surface tension limit*, is the one selected from among multiple possible solutions. We maintain that the vanishing surface tension limit solution is the appropriate physical solution for grain boundary motion, as some surface tension must *always* be present, though it may be dominated by other effects. Given the $O(1)$ difference between these two candidate solutions, it is worth repeating that the surface tension plays a defining role on the dynamics even in the limit that bulk energy effects would seem to dominate, as observed in, e.g., the late stages of recrystallization.

In the recent paper [10], the authors claim to simulate pure bulk energy motion using a finite elements implementation of the level set method. Their method seems to capture the arrival time dynamics solution (the red arc in Figure 4.1(b)) described above; see, e.g., Figure 7 in [10]. In this section, we demonstrate that with our algorithm — diffusion generated motion — we capture the *vanishing surface tension* limit by taking large values of λ in Equation (4.5). Figure 4.2 shows the convergence

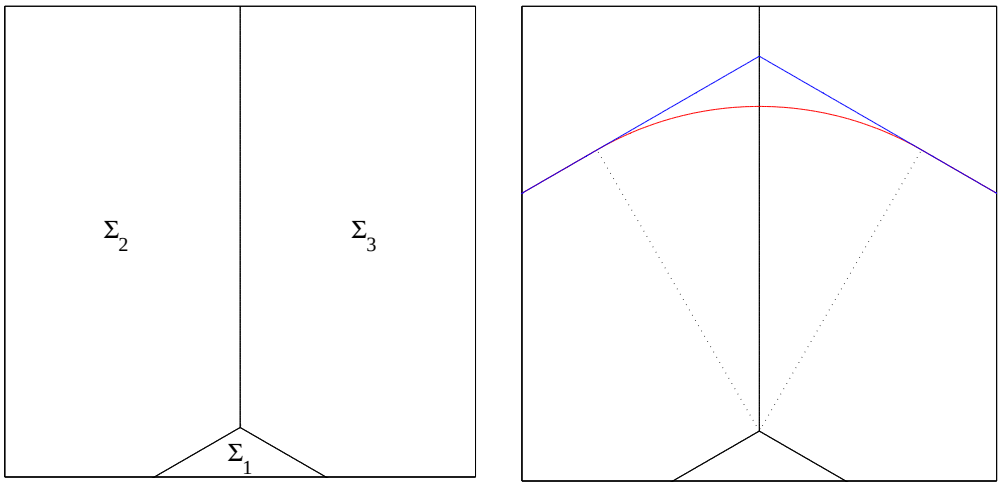

(a) (b)

Figure 4.1: The initial condition in (a) evolves by pure bulk energy motion. Two possible solutions to the non-unique motion are shown in (b), one in red, the other in blue. The red curve, consisting of a circular arc connecting two straight line segments, depicts the *arrival time dynamics* solution. The blue curve, which maintains the original angle condition at the triple junction throughout the evolution, represents the *vanishing surface tension* solution of Reitich and Soner [68]. Thus, even in the limit $\lambda \to \infty$, the mere presence of curvature effects (which always dominate in a small enough neighborhood of the triple junction) has $O(1)$ effect on the dynamics regardless of how large λ is in Equation (4.5), thereby selecting a specific pure bulk energy motion solution from a multitude of possibilities in the limit $\lambda \to \infty$.

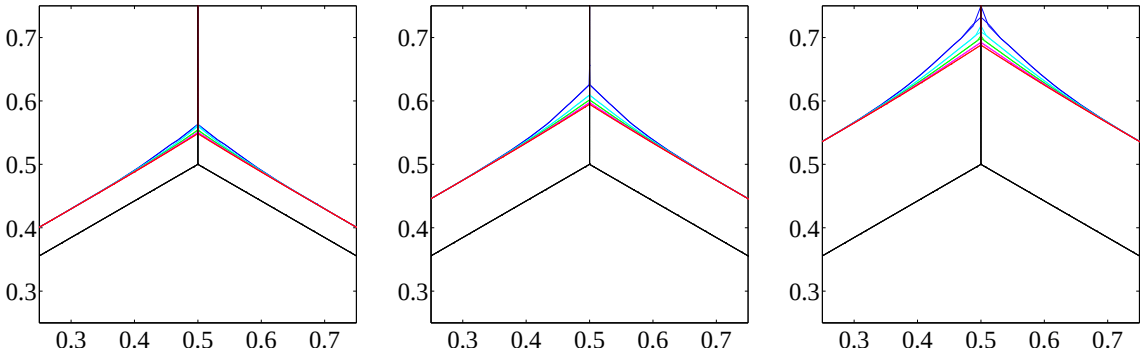

(a) (b) (c)

Figure 4.2: Comparisons with the vanishing surface tension limit (a translation of the black initial curve) as Δx and Δt are refined in our algorithm for motion by Equation (4.5) with (a) $\lambda = 8$, (b) $\lambda = 16$, and (c) $\lambda = 32$. The computed solution at successively higher resolutions are shown in blue, cyan, green, magenta, and red, respectively.

of our algorithm as $\Delta x,\ \Delta t \to 0$ as $\lambda = 8$, 16, and 32. Table 4.1 contains the convergence test data. The predictions for the final locations of the interface were calculated by finding the intersection of the two lines determined by advancing the interfaces Γ_{12} and Γ_{13} with velocity λ for the simulation time 5/1024. These values were calculated to be 0.5451, 0.5902 and 0.6804, for $\lambda = 8$, $\lambda = 16$, and $\lambda = 32$, respectively. These simulations are quite accurate, with relative errors under 5% for $n = 64$ grid points and under 2% for $n = 256$ grid points. The grid discretizes $[0, 1]^2$. We note that λ acts as a stiffness parameter: increasing λ requires increased computational effort for fixed accuracy. Even in the extreme case, $\lambda = 32$, the triple junction moves only between 0.5 and 0.75 on the vertical axis, suggesting that good accuracy is achieved for motions using only about one–fourth the available grid points in each direction. The convergence rate is sublinear but agrees well with convergence rates seen at triple junctions for pure curvature motion via the same algorithm in [22].

Furthermore, the surface tension plays a decisive role even in the limit that it vanishes in determining the characteristic shape of recrystallized nuclei growing along pre-existing grain boundaries. Rather than the nucleus appearing as a growing circle overlapping the pre-existing boundary (as in solutions computed in [10]), the nucleus takes on an elongated shape along the boundary, as in Figure 4.3. This shape can be derived as a self-similar solution for pure bulk energy motion respecting the Herring angle condition at triple junctions. It is described as a function of the circular sector radius r by:

$$y(x;r) = \begin{cases} \pm\sqrt{r^2 - x^2}, & |x| \le \frac{\sqrt{3}r}{2} \\ \pm\sqrt{3}\left(x \pm \frac{\sqrt{3}r}{2}\right) \pm \frac{r}{2}, & \frac{\sqrt{3}r}{2} \le |x| \le \frac{2r}{\sqrt{3}} \end{cases} \tag{4.6}$$

This shape is *independent* of the choice of λ: as long as a nucleus along a pre-

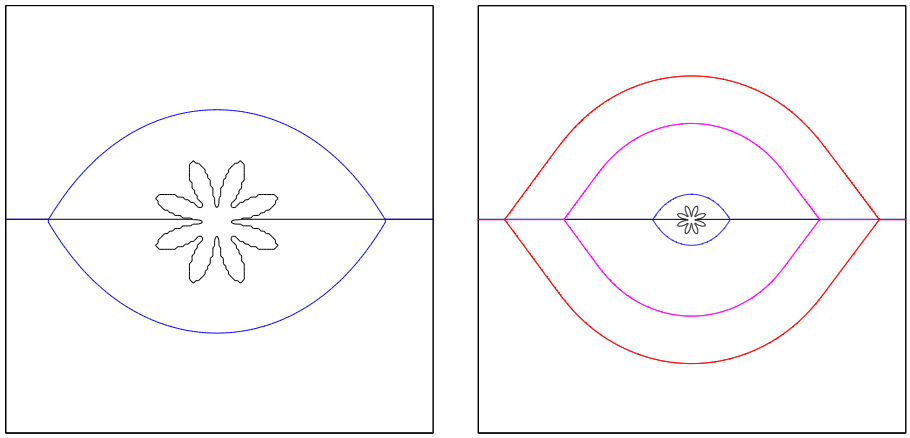

(a) (b)

Figure 4.3: Any initial shape which is sufficiently large for the choice of λ will grow; and as the ratio $\lambda/\kappa \to \infty$ will approach the characteristic shape described by Equation (4.6). In contrast, arrival time dynamics predict the asymptotic shape to be a disk, demonstrating again the $O(1)$ difference between the two possible definitions of a solution. The initial condition is zoomed in on in (a). Later times in the evolution are shown in (b), with the characteristic shape of circular arcs connected by line segments seen clearly.

existing boundary survives and grows, it will penetrate the existing unrecrystallized grains. The aspect ratio of the shape is $2 : \sqrt{3}$. In contrast, the arrival time dynamics solution has the disk as its characteristic shape, regardless of the pre-existing structure beneath the nucleus. We demonstrate that our algorithm evolves towards the self-similar solution even from a highly complex initial condition that does not respect the boundary conditions, as shown in Figure 4.3.

4.2.2 Critical Nuclei

For the model considered in this work, the curvature term contributes at the same order as the bulk energy term on the length scale $1/\lambda$; this is just a simple fact of the scaling in Equation (4.5). One of the appealing attributes of this model developed by Srolovitz et al. in [79, 80] is the potential for capturing various recrystallization phenomena, e.g. homogeneous or heterogeneous nucleation, through the effect sur-

face tension may play at the scale of the smallest recrystallized embryos. An exact, though unstable, stationary solution is easily determined from Equation (4.5) for any λ. These critical nuclei are those with constant curvature $\kappa = -1/\lambda$ away from triple junctions, with 120° angles at all triple junctions. Thus the stationary boundary must always be the union of circular arcs. As in the case of pure bulk growth, the stationary shapes have aspect ratios independent of λ. We consider three cases: (1) a nucleus contained entirely within another grain, (2) lying on a grain boundary, and (3) lying on a triple junction. We further assume that the nucleus is small compared to the original grains and make the two following approximating assumptions: the pre-existing grains have straight boundaries, and the nucleus lies with its centre on the grain boundary or triple junction, as appropriate.

Case (1) is trivial: The grain is a circle of radius $r = 1/\lambda$, with area $A_1(\lambda) = \pi\lambda^{-2}$. For case (2), assume the grain boundary lies along the line $y = 0$. Then the shape is implicitly represented as

$$\begin{cases} x^2 + \left(y + \frac{1}{2\lambda}\right)^2 = \lambda^{-2}, & y > 0, \\ x^2 + \left(y - \frac{1}{2\lambda}\right)^2 = \lambda^{-2}, & y < 0, \end{cases} \tag{4.7}$$

with area $A_2(\lambda) = \left(\frac{2\pi}{3} - \frac{\sqrt{3}}{2}\right)\lambda^{-2}$. Finally, we may rotate the triple junction of case (3) so that the grain boundaries emanate along the rays $\theta = \pi/2, 7\pi/6$ and $11\pi/6$. This shape is given by:

$$\begin{cases} \left(x + \frac{1}{2\lambda}\right)^2 + \left(y + \frac{1}{2\sqrt{3}\lambda}\right)^2 = \lambda^{-2}, & \theta \in (-\frac{\pi}{6}, \frac{\pi}{2}), \\ \left(x - \frac{1}{2\lambda}\right)^2 + \left(y + \frac{1}{2\sqrt{3}\lambda}\right)^2 = \lambda^{-2}, & \theta \in (\frac{\pi}{2}, \frac{7\pi}{6}), \\ x^2 + \left(y - \frac{1}{\sqrt{3}\lambda}\right)^2 = \lambda^{-2}, & \theta \in (\frac{7\pi}{6}, \frac{11\pi}{6}), \end{cases} \tag{4.8}$$

with area $A_3(\lambda) = \left(\frac{\pi - \sqrt{3}}{2}\right)\lambda^{-2}$. These shapes are shown in Figure 4.4. Note the

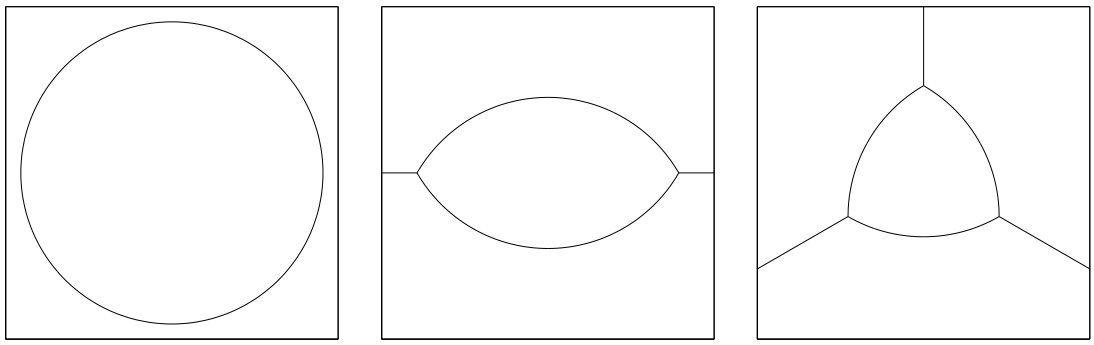

(a) (b) (c)

Figure 4.4: The critical shapes corresponding to cases 1 (grain interior), 2 (grain boundary) and 3 (triple junction), respectively. The shapes are independent of λ, while their areas scale with λ^{-2}.

constant curvature in smooth regions and that the Herring condition is satisfied at triple junctions.

We define the critical grain radii to be the effective grain radius of the critical shape, $R_i = \sqrt{A_i(\lambda)/\pi}$, and calculate these from to be:

$$R_i = \begin{cases} \frac{1}{\lambda}, & i = 1, \\ \frac{\sqrt{2/3-\sqrt{3}/(2\pi)}}{\lambda}, & i = 2, \\ \frac{\sqrt{1/2-\sqrt{3}/(2\pi)}}{\lambda}, & i = 3. \end{cases} \tag{4.9}$$

Thus $R_2 \approx .6253/\lambda$ and $R_3 \approx .4736/\lambda$, for any choice of λ. We conclude that for fixed λ, *the critical grain size necessary for nucleus survival is smallest at triple junctions, moderate at grain boundaries, and largest in grain interiors.* This observation has been verified experimentally and in simulations by numerous previous authors.

4.2.3 Parameter Regimes

In this section, we give a complete classification of the role of parameters in the nucleation and recrystallization model used here and in the work of Srolovitz et al. [79, 80] with regard to their effect on the type of recrystallization (homogeneous

or heterogeneous) that results. The understanding developed here will guide our numerical experiments with the model in subsequent sections.

Let R be the (random) size of a circular nucleus, given by some distribution f_R, and let T_i be the event that a nucleus touches exactly i different grains (corresponding to the cases of Section 4.2.2). To approximate the conditional probability $\mathbb{P}(T_i|R = r)$, we note the following facts:

- The total area of the nondimensionalized domain Ω is $|\Omega| = \pi N_0$, where N_0 is the initial number of unrecrystallized grains.
- Assuming grains are approximately circular, the total boundary length is πN_0, as each individual grain has boundary length 2π, and each segment of grain boundary is counted by two grains.
- One implication of the von Neumann area law [63] is that the mean number of triple junctions along the boundary of one grain must be 6. Thus the number of triple junctions in the system must be $2N_0$, as each triple junction is counted by three grains.
- A nucleus of radius r must have its centre within r units of a grain boundary or a triple junction in order to be touching 2 or 3 different grains, respectively.

We define $\Omega_i \subset \Omega$, for $i = 1, 2, 3$, to be region where a nuclei of radius r touches exactly i pre-existing grains. Thus Ω_3, the region in which a grain of radius r must be centred to touch a triple junction, has $|\Omega_3| \approx 2N_0 \cdot \pi r^2$. Similarly, we conclude from the total boundary length that $|\Omega_2 \cup \Omega_3| \approx \pi N_0 \cdot 2r$. Since $\Omega_2 \cap \Omega_3 = \emptyset$, we

conclude that

$$\mathbb{P}(T_i|R=r) \approx \begin{cases} 1-2r, & i=1, \\ 2(r-r^2), & i=2, \\ 2r^2, & i=3, \end{cases} \tag{4.10}$$

if nuclei are placed uniformly at random within Ω.

Further let G be the event that a given nucleated grain grows. Numerically, we find that the critical radii for initially circular nuclei are very close to the values found analytically for the critical shapes described in Section 4.2.2:

$$R_i \approx \begin{cases} \frac{1}{\lambda}, & i=1, \\ \frac{.642}{\lambda}, & i=2, \\ \frac{.484}{\lambda}, & i=3. \end{cases} \tag{4.11}$$

To further validate this numerical result, we consider nuclei which are initially circular. In this case, we can give an upper bound on the critical radii as $R_2 \leq 2/(3\lambda)$ and $R_3 \leq 1/(2\lambda)$. This follows from the expression for the rate of change of area of a recrystallizing grain Σ:

$$\frac{dA}{dt} = \frac{\pi}{3}(N_e - 6) + \lambda \operatorname{Per}(\Sigma), \tag{4.12}$$

where N_e is the number of edges (equivalently, the number of neighboring grains) of grain Σ. The isoperimetric inequality guarantees that if $dA/dt \geq 0$ for some time interval $[0, t^\star]$, then $\operatorname{Per}(\Sigma(t^\star)) \geq \operatorname{Per}(\Sigma(0))$, as the circular initial condition has minimal perimeter among all shapes with area $\geq A(0)$. Thus, choosing the critical radii above guarantees that $dA/dt \geq 0$ for all subsequent times. Equation (4.12) shows that the critical nucleus size depends only on the perimeter of the nucleus and the *number* of grains neighboring the nucleus; but is independent of *where* on the

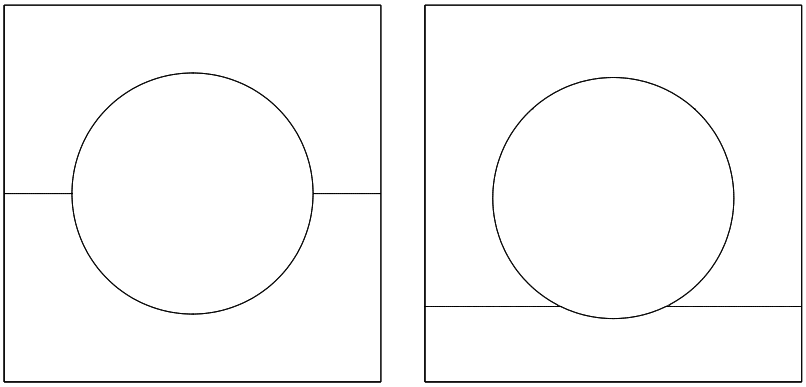

(a) (b)

Figure 4.5: The critical grain size for circular nuclei is found analytically and numerically to be independent of where on the nucleus the grain boundary crosses, either (a) at nucleus centre, or (b) near the edge of the nucleus.

nucleus the triple junctions occur. We numerically verified that the critical grain size is minimally affected by varying where the nucleus touches the grain boundary or triple junction, finding a difference of approximately 0.2% in critical grain radii for circles nucleated with their centres at the grain boundary (as in Figure 4.5(a)) as compared to circles nucleated so that the grain boundary is near the edge of the nucleus (see Figure 4.5(b)).

Therefore we have

$$\mathbb{P}(G \cap T_i | R = r) = \begin{cases} \mathbb{P}(T_i | R = r), & r > R_i \\ 0, & r < R_i, \end{cases} \tag{4.13}$$

where R_i is given by Equation (4.11). Then we can compute

$$\mathbb{P}(G \cap T_i) = \int_{-\infty}^{\infty} \mathbb{P}(G \cap T_i | R = r) f_R(r) dr = \int_{R_i}^{\infty} \mathbb{P}(T_i | R = r) f_R(r) dr. \tag{4.14}$$

It is surely of interest to describe the locations of nuclei that will survive in this model. The conditional probabilities describing the distribution of surviving nuclei

locations is given by:

$$\mathbb{P}(T_i|G) = \frac{\mathbb{P}(G \cap T_i)}{\sum_{i=1}^{3} \mathbb{P}(G \cap T_i)}. \tag{4.15}$$

An instructive first case is to suppose that the nucleation radius R is deterministic, i.e. $f_R(r) = \delta(r - \mu)$, where δ denotes the Dirac delta. Then there are four cases:

1. $\mu > R_1 > R_2 > R_3$: Grain grow regardless of where they are placed, and

$$\mathbb{P}(T_i|G) = \begin{cases} 1 - \mu, & i = 1, \\ 2(\mu - \mu^2), & i = 2, \\ 2\mu^2, & i = 3. \end{cases} \tag{4.16}$$

2. $R_1 > \mu > R_2 > R_3$: Grains only grow along grain boundary or at triple junctions, with

$$\mathbb{P}(T_i|G) = \begin{cases} 0, & i = 1, \\ 1 - \mu, & i = 2, \\ \mu, & i = 3. \end{cases} \tag{4.17}$$

3. $R_1 > R_2 > \mu > R_3$: Grains grow only at triple junctions. $\mathbb{P}(T_3|G) = 1$.

4. $R_1 > R_2 > R_3 > \mu$: Grains do not grow. Recrystallization cannot occur in the absence of of phenomena beyond the scope of the approximations made here (for example, the presence of quadruple or higher-order junctions, severely kinked grain boundaries, or interactions between nuclei).

These cases partition the μ–R_1 parameter space into four regions, as shown in Figure 4.6.

More generally, one might suppose that the grain radii are approximately normally distributed with some mean μ and variance σ^2. Taking care to ensure that $R > 0$,

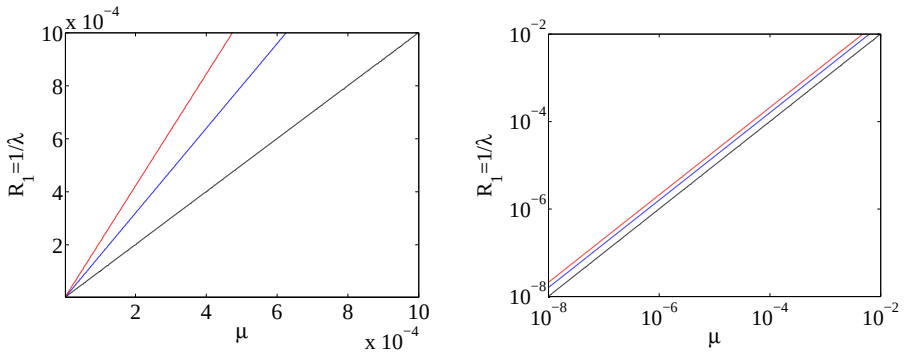

(a) (b)

Figure 4.6: The μ–R_1 parameter space for deterministic nucleation sizes divides into four regions describing whether the recrystallization is homogeneous (equally likely to occur anywhere throughout D), heterogeneous (along grain boundaries), heterogeneous (only at triple junctions), or will not occur (as R_1 increases for constant μ, respectively). On (a) linear and (b) logarithmic axes.

we define the nonnegative normal distribution $\bar{N}$ by

$$f_X(x) = \begin{cases} \frac{1}{\Phi(\mu/\sigma)} \left(\frac{1}{\sqrt{2\pi\sigma^2}} \exp\left(\frac{-(x-\mu)^2}{2\sigma^2} \right) \right), & x \geq 0, \\ 0, & x < 0, \end{cases} \tag{4.18}$$

if $X \sim \bar{N}(\mu, \sigma^2)$, where $\Phi(x)$ is the cumulative distribution function for the standard normal distribution, $N(0,1)$. Suppose $R \sim \bar{N}(\mu, \sigma^2)$. Then we calculate that

$$\mathbb{P}(G \cap T_i) \approx \begin{cases} \frac{1}{\Phi(\mu/\sigma)} \Big\{ (1-2\mu) \left[1 - \Phi\left(\frac{R_1 - \mu}{\sigma} \right) \right] & \\ \qquad - \sigma\sqrt{\frac{2}{\pi}} \exp\left(\frac{-(R_1-\mu)^2}{2\sigma^2} \right) \Big\}, & i = 1, \\ \frac{1}{\Phi(\mu/\sigma)} \Big\{ 2(\mu - \mu^2 - \sigma^2) \left[1 - \Phi\left(\frac{R_2 - \mu}{\sigma} \right) \right] & \\ \qquad + \sigma\sqrt{\frac{2}{\pi}} (1 - R_2 - \mu) \exp\left(\frac{-(R_2-\mu)^2}{2\sigma^2} \right) \Big\}, & i = 2, \\ \frac{1}{\Phi(\mu/\sigma)} \Big\{ 2(\mu^2 + \sigma^2) \left[1 - \Phi\left(\frac{R_3 - \mu}{\sigma} \right) \right] & \\ \qquad + \sigma\sqrt{\frac{2}{\pi}} (R_3 + \mu) \exp\left(\frac{-(R_3-\mu)^2}{2\sigma^2} \right) \Big\}, & i = 3. \end{cases} \tag{4.19}$$

We visualize the effects of parameter choice in the μ–R_1 plane for various values of σ in Figure 4.7. Compare to Figure 4.6(b). Increasing σ increases the probability

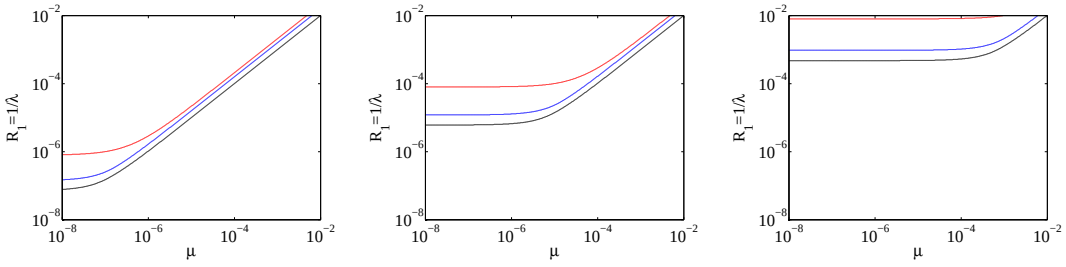

(a) (b) (c)

Figure 4.7: The μ–R_1 parameter space for (a) $\sigma = 10^{-8}$, (b) $\sigma = 10^{-6}$ and (c) $\sigma = 10^{-4}$. Increasing σ increases the likelihood of large nucleations, allowing a greater part of the region to support homogeneous nucleation. The contours bounding other regions move in a similar fashion.

of nucleations with $R > \mu$, allowing homogeneous nucleation to prevail even for $\mu < R_1$. In the regions of parameter space where μ and R_1 are much larger than σ, the behavior is as predicted in the deterministic case.

Figures 4.6 and 4.7 show that there are two very distinct parameter regimes: $\mu \ll \sigma$, and $\mu \gg \sigma$. In the first, $\mu \ll \sigma$, there is a wide range of values R_1 for which heterogeneous nucleation (nuclei survival primarily along grain boundaries) may occur. In contrast, when $\mu \gg \sigma$, nuclei radii are essentially deterministic, and the parameter regime in which heterogeneous nucleation may occur is much more narrow. In this case, there must be a close relationship between R_1 and μ in order for heterogeneous nucleation to occur. As heterogeneous nucleation is frequently observed in practice, it appears reasonable that either $\sigma \gg \mu$ or that there is indeed a close physical relationship between μ and $R_1 = 1/\lambda$.

4.3 Comparison to Previous Work

For the recrystallization model studied here, there are very few theoretical predictions available compared with, e.g., models of normal grain growth. Primary among the known results is the theory of Johnson and Mehl [44], Avrami [6–8],

and Kolmogorov [50] (JMAK) for the kinetics of the recrystallized volume fraction F. The JMAK theory is briefly discussed in Section 4.3.1. In contrast, there is an abundance of numerical simulation studies of recrystallization in the literature. Many of the most recent numerical works focus on incorporating additional features such as texture dependence and physically-based nucleation models. Our focus is different: we stay with the simple model of Srolovitz et al., and explore instead the difference that fully resolved numerics — as opposed to additional physics — makes. Once again, this is in the interest of separating numerical issues (possibly artifacts) from modeling issues. As such, in Section 4.3.2 we compare our numerical results with prior simulations of the Srolovitz model, in particular with the Monte Carlo simulations contained in the original papers [79, 80].

4.3.1 JMAK Theory

A normal interface velocity of the form given by Equation (4.5), in the limit $\lambda \to \infty$, is in keeping with the JMAK theory. This theory is based on the assumption that each nucleated grain grows outward with constant normal velocity, which occurs in our system by neglecting the curvature term, and is approximated by choices of length scale with grains sufficiently large that the bulk energy term dominates the interfacial energy term in Equation (4.5). The JMAK model has associated theoretical results in this limit, predicting the recrystallized volume fraction F to be a sigmoidal function of time, t, in the form

$$F(t) = 1 - \exp(-kt^p), \tag{4.20}$$

where k and p are constant. The parameter p can be predicted given the nucleation technique and the dimensionality of the evolution ([14], page 542).

4.3.2 Monte Carlo Simulations

A variety of numerical techniques have been employed previously in simulations of recrystallization. Chief among them are the Monte Carlo Potts [79, 80] and cellular automata [37] techniques. Both have well-known shortcomings (see, for example, [41], page 422, and [43], page 102). More recently, there are hybrid methods that combine the two [71], as well as a level sets-based implementation [10] of pure bulk energy (recrystallization) dynamics, disregarding angle conditions. The seminal works [79, 80] by Srolovitz et al. both introduced the models we study in this work and carried out Monte Carlo simulations in two dimensions. As an important first step in verifying our algorithms, we demonstrate in this section reasonable agreement between our results and those of [79, 80] in certain parameter regimes. However, we have also observed important differences; we believe these are due to the benefits of our improved numerics and constitute the content of Section 4.4, where they are extensively reported and discussed.

In [79, 80], the authors introduce the parameters H and J, corresponding to scalings for stored (bulk) energy and interfacial energy. They use the ratio H/J in place of our nondimensionalized parameter λ, with the correspondence

$$\lambda = \frac{H}{J}\sqrt{\frac{\langle g \rangle}{\pi}}, \tag{4.21}$$

where $\langle g \rangle$ is the mean number of grid points per grain in the initial (unrecrystallized) microstructure. Every simulation in [79] and [80] uses the same initial microstructure, with $\langle g \rangle \approx 43$ and approximately 930 initial unrecrystallized grains, resulting in $\lambda \approx 3.7H/J$. The nuclei were taken to be 1 site for $H/J = 5$ and 3, and 3 sites for $H/J = 2$, 1.5, 1 and 0.5 on a 200×200 triangular grid. These correspond to nondimensionalized areas of 0.0730 and 0.2191, respectively, with equivalent radii

of 0.1525 and 0.2641 (recall that the mean equivalent radius of an unrecrystallized grain is 1). These parameter choices are plotted in Figure 4.8 on the μ–R_1 parameter space as discussed in Section 4.2.3. Note that for $\lambda = 7.4$ and 5.55 (corresponding to $R_1 = 0.1351$ and $R_1 = 0.1802$, respectively), the parameter choices fall in the homogeneous nucleation range under our analysis. Srolovitz et al. characterize these parameter choices (for them, $H/J = 2$ and 1.5, with 3 site nuclei) as heterogeneous nucleation. The model of Section 4.2.3 suggests that the effects seen in [80] for these parameter choices are an effect of the Monte Carlo simulation technique rather than an outcome determined by the model of Equation (1.6).

We will now focus on the simulations of site-saturated nucleation performed in [79,80]. Our simulations were performed for 200, 100, 50, 20, 10 and 5 nuclei at $\lambda = 18.5$ and $\lambda = 11.1$, and for 2000, 1000, 500, and 200 nuclei at $\lambda = 7.4$, 5.55, 3.7, and 1.85, agreeing with the simulations of [79,80]. Figure 4.9 examines the microstructure for 200 nuclei, with radius $\mu = 0.2641$. Figure 4.9(a) shows part of the microstructure at $t = 0$, immediately after 200 nuclei are added to the domain. Figures 4.9(b) and (c) show the microstructure for $\lambda = 7.4$ and $\lambda = 5.55$ at $t = 0.557$. In these simulations, it is clear that *all* nuclei are growing, agreeing with the prediction of homogeneous growth shown in Figure 4.8. For $\lambda = 3.7$, the chosen nucleation size is very near the border of homogeneous growth and grain boundary-dominated growth. It can be seen in Figure 4.9(d) that for this parameter choice, grains nucleated in grain interiors remain approximately stationary, while grains nucleated on grain boundaries and at triple junctions grow. Note that the theory of Section 4.2.3 does not account for the rate at which grains grow or shrink, or impingement between nucleating grains. In these simulations, impingement will occur before some of the nuclei in grain interiors disappear. In Figure 4.9(e), grains which nucleate in grain interiors

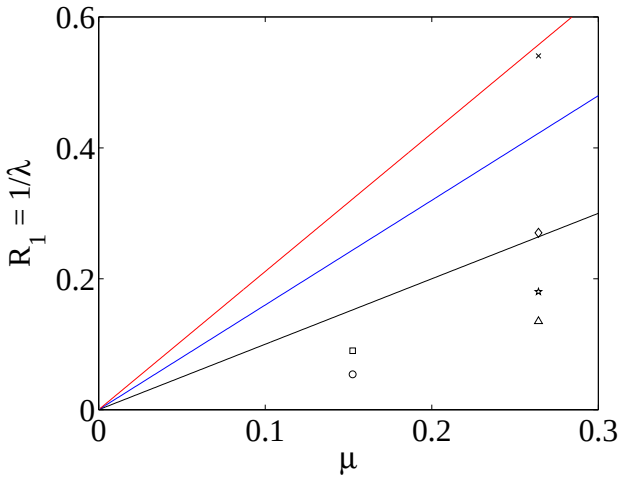

Figure 4.8: The deterministic μ–R_1 parameter space with the simulations of [79, 80] marked. $\lambda =$ 18.5, 11.1, 7.4, 5.55, 3.7 and 1.85 correspond to circle, square, triangle, star, diamond and x markers, respectively. Note that the simulations with $\lambda = 7.4$ and 5.55 correspond to homogeneous nucleation for this model, not heterogeneous nucleation as is found by the Monte Carlo simulations.

disappear quickly, with all completely gone by $t = 0.1115$. Grains which nucleated along grain boundaries persist longer but again have all vanished by $t = 0.2229$. At this time only recrystallizing grains which nucleated at triple junctions remain, agreeing with the prediction shown in Figure 4.8 for $\lambda = 1.85$.

Figure 4.10 demonstrates the time evolution of the recrystallized area fraction F for simulations of site-saturated recrystallization with varying values of $\lambda \in [1.85, 18.5]$ and varying numbers of recrystallization nuclei (from 5 to 2000), corresponding precisely to the parameter choices of Figures 6 and 7 in [79] and those of Figures 8 and 9 in [80]. The essential features of our plots match the corresponding ones in [79, 80]. Figure 4.10(b) visualizes the Avrami exponent p of Equation (4.20). The JMAK prediction can be rearranged as $\log(-\log(1-F)) = p \log t + \log k$, suggesting that these plots should have slope p on logarithmic axes, where p is predicted to be 2 for two-dimensional site-saturated nucleation ([14], page 542). Triangles with slope 2 are inset on the Avrami plots and agree well with the trends of the

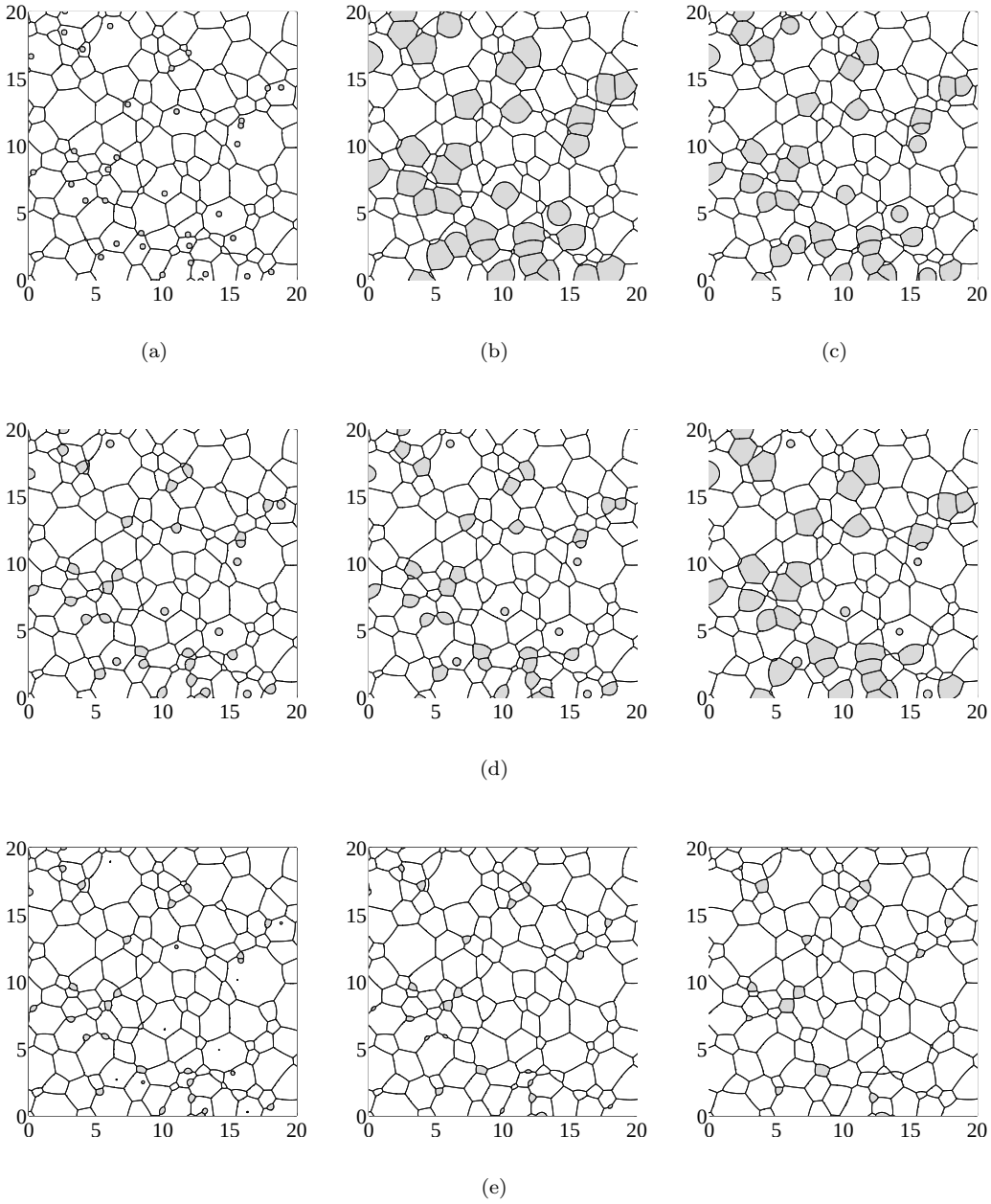

Figure 4.9: Snapshots of microstructure for site-saturated nucleation, with 200 nuclei of radii 0.2641 and varying λ. (a) Nuclei immediately after nucleation. (b) $\lambda = 7.4$ at $t = 0.0557$. (c) $\lambda = 5.55$ at $t = 0.0557$. In both (b) and (c), all nuclei survive and grow: homogeneous nucleation. (d) $\lambda = 3.7$ at $t = 0.0557$, 0.1115, and 0.2229, respectively. Nuclei crossing grain boundaries and triple junctions clearly grow, while nuclei in grain interiors appear to remain approximately stationary. (e) $\lambda = 1.85$ at the same times as (d). Nuclei away from triple junctions all disappear quickly.

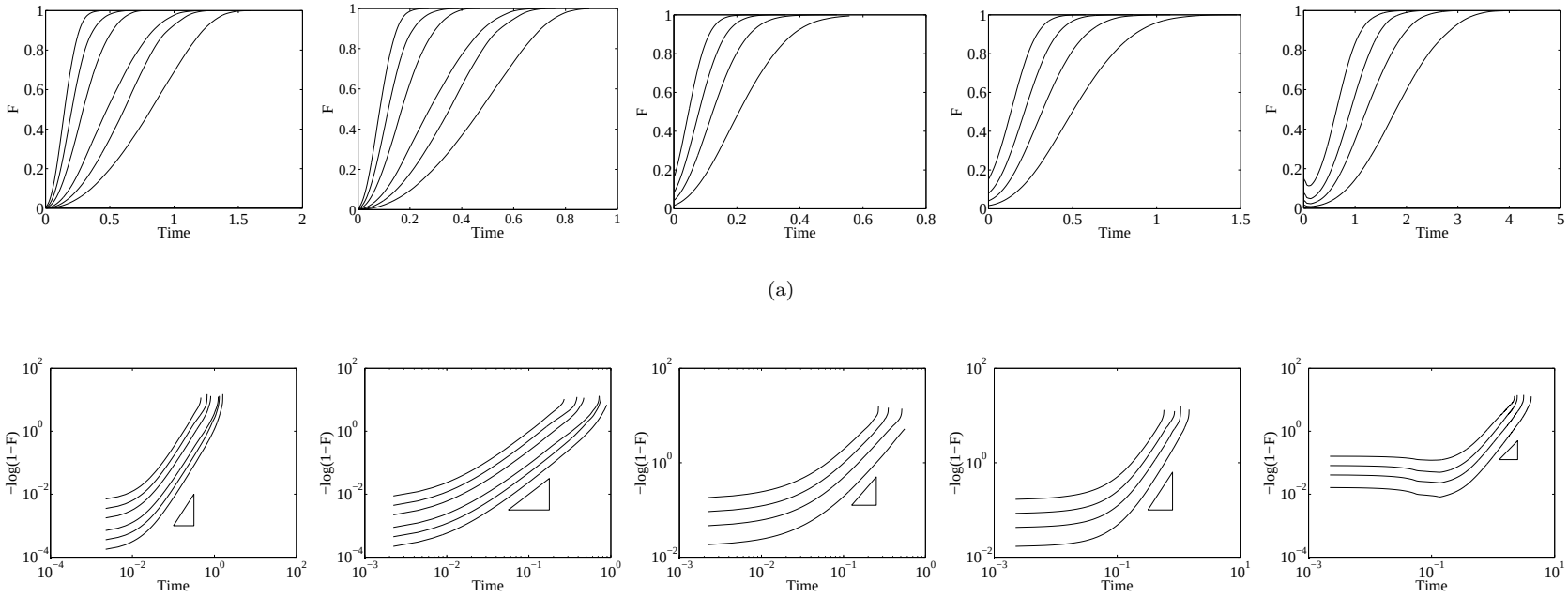

(a)

(b)

Figure 4.10: (a) The recrystallized area fraction F for $\lambda = 18.5$, 11.1, 7.4, 5.55, 3.7 and 1.85, respectively. The curves correspond to 200, 100, 50, 20, 10, and 5 nuclei (from left to right) in the first two plots, and to 2000, 1000, 500, and 200 nuclei in the last three. Corresponds to Figure 6 of [79] and Figure 8 of [80]. (b) The Avrami plots for the same experiments, corresponding to Figure 7 of [79] and Figure 9 of [80]. The slope of two is predicted for two-dimensional site-saturated nucleation.

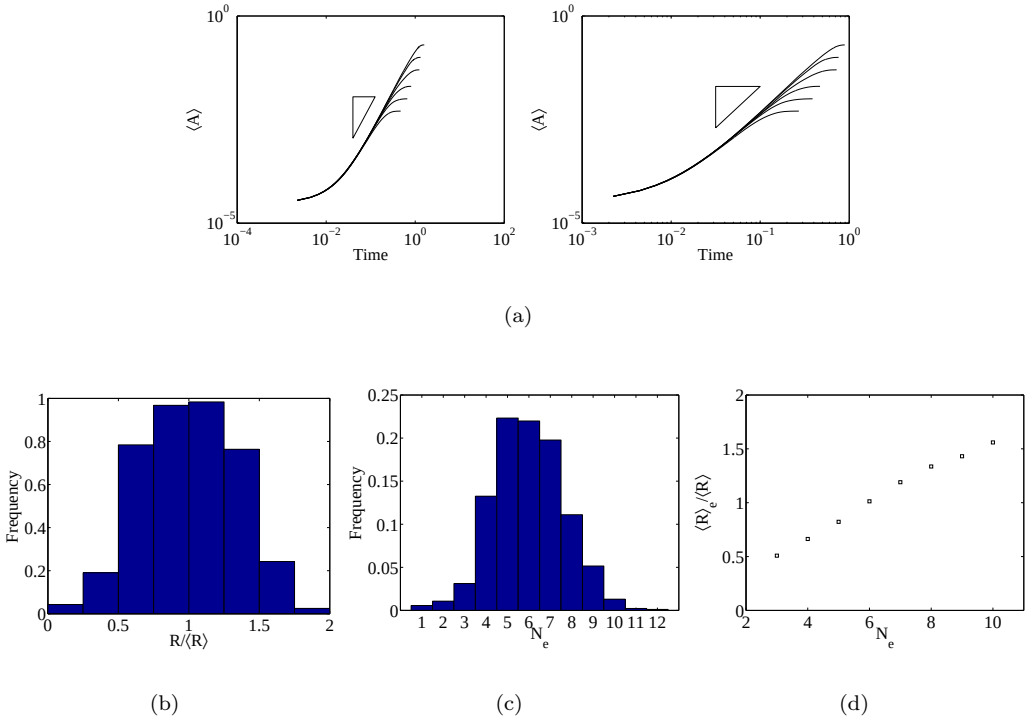

Figure 4.11: (a) The evolution of the average recrystallized grain area $\langle A \rangle$ through time for $\lambda = 18.5$ and 11.1, respectively. The slope of two is predicted by the growth rate of a circle under pure bulk energy motion. Corresponds to Figure 8 of [79]. (b) The grain size distribution function for recrystallized grains for $\lambda = 3.7$ and 2000 site-saturated nuclei at $F = 0.9$. (c) The distribution of number of edges per grain for the same conditions as (b). (d) The mean normalized size of N_e sided grains for the same conditions as (b). (b), (c) and (d) correspond to Figures 10, 11, and 12 of [80], respectively.

plots at intermediate times. Note that the JMAK prediction is approximate for this model, neglecting the influence of curvature, which is strongest on small recrystallizing grains, present early in the evolution.

The evolution of the mean recrystallized grain area for simulations with $\lambda = 18.5$ and 11.1 is shown in Figure 4.11(a). As expected (see, for example, [79]), $\langle A \rangle$ increases with t^2 at intermediate times, when the effect of curvature on recrystallized grain size is small but the recrystallized grains do not impinge on each other frequently. At later times in the evolution, the mean growth rate of recrystallized grains slows due to impingement. This plot agrees well with Figure 8 of [79] up to

scaling factors in time and total area.

Figure 4.11(b) gives the grain size distribution function for recrystallized grains in the simulation with $\lambda = 3.7$ and 2000 site-saturated nuclei at the time when an area fraction of $F = 0.9$ is reached, while Figure 4.11(c) gives the distribution of N_e sided recrystallizing grains, and Figure 4.11(d) gives the mean normalized size of N_e sided grains for these same conditions. The plots should be compared to Figures 10, 11, and 12 of [80]: the parameters of our and their simulations matched exactly. Some differences are striking. For example, we find the peak of the topological (number of edges) distribution to fall at $N_e = 5$ (Figure 4.11(c)), while Figure 11 of [80] shows the peak of this distribution to fall at $N_e = 4$. Our results find a much smaller proportion of four-sided grains than any of five-, six- or seven-sided grains.

Figure 4.11(d) displays an approximately linear relationship between the topological class (number of edges) of a grain and the mean normalized grain radius for grains of that topological class, in disagreement with the simulation results of [80], which show some nonlinearities for small and large N_e (see Figure 12 of [80]). Also, the peak of the grain size distribution is to the right of 1 in the present simulations (Figure 4.11(b)), while it is to the left of 1 in the Monte Carlo simulations. However, the sample size is small and the distributions are not well resolved, so one must be cautious in making conclusions about the cause of these observations. The major observation made in [80] about Figure 10 of that work holds in Figure 4.11(b): the maximum grain size is not more than twice the mean among recrystallizing grains. In contrast, this ratio is seen in grain growth to be between 2.5 and 3.

Following [79, 80], we also perform simulations under continuous nucleation conditions. At each time step, we nucleate grains at locations uniformly chosen in the microstructure, but remove nuclei placed at already-recrystallized locations. Thus

the effective nucleation rate declines as recrystallization proceeds due to the decrease in area available for nucleation. It is difficult to relate our nondimensionalized time to the Monte Carlo steps of [79,80], as it is well known that some type of calibration must be performed to link Monte Carlo time to physical time (see, for instance, the discussion in [43], page 102). Based on the simulation times reported in this work and in [79,80] for site-saturated nucleation, we make the approximation that 1 nucleation per Monte Carlo step is roughly equivalent to 112.1 nucleations per unit time in our simulations.

Figure 4.12 displays the evolution of the recrystallized area fraction F in our simulations of continuous nucleation for choices of the parameter λ and the nucleation rate dn/dt, that correspond to those of Figures 11 and 12 of [79] and Figures 18 and 19 of [80]. In each case, it appears that the predicted Avrami exponent of 3 is approximately attained in the later stages of the simulation. Note that particularly for few nucleations per unit time and small λ, the Avrami plots are quite jagged early in the evolution. This is an effect of the small number of recrystallized nuclei present at this time in the simulation and the importance of the curvature term in delaying or preventing the growth of some nuclei (particularly for $\lambda = 3.7$ or 1.85, which correspond to the heterogeneous nucleation regime).

In [79,80], the authors report that the recrystallized grain size for $F = 0.95$ varies with nucleation rate approximately as $(dn/dt)^{-2/3}$, in agreement with theoretical predictions of [31]. If we compare Figure 14 of [79] and Figure 15 of [80] to our Figure 4.13, then it is apparent that our simulations show good agreement with this prediction. Note that the last two data points for $\lambda = 18.5$ and 11.1 have areas averaged for less than 50 surviving recrystallized grains — such a small number of surviving grains is insufficient to expect close fit to statistical predictions.

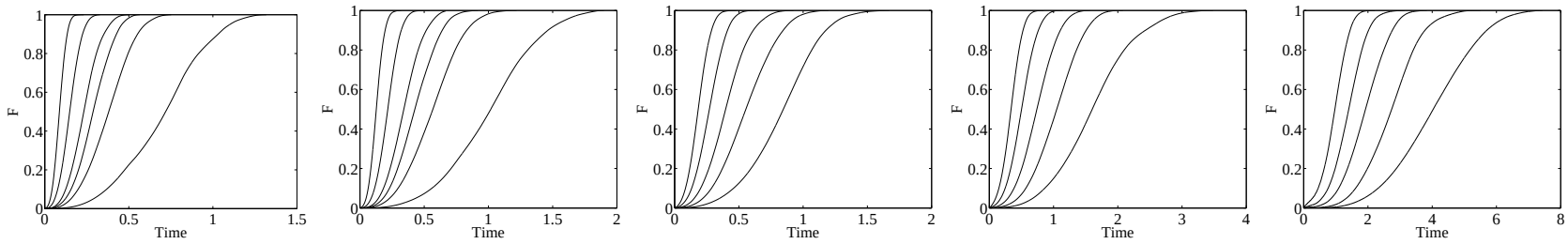

(a)

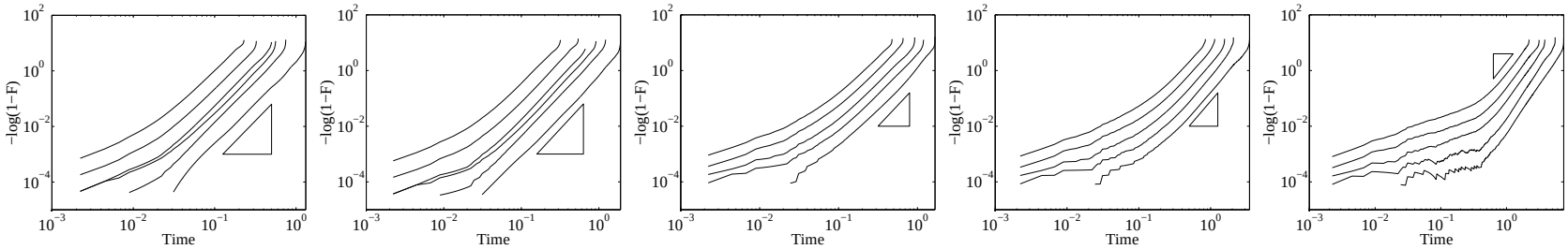

(b)

Figure 4.12: (a) The recrystallized area fraction F for $\lambda = 18.5$, 11.1, 7.4, 5.55, 3.7 and 1.85, respectively. The curves correspond to 5607, 1121, 224, 112, 56, and 22 nucleations per unit time (from left to right) in the first two plots, and to 3364, 1121, 336, 112, and 37 nucleations per unit time in the last three. Corresponds to Figure 11 of [79] and Figure 18 of [80]. (b) The Avrami plots for the same experiments, corresponding to Figure 12 of [79] and Figure 19 of [80]. The slope of three is predicted for two-dimensional continuous nucleation.

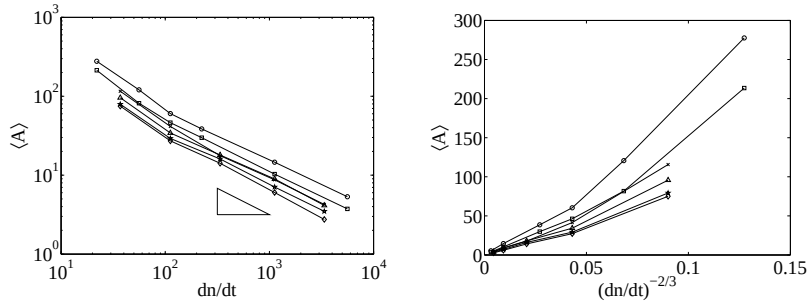

(a) (b)

Figure 4.13: Comparison of the mean recrystallized grain size $\langle A \rangle$ at $F = 0.95$ to the nucleation rate dn/dt. $\lambda = 18.5$, 11.1, 7.4, 5.55, 3.7 and 1.85 correspond to circle, square, triangle, star, diamond and x markers, respectively.

4.4 Benefits of Diffusion-Generated Motion

As already mentioned, the work of Srolovitz et al. in [79, 80] and of Hesselbarth and Göbel in [37] represent some of the major contributions to the field. There is a long list of more recent works that add further physical details (such as texture) to the models and extend the simulations to three dimensions (for example, [27, 67]), but the basic Monte Carlo techniques remain largely the same. It is important to be aware of some basic limitations of the Monte Carlo technique applied in [79, 80]:

- For small λ, [79, 80] cannot produce the appropriate stationary shapes seen in Figure 4.4, with aspect ratio independent of λ.

- For large λ, grain boundaries become rough, though the PDE description of the model does not predict this behavior.

- Monte Carlo techniques are most appropriate for simulating atomistic-scale interactions. Recrystallization is often studied on the micrometer scale and so would require prohibitively expensive computation for each grid point to resolve the atomistic scale.

- The lattice definition (e.g. square or triangular) and neighborhood definition affect the results of Monte Carlo simulations, as noted in [5].

In Figures 1 and 2 of [80], the authors demonstrate that nuclei grow along grain boundaries but not out into the bulk of unrecrystallized grains for small values of the parameter H/J in their Monte Carlo simulations. However, we have shown in Section 4.2.2 that the critical grain shapes have aspect ratios independent of λ for this model: the shapes described in [80] are artifacts of the algorithm, not the model. In particular, we believe that they are a consequence of performing zero temperature simulations. For sufficiently small H/J in Monte Carlo simulations, it is *never* energetically favourable to change a single site from unrecrystallized to recrystallized if less than half the neighboring sites are already recrystallized. For certain parameter choices, it will be energetically favourable for growth to occur only along the grain boundary but not out into the unrecrystallized grain bulk. This observation is independent of the grid resolution and the overall size of the recrystallized grain which is attempting to grow. In contrast, Figure 4.3 shows that, under the diffusion-generated motion algorithm, any initial nucleus which is sufficiently large for the choice of λ will grow and evolve towards the critical shape described by Equation (4.6).

In [79], the authors forthrightly admit that rough boundaries arise from the growth of a circular grain for large H/J. Figure 4.3 demonstrates that no such difficulty arises for diffusion generated motion with precisely corresponding parameter choices. Though the initial shape is very irregular, it quickly relaxes to a shape with smooth boundary and maintains smooth boundaries away from triple junctions as $\lambda/\kappa \to \infty$. These observations suggest that the Monte Carlo model has limitations for *both* large and small values of H/J. However, diffusion generated motion successfully obtains

the correct behaviors in both situations.

The two-dimensional simulations of [79, 80] are performed on 200×200 grids. In three dimensions, [67] work on a $30 \times 30 \times 30$ grid, and [27] work on a grid of $100 \times 100 \times 100$ with 822 initial grains. In Sections 4.4.1 and 4.4.2, we perform much larger simulations in both two and three dimensions while at the same time having full benefit of subgrid resolution. These simulations take as initial condition a number of unrecrystallized grains generated by normal grain growth starting from Voronoi initial data. The parameters for our two-dimensional simulations are chosen to agree with physically relevant length scales and surface tensions and bulk energies. In three dimensions, computational constraints prevent us from obtaining the proper scaling between unrecrystallized grains and recrystallizing nuclei (while having several unrecrystallized grains fit into the computational domain). We nucleate grains with mean radius $\langle r_n \rangle = 0.0378$, so that nuclei are approximately 5×10^{-5} the volume of unrecrystallized grains initially. The vast majority of the nuclei disappear quickly. We are able to see the influence of the angle conditions and surface tension on the microstructure (which always play a role at junctions and at small scales even when vanishingly small, as discussed in previous sections), resulting in grains which are clearly faceted as seen in experiments. In contrast, other numerical algorithms fail to show this clear faceting. The pure bulk energy phase field simulations of Bernacki et al. fail to respect the angle conditions (for example, see Figure 8 of [10]) and recrystallizing grains tend to be circular until collision with other recrystallizing grains. Monte Carlo simulations necessarily generate grains with rough boundaries, as discussed in [79], which also produces less clearly faceted grains.

As the discretization of a continuum (PDE) model, we believe that diffusion generation motion is more appropriate for simulating evolutions at the micrometre scale

than the inherently atomistic Monte Carlo method. As such, our simulations can more cleanly reproduce theoretical predictions of the PDE model (4.5) used in this work. For example, the diffusion generated motion simulations correctly find the appropriate nucleation regimes for parameters in μ–R_1 space, while the Monte Carlo simulations fail to do so (see Figure 4.8). Furthermore, the diffusion generated motion algorithm performs correctly on a simple uniform grid and requires no definition of the neighborhood surrounding a grid point.

4.4.1 Large Scale Two-Dimensional Simulations

We present three large-scale simulations of recrystallization in two dimensions. Each simulation is initialized with sixteen unrecrystallized grains on a domain that corresponds to $\Omega = [0, 4\sqrt{\pi}]^2$ in our nondimensionalized setting. In each simulation, tens of thousands to millions of recrystallized grains are nucleated, with initial sizes thousands of times smaller than the existing grains. The first two simulations are performed under site-saturated nucleation conditions, designed to demonstrate the ability of our algorithm to efficiently simulate recrystallization with physically-relevant parameter choices and to allow for comparison to the analysis of Section 4.2.3. The third simulation is performed under the conditions of continuous nucleation. Here, only 26 of over *four million* nuclei survive to the end of recrystallization, as the mean nucleus size is much smaller than the critical nuclei sizes described by Equation (4.9). The variation seen in grain sizes at the completion of recrystallization is primarily due to the differing nucleation times of the surviving grains. In contrast, the variation in grain sizes seen in the simulation with site-saturated nucleation is due primarily to differences in time of impingement along pre-existing grain boundaries.

Site-Saturated Nucleation I

In the first simulation we make physically reasonable choices for the sizes of recrystallizing nuclei and unrecystallized grains. We choose $\lambda = 577.73$, and nucleate 42,095 grains. The radii of nuclei are normally distributed with mean $\langle r_n \rangle = 3.55 \times 10^{-4}$ and standard deviation $\sigma_n = 7.09 \times 10^{-5}$. This choice of parameters is well within the heterogeneous nucleation regime, as $R_1 = 1.73 \times 10^{-3}$. Using the values $\gamma = 0.5\, J/m^2$ and $\rho = 10\, MPa$ discussed in Section 4.1, $\langle r_0 \rangle = 28.9\, \mu m$, and the mean recrystallizing nucleus size is $\langle r_n \rangle = 0.01\, \mu m$: recrystallizing nuclei are a factor of 10^4 smaller than unrecrystallized grains. This wide range of length scales is necessary for curvature effects to be significant for recrystallizing nuclei while maintaining physical sizes for unrecrystallized grains. With these parameter choices, by the time a recrystallized nucleus reaches a size comparable to that of a pre-existing grain, the effect of surface tension will be negligible away from junctions (where angle conditions will still be maintained): along facets, the bulk energy term will dominate the dynamics.

We evolve until the nuclei completely cover Ω at $t = 1.73 \times 10^{-3}$. At that time, there are 245 surviving recrystallized grains. The vast majority of nucleated grains disappear almost immediately in the evolution. Figure 4.14 displays the agreement of this simulation with JMAK predictions. The recrystallized area fraction F evolves sigmoidally in time and the Avrami plot of t against $-\log(1 - F(t))$ appears to be approximately linear on logarithmic axes. The slope of the line in the Avrami plot is approximately 2, agreeing with the prediction in [14] (page 542) for site-saturated homogeneous nucleation. There is a visible decrease in $-\log(1 - F)$ at early times. This is due to the large number of nuclei that are nucleated but disappear almost immediately.

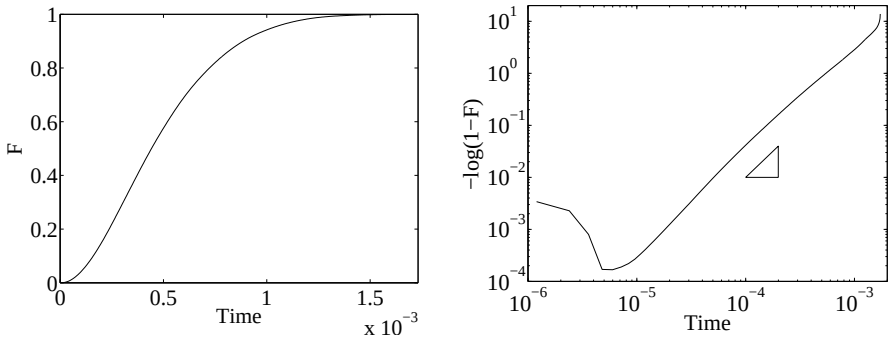

(a) (b)

Figure 4.14: Recrystallization kinetics for two dimensional site-saturated nucleation with physically relevant parameters. (a) The fraction of recrystallized area F evolves sigmoidally in time, as expected. (b) The Avrami plot is approximately linear throughout the bulk of the evolution and demonstrates the expected slope of 2 for site-saturated homogeneous nucleation in two dimensions. The initial decrease in the Avrami plot is due to the fast disappearance of many nucleated grains that do not survive.

For $\lambda = 577.73$, a circular recrystallizing grain contained within a single pre-existing grain must have its radius r be at least $0.05\,\mu m$ in order to remain stationary. Smaller grains that are not touching each other or crossing grain boundaries will shrink and disappear. Recrystallizing nuclei crossing grain boundaries or touching other recrystallizing nuclei benefit both from the additional energy removed from the system (due to elimination of part of the original boundaries) and from the natural boundary conditions which take effect immediately, quickly forming the characteristic shape described in Section 4.2.1. This preference is displayed clearly in Figure 4.15(a), where at time $t = 1.07 \times 10^{-4}$, the surviving nuclei are primarily located along grain boundaries. Note that by this time the surviving recrystallized grains (which appear quite tiny) have already grown considerably from their initial embryonic state — the embryos are too small to display on this Figure 4.15(a). At this time, we also observe that large numbers of recrystallized grains that survive along existing grain boundaries contact their neighbors as they grow, and as a result of

this crowding recrystallized grains tend to form elongated shapes which eventually penetrate deep into the bulk of unrecrystallized grains (see Figure 4.15(b), at time $t = 4.90 \times 10^{-4}$). When the evolution is complete, at $t = 1.73 \times 10^{-3}$, there are many elongated grains because the majority of surviving recrystallized grains nucleated at grain boundaries, and there are many more surviving recrystallized grains (245) than there were unrecrystallized grains originally (16). The Herring angle condition is maintained for the recrystallized grain pattern. This is difficult to see when the entire simulation domain Ω is viewed (Figure 4.15(c), top), as the surface tension term is negligible in comparison to the bulk energy term at the $O(1)$ scale with our choice of parameters. On smaller scales (same figure, zoomed in at bottom), the mere presence of the tiny surface tension introduces curvature into grain boundaries right near the junctions to maintain the Herring angle condition.

Site-Saturated Nucleation II

In this simulation, we choose parameters to predict even more severe heterogeneity than in the simulation of Section 4.4.1. We set $\lambda = 288.87$, and nucleate 162,070 grains. The radii of nuclei are normally distributed with mean $\langle r_n \rangle = 2.13 \times 10^{-3}$ and standard deviation $\sigma_n = 2.13 \times 10^{-4}$. Here, using the values $\gamma = 0.5\, J/m^2$ and $\rho = 10\, MPa$ determines that $\langle r_0 \rangle = 14.4\, \mu m$, and the mean recrystallizing nucleus size is $\langle r_n \rangle = 0.03\, \mu m$. These parameters are chosen to support successful nucleation along grain boundaries and at triple junctions while discouraging the survival of nuclei in pre-existing grain interiors. The number of grains expected to survive is higher than in the previous simulation. We evolve until the nuclei cover Ω at $t = 5.12 \times 10^{-3}$. At this time, there are 542 surviving recrystallized grains.

The simulation described in Section 4.4.1 approached the limit of the grid resolution. The mean nuclei radius was just 1.23 grid cells. This simulation further

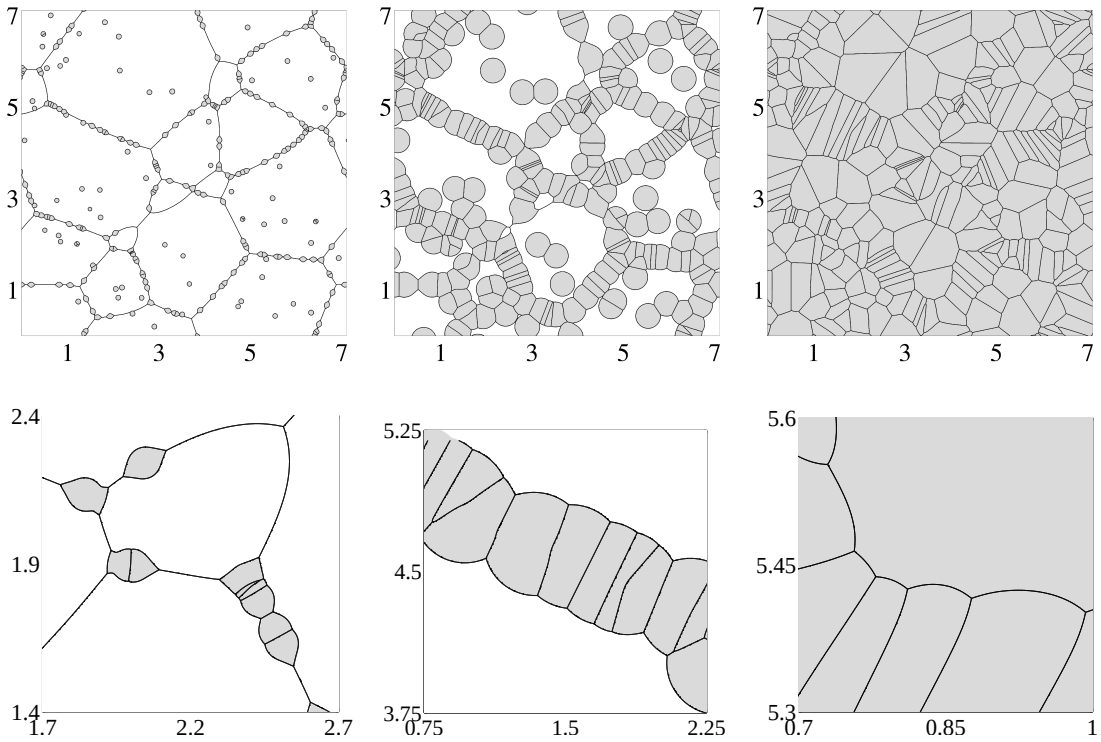

(a) (b) (c)

Figure 4.15: Microstructure of two-dimensional site-saturated nucleation simulation I, with physically relevant parameters. (a) At time $t = 1.07 \times 10^{-4}$, with $F = 0.05$. Surviving nuclei are heavily concentrated along grain boundaries. The originally-circular nuclei are clearly taking the characteristic shape described in Section 4.2.1. (b) At time $t = 4.90 \times 10^{-4}$, with $F = 0.56$. The concentration of surviving nuclei along the original grain boundaries leads to elongated recrystallizing grains as recrystallization continues. (c) Recrystallization is complete at time $t = 1.73 \times 10^{-3}$. Many elongated recrystallized grains are present because most surviving nuclei originated along grain boundaries. Close inspection reveals that recrystallized grain boundaries meet at 120° angles though this cannot be easily seen when viewing the entire simulation domain. At this level, the evolution is dominated by the bulk energy motion. Full simulation domain shown at top, with zoom-in below.

refines the grid, takes larger recrystallizing nuclei to improve resolution in the initial stages of the simulation, and decreases the value of λ. These changes allow for comparison with the theoretical predictions of Section 4.2.3, which depend on accurate computations for grains near the critical sizes. We discretize the initial condition on a 8192×8192 grid. After the surviving recrystallized grains grow to sufficient size, we coarsen the grid to 4096×4096 and take larger time steps. No impact on the kinetics of recrystallization were detected.

The analysis of Section 4.2.3 is rough, yet Equations (4.15) and (4.19) make excellent predictions for this simulation. Indeed, these equations indicate that nuclei should only survive along grain boundaries or at triple junctions, with 99.5% of surviving nuclei originally nucleating along grain boundaries and the remainder at triple junctions. Visual inspection of Figure 4.16 indicates that a few nuclei survive in the grain interior, but that the vast majority of survivors are indeed along grain boundaries and triple junctions. The analysis predicts that 0.02% of the nuclei should survive, agreeing reasonably well with the simulated survival rate of 0.033% at the end of recrystallization.

Figure 4.16 shows the microstructure of the evolution at various times throughout the simulation. As noted, the majority of grains survive along grain boundaries and at triple junctions. In Figure 4.16(a), at time $t = 7.79 \times 10^{-5}$, $F = 9.9 \times 10^{-3}$. The zoom-in indicates that the growing grains tend towards the characteristic shape shown in Figure 4.3. Figures 4.16(b), (c) and (d) correspond to $t = 2.40 \times 10^{-4}$ and $F = 0.086$, $t = 5.51 \times 10^{-4}$ and $F = 0.26$, and $t = 5.13 \times 10^{-3}$ and $F = 1$, respectively. As in the prior simulation, it can be seen that the Herring angle condition is maintained, though these boundary conditions are difficult to visualize on the scale of the full simulation (Figure 4.16(d)).

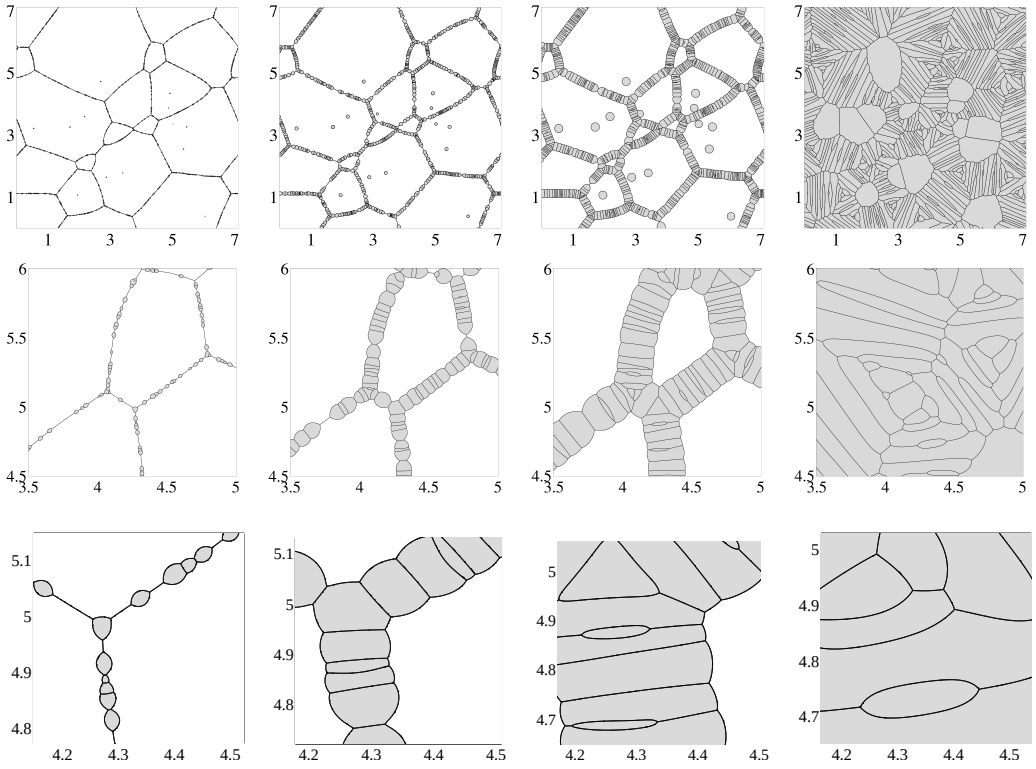

(a) (b) (c) (d)

Figure 4.16: Microstructure of two-dimensional site-saturated nucleation simulation II, with higher surviving grain density along pre-existing grain boundaries. (a) At time $t = 7.79 \times 10^{-5}$, with $F = 9.9 \times 10^{-3}$. (b) At time $t = 2.40 \times 10^{-4}$, with $F = 0.086$. Nuclei are beginning to impinge along grain boundaries, while some unimpinged grains can still grow in all directions. (c) At time $t = 5.51 \times 10^{-4}$, $F = 0.26$. All nuclei except those in grain interiors have impinged along the pre-existing grain boundaries and can grow along only one dimension. (d) Recrystallization is complete at $t = 5.13 \times 10^{-3}$. Many elongated recrystallized grains are present because most surviving nuclei originated along grain boundaries. Full simulation domain shown at top, with successive magnification below.

As recrystallization proceeds, grains begin to impinge upon each other along grain boundaries and grow primarily normal to the boundaries between pre-existing grains. Thus the recrystallized grains tend to be quite elongated. Figure 4.17(a) shows the distribution of a generalized measure of eccentricity computed among grains surviving at the completion of recrystallization. The generalized eccentricity is computed as the ratio of radius computed from perimeter, $R_P = (\text{Perimeter})/2\pi$, to radius computed from area, $R_A = \sqrt{(\text{Area})/\pi}$. Many of the grains remaining at the end of recrystallization have high eccentricity, greater than that of a rectangle with side length ratio of $10 : 1$. The most eccentric grains had eccentricity comparable to a rectangle with side length ratio of $20 : 1$. The mean grain eccentricity is 1.58, with standard deviation 0.41. In contrast, grain eccentricities were calculated for fifty smaller simulations of normal grain growth, each starting with approximately $10,000$ grains initialized as Voronoi data and concluding with approximately $1,000$ grains. For these simulations of normal grain growth, the final mean grain eccentricity is 1.06, with standard deviation 0.03.

Figure 4.17 compares the evolution of the recrystallized area fraction (F) with JMAK predictions. The recrystallized area fraction F is expected to be a sigmoidal function of time. In this simulation, the sigmoidal tails are asymmetric (Figure 4.17(b)). This effect is due to the multiple growth regimes clearly seen in the Avrami plot (Figure 4.17(c)). The prediction for site-saturated homogeneous nucleation is a slope of 2 [14] (page 542). This slope is seen early in the evolution, before nucleated grains begin to impinge upon each other in significant numbers. Later in the evolution, nucleated grains show significant impingement along the pre-existing grain boundaries, but are still free to grow along the normal direction to the grain boundaries. In Figure 4.17(c), the left triangle has a slope of 2, while the right triangle is

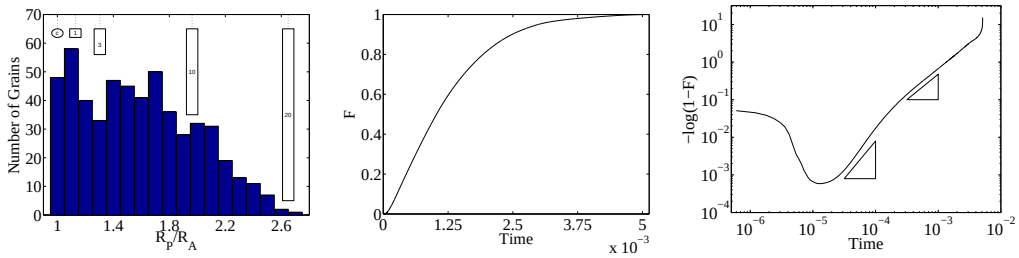

(a) (b) (c)

Figure 4.17: (a) The ratio of $R_P = (\text{Perimeter})/2\pi$ to $R_A = \sqrt{(\text{Area})/\pi}$ reveals that many grains are very elongated. For comparison, the value of R_P/R_A is shown for a circle and for rectangles with side length ratios of 1, 3, 10, and 20. (b) Recrystallization kinetics for two dimensional site-saturated nucleation with physically relevant parameters. The fraction of recrystallized area F evolves approximately sigmoidally in time. Two growth regimes are seen in the Avrami plot (c). The expected slope of 2 predicted for site-saturated homogeneous nucleation prevails initially. At later times, nuclei impinge along pre-existing grain boundaries but are free to grow in the direction normal to these boundaries. The data in this region is numerically fit to a slope of 1.355.

fit locally to the data with a slope of 1.355.

After recrystallization concludes, the simulation reduces to normal grain growth (since the bulk energy terms in (4.5) vanish). Because surface tension is negligible away from triple junctions compared to the now exhausted bulk energy driving forces once the grains reach this scale, the evolution of the system becomes extremely slow and therefore the time step has to be increased in the simulation. We continue to coarsen the grid as the grain growth proceeds, allowing for computational efficiency with larger time steps. In doing so, we ensure that the mean grain width along the minor axis of the elongated grains remains well-resolved throughout the coarsening process. The final grid size is 1024×1024. Recrystallization concludes at time $t = 5.13 \times 10^{-3}$, with 542 surviving nuclei. Grain growth is performed until just 52 grains remain, at time $t = 3.50 \times 10^{-1}$. A computation over such a long time period would be computationally infeasible without the grid and time step coarsening made possible by the large size of the surviving grains in the system, as well as the

t	# Grains	$R(t)_{\max}$	$\langle R(t)\rangle$	$\psi(t)$	$\langle R_P/R_A\rangle$
5.13×10^{-3}	542	9.89×10^{-2}	2.10×10^{-2}	4.70	1.582
8.76×10^{-2}	161	1.40×10^{-1}	3.78×10^{-2}	3.72	1.196
1.76×10^{-1}	92	1.62×10^{-1}	4.97×10^{-2}	3.25	1.148
2.62×10^{-1}	66	1.75×10^{-1}	5.95×10^{-2}	2.93	1.138
3.50×10^{-1}	52	1.87×10^{-1}	6.68×10^{-2}	2.80	1.132

Table 4.2: Data for maximum grain size, mean grain size, and their ratio, $\psi(t)$ demonstrates that while $R(t)_{\max}$ increases, $\psi(t)$ decreases. $\dot{\psi}(t) > 0$ is a condition for abnormal grain growth as defined by Detert [16]. The mean grain eccentricity $\langle R_P/R_A\rangle$ is also seen to decrease.

unconditional numerical stability of our algorithms.

Figure 4.18 shows the evolution of the same microstructure from the simulation of Figure 4.16 beyond the fully recrystallized configuration shown in part (d) of that figure. More precisely, Figure 19(a), (b), and (c) show the solution, which evolves effectively via normal grain growth starting from Figure 4.16(d), at approximately quarter, half, and final times of the full computation. During this time, the elongated grains disappear or become more equiaxed. The few very large grains evident in the microstructure at the end of primary recrystallization continue to grow. Detert [16] defines *abnormal grain growth* as being characterized by an increase in maximum grain size that is much faster than the increase in mean grain size. Specifically, the function

$$\psi(t) = \frac{R(t)_{\max}}{\langle R(t)\rangle} \tag{4.22}$$

must be increasing. In this evolution, $R(t)_{\max}$ is increasing, but $\psi(t)$ is decreasing. Values at various stages in the evolution are shown in Table 4.2. This simulation result agrees with the conclusion of simulations in [78], and analysis in [84], in which the authors suggest that abnormal grain growth *cannot* occur under pure curvature motion, regardless of the initial grain size distribution. Instead, abnormal grain growth must result from additional factors such as the presence of second-phase particles, texture, or other surface effects ([41], page 316).

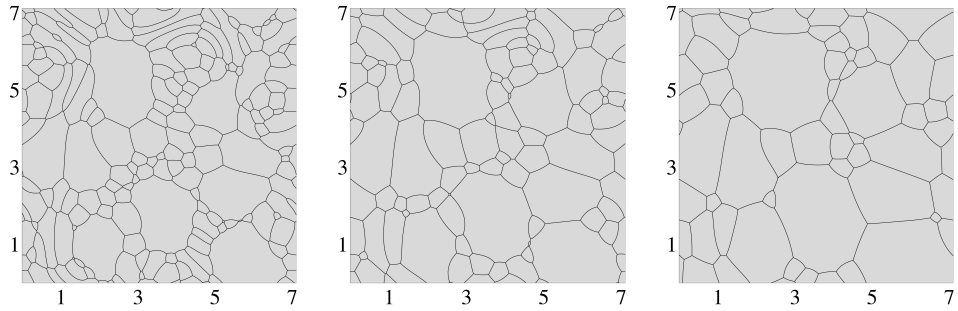

Figure 4.18: The evolution of the microstructure during grain growth following primary recrystallization at (a) $t = 8.76 \times 10^{-2}$, (b) $t = 1.76 \times 10^{-1}$, and (c) $t = 3.50 \times 10^{-1}$. Elongated grains tend to become more equiaxed. The unusually large grains continue to grow, but the mean grain size grows faster. This evolution does not correspond to abnormal grain growth.

Table 4.2 also displays the evolution of the mean grain eccentricity, $\langle R_P/R_A \rangle$. This value is also seen to decrease as normal grain growth proceeds. At the conclusion of the grain growth simulation, there are too few grains present to make statistically significant claims about the convergence of the grain size distribution to the self-similar distribution expected for normal grain growth (and which has been numerically observed by many authors in dedicated simulations). However, the decay of both the maximum relative grain size $\psi(t)$ and the mean grain eccentricity towards values seen for normal grain growth (calculated as 2.212 and 1.06, respectively, for 50 simulations of normal grain growth from Voronoi initial data of approximately 10,000 grains until approximately 1,000 grains remain, via diffusion generated motion) suggests that this evolution is not significantly different that what is observed in typical simulations of normal grain growth, despite the highly unusual initial condition of extremely directionally-correlated and elongated grains.

Continuous Nucleation

The parameters in our continuous nucleation simulation have been chosen so that the vast majority of nuclei disappear quickly. Specifically, our parameters were: $\mu = 4.15 \times 10^{-3}$ and $\sigma = 1.21 \times 10^{-3}$, with $\lambda = 72.22$, corresponding to $R_1 = 1.39 \times 10^{-2}$, chosen so that R_1 lies eight standard deviations above the mean, with R_2 four standard deviations above the mean, and R_3 approximately two standard deviations above the mean. The nucleation rate is set to 3.5×10^8 nucleations per unit time. Throughout the full simulation, approximately 4.4 million grains are nucleated, but most do not survive.

The values $\gamma = 0.5\, J/m^2$ and $\rho = 10\, MPa$ determine that the mean unrecrystallized grain size for this simulation is $\langle r_0 \rangle = 3.61\, \mu m$ and the mean recrystallized nucleus size is $\langle r_n \rangle = 0.015\, \mu m$. Thus the unrecrystallized grains are somewhat smaller than often seen in experiment, but within an order of magnitude of the proper size. From Equations (4.15) and (4.19), we predict that no nuclei should survive away from grain boundaries, and that 43.5% of surviving nuclei are predicted to fall along grain boundaries, with the remaining 56.5% at triple junctions. This prediction is borne out well by Figure 4.19, though it is difficult to tell whether some surviving nuclei were touching grain boundaries at the time of nucleation. Further, we calculate $\mathbb{P}(G) \approx 4.13 \times 10^{-6}$. With 4.4 million total nucleations, the basic analysis of Section 4.2.3 predicts that approximately 18 of the nuclei will survive. Although our analysis in Section 4.2.3 does not account for continuous nucleation in any way — in particular, the changing proportion of grain boundaries in the simulation domain D is unaccounted for — and yet agrees quite well with the simulation result, in which there are 26 grains present when nucleation completes.

The final microstructure seen in Figure 4.19 is quite different than that seen in

Figure 4.15, where the simulations took place under site-saturated nucleation. There are far fewer survivors due to the differing parameter choices. The surviving grains tend to be more equiaxed in this simulation because the density of surviving nuclei along grain boundaries is much lower. Final recrystallized grain sizes vary greatly in both simulations, but the mechanisms behind this variation differ. In the site-saturated case, the variation is due to the variation in times when impingement occurs between recrystallizing grains along the pre-existing grain boundary. In the continuous case, the variation is explained primarily by the different times at which the surviving nuclei were nucleated.

Figure 4.20 demonstrates the evolution of the recrystallized area fraction F through time. The Avrami plot in Figure 4.20(b) clearly shows a long transition period before the expected Avrami exponent, 3, emerges. In this case, the initial increase in the plot is because nuclei are being added to the system (increasing F at a constant rate) faster than the nuclei present disappear due to surface tension effects (decreasing F at a rate approximately proportional to the number of nuclei present), until a sufficient number of nuclei are present for these competing effects to find an equilibrium. F remains approximately constant from $t = 5 \times 10^{-5}$ to $t = 7.5 \times 10^{-4}$. Only after a few nuclei successfully begin to grow does the Avrami exponent achieve the predicted value.

4.4.2 Three-Dimensional Recrystallization

In three dimensions, our simulation begins with 216 unrecrystallized grains. The domain is $\Omega = [0, 9.67]^3$, discretized on a $256 \times 256 \times 256$ grid, $\lambda = 12.407$, and the final time for the simulation is $t = 0.1713$. Spherical recrystallized grains are nucleated with normally distributed radii, with mean $\langle r_n \rangle = 0.0378$ and standard deviation $\sigma_n = 0.0094$. 243,872 nuclei are placed in the simulation domain D.

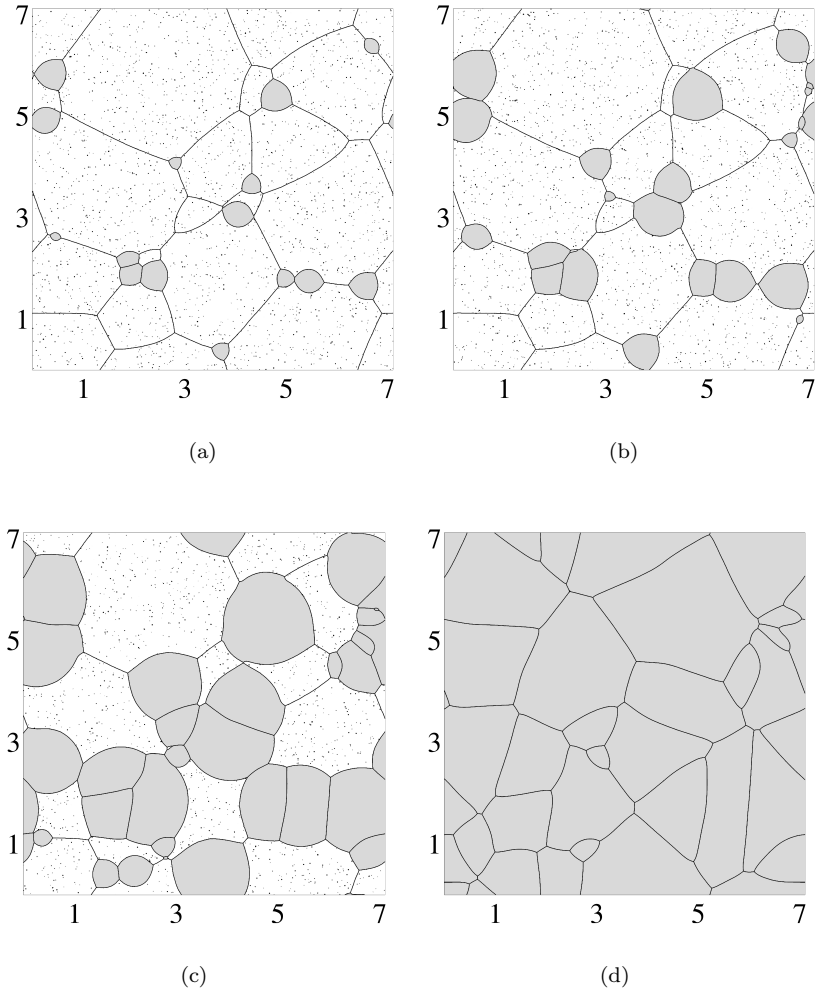

Figure 4.19: Microstructure from two-dimensional simulation with continuous nucleation. (a) At $t = 4.55 \times 10^{-3}$, with $F = 0.05$. All growing nuclei are located along grain boundaries or at triple junctions, as predicted. Many tiny nuclei can be seen throughout the microstructure. These nuclei have recently been nucleated but are not large enough to survive. (b) $F = 0.15$ at $t = 7.07 \times 10^{-3}$. Four new nuclei have successfully initiated visible growth since (a). All are quite small relative to the recrystallized grains that were also present in (a). (c) $F = 0.50$ at $t = 1.25 \times 10^{-2}$. Successful nuclei are of a wide variety of sizes, due to their varying nucleation times. Compare to Figure 4.15(b), where the nucleated grains are much closer in size, and size differences appear to be primarily due to impingement. (d) Recrystallization is complete at $t = 2.92 \times 10^{-2}$. The resultant grains are of a wide variety of sizes and shapes due to inhomogeneities in nucleation locations and varying nucleation times.

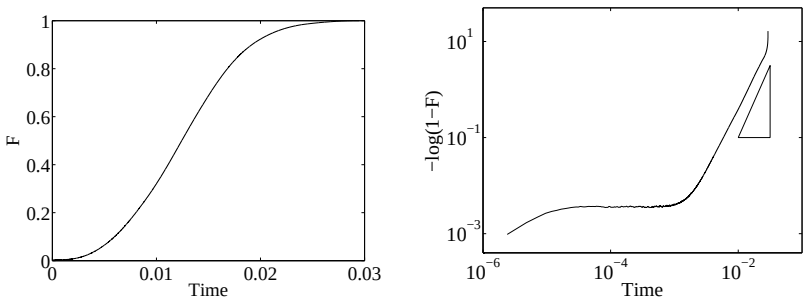

(a) (b)

Figure 4.20: (a) The recrystallized area fraction F evolves sigmoidally as expected for the large-scale simulation of continuous nucleation in two dimensions. (b) The Avrami plot shows a long initial transition period in which nuclei are continuously placed in the microstructure but disappear at the same rate due to their small sizes and corresponding high curvatures. The expected Avrami exponent, 3, is seen at later times.

In this case, taking the physically relevant parameter choices $\gamma = 0.5\,J/m^2$ and $\rho = 10\,MPa$, we find that the mean unrecrystallized grain radius is $0.62\,\mu m$ and the mean recrystallized grain radius is $0.0234\,\mu m$. The mean unrecrystallized grain radius is unphysically small. A significantly larger grid and the attendant memory requirements would be necessary to simulate three-dimensional recrystallization for this many (approximately 200) physically realistic unrecrystallized grains while maintaining the unrecrystallized nucleus size.

Just as in two dimensions, the three-dimensional simulations agree well with the JMAK predictions, as shown in Figure 4.21. In three dimensions, the predicted Avrami slope is 3 for site-saturated nucleation. Figure 4.22 shows the evolution of the microstructure as evolution progresses. At $t = 5.02 \times 10^{-2}$, recrystallization is 10% complete. The surviving recrystallized grains are still much smaller on average than the unrecrystallized grains. 50% recrystallization occurs at $t = 8.45 \times 10^{-2}$. By this time, there are fewer surviving recrystallizing grains (158) than unrecrystallized grains (216), so the recrystallizing grains are slightly larger on average at 50%

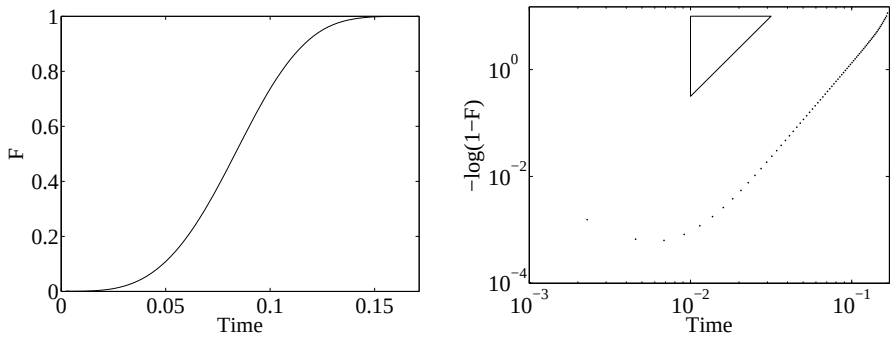

(a) (b)

Figure 4.21: Recrystallized volume fraction F and Avrami plot for three-dimensional site saturated nucleation. (a) F evolves sigmoidally in time, as expected. (b) The Avrami plot is approximately linear throughout the bulk of the evolution and demonstrates the expected slope of 3 for site-saturated homogeneous nucleation in three dimensions.

recrystallization. At all stages of the evolution, the recrystallizing grains are visibly faceted, consistent with the Herring angle condition even though as before surface tension is negligible compared to bulk energy along the faces of the recrystallizing grains by the time they have grown to be comparable to the length scale of the initial grain network.

Figure 4.23 compares the evolution of mean grain volume and mean number of faces for recrystallized and unrecrystallized grains through time. Early in the evolution, the recrystallizing grains are very small and have few faces as compared to the unrecrystallized grains. The bulk energy term allows some of the recrystallization nuclei to grow despite their small size and low number of faces. It is demonstrated in Section 3.2.4 that, for normal grain growth, a grain with few faces is likely to be a shrinking grain, in agreement with the inexact three-dimensional extension of the von Neumann–Mullins prediction given in [64].

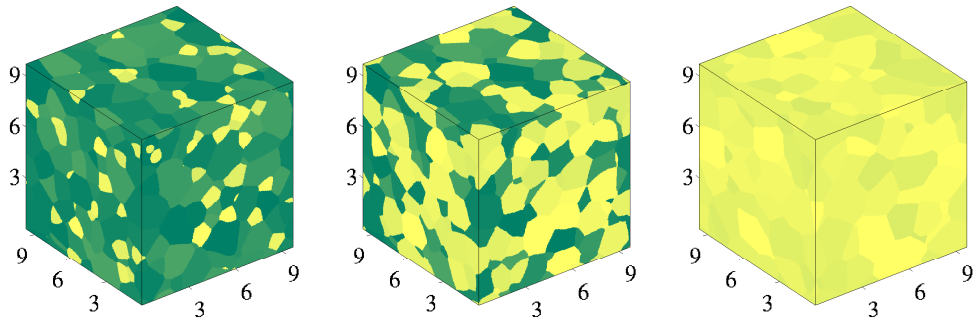

(a)

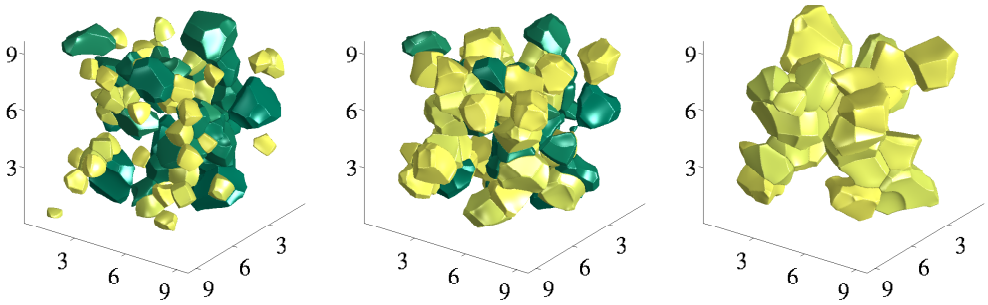

(b)

Figure 4.22: (a) Surface planes at $F = 0.1$, $F = 0.5$, and $F = 1$, respectively. Recrystallizing grains are shown in shades of yellow, unrecrystallized grains in shades of green. (b) Subsets of grains are shown at the same points in the evolution. Note that recrystallizing grains are clearly faceted, and that at early times, recrystallizing grains appear to have fewer faces on average than the unrecrystallized grains.

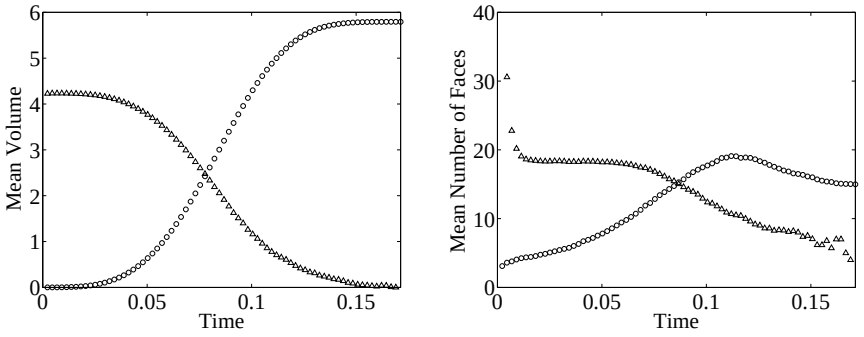

(a) (b)

Figure 4.23: (a) Mean volume of recrystallized grains (circles) and of unrecrystallized grains (triangles) through time. (b) Mean number of faces among recrystallized (circles) and unrecrystallized (triangles) grains through time. Early in the evolution, recrystallized grains are quite small and are likely to meet less grains than the larger unrecrystallized grains. The bulk energy evolution causes the recrystallized grains to grow on average despite their smaller sizes and numbers of neighbors until the situation is reversed at later times.

4.5 Discussion

We apply the algorithm developed in [19, 22] based on diffusion generated motion of signed distance functions to simulations of recrystallization in two and three dimensions. The use of this algorithm allows for fully-resolved simulations of the PDE-based version of the recrystallization model introduced in the seminal works of Srolovitz et al. [79, 80]. Due to the computational efficiency and subgrid resolution of this algorithm, we obtained previously unseen levels of detail in our simulations. This detail allows for the identification of some numerical artifacts in the Monte Carlo simulations of [79, 80], and thus for separation of these artifacts from features inherent to the model.

Section 4.2 presents new analysis of the model. In particular, it is shown that surface tension effects are *always* important, even when the surface tension is vanishingly small in comparison to the bulk energy driving force. It is demonstrated that

our algorithm capably captures the $O(1)$ effect described even for vanishingly small surface tensions and displays good agreement with the classification of parameter regimes presented here.

New simulations of recrystallization under this model are presented, with physically-relevant parameter choices. These parameter regimes could not be approached via the standard Monte Carlo method. For certain parameter choices in this range, we obtain microstructures at the conclusion of recrystallization composed primarily of extremely elongated grains. A simulation of three-dimensional grain growth is also presented. Though computational constraints prevent this simulation from taking physically-relevant parameters, good agreement with JMAK predictions is still obtained.

CHAPTER V

Conclusion

This dissertation extends, implements, and utilizes a class of algorithms for simulating multiphase motions with interfacial normal velocities of the form (1.1) and the natural Herring angle conditions (1.9) and (1.10) at triple junctions. These algorithms are collectively known as the "distance function-based diffusion-generated motion" (DFDGM) algorithms. Major advantages of the DFDGM algorithms are listed here, and discussed more completely next.

- Interfaces are implicitly represented, allowing topological changes to be handled naturally.
- The algorithms are absolutely stable, making accuracy the only constraint on the choice of the discrete time step Δt.
- DFDGM algorithms are highly accurate on uniform grids.
- The efficiency of the algorithms allows for very large simulations in both two and three dimensions to be performed.

The interfaces $\Gamma_{k\ell}$ are implicitly represented as the zero-level set of signed distance functions by the DFDGM algorithms, allowing topological changes (triple junction collisions and phase disappearance events, for example) to be handled naturally,

unlike explicit, front tracking-type methods. This is a sharp representation of the interface, unlike phase field methods, which have a diffuse boundary layer representing the interface. This diffuse boundary layer must be resolved by the discretized grid, limiting the scale of simulations possible via phase field methods.

The absolute stability of the DFDGM algorithms is inherited from the close connection between the DFDGM algorithms and the threshold dynamics scheme of Merriman, Bence, and Osher [59, 60], and is a major advantage over phase field and level set schemes. Large time steps Δt may be taken, with accuracy as the only concern. Front tracking, level sets, and phase field methods will all become numerically unstable if too large of time steps (with respect to the spatial discretization) are taken with typical standard time discretization methods.

The use of the signed distance function in the DFDGM algorithms allows for much greater accuracy than the threshold dynamics scheme is capable of, due to the subgrid accuracy that can be achieved by interpolating the value of the signed distance function. Interpolation is not possible in the threshold dynamics scheme due to the lack of continuity of the characteristic function. Furthermore, careful numerical convergence tests presented in Chapter II suggest the convergence of the algorithms to exact solutions where these are known (particularly, away from topological events), and also demonstrate the accuracy of the algorithm on small, uniform grids. The computational complexity of the DFDGM algorithms for isotropic grain growth and recrystallization is just $O(M \log M)$ per time step, where M is the total number of grid points used. This is the same as the threshold dynamics scheme; the scaling of the computational complexity is not affected by the use of signed distance functions and the need to perform redistancing operations. The accuracy and efficiency of the algorithms and the efficient parallel implementation of the algorithms allows for very

large simulations in the context of grain growth and recrystallization to be performed in both two and three dimensions.

Beyond the development and verification of the DFDGM algorithms, a second major contribution of this work is the application of these algorithms to large-scale simulations of isotropic grain growth and recrystallization. These important materials science phenomena are simulated using Algorithms 2.1 and 2.3, respectively. The simulation results are discussed in great depth in Chapters III and IV. Good agreement is seen with theoretical predictions, experimental results, and, where applicable, prior simulations.

The well-resolved three-dimensional simulation of isotropic grain growth presented is considerably larger than any other that we are aware of. Visually, the resulting microstructure compares well with real polycrystalline grains. We verify that the grain size distribution function is self-similar through time, and that the mean grain size scales with time as expected. The self-similar grain size distribution is shown to match well with the Rios distribution [70], a modification of the Hillert distribution [39]. Topological measures, including the number of faces, edges and corners per grain, are computed and compared to various simulations, models, and experimental results.

The work on the recrystallization model of Srolovitz, et al. [79,80] combines analytical results with simulation. We separate characteristics of the model from numerical artifacts contained in previous simulations and demonstrate the ability of Algorithm 2.3 to perform simulations displaying the correct model properties. We also present results of a large-scale two-dimensional simulation of recrystallization featuring a previously unseen microstructure containing primarily very elongated grains.

An important step towards the full model for anisotropic grain growth is the unequal surface tension case, with normal velocity given by (1.7). The full model allows the surface tension $\gamma_{k\ell}$ to vary spatially, for example, depending on the direction of the local unit normal vector to the interface $\Gamma_{k\ell}$. In this work, we present Algorithm 2.4 and numerical results suggesting the convergence of this algorithm in the special case where the surface tensions are additive (2.17). A possible extension of Algorithm 2.4 to the general unequal surface tension case is presented as Algorithm 2.5, though there is much work yet to be done in verifying this algorithm.

As a whole, the work presented in this dissertation clearly demonstrates the utility of the DFDGM algorithms for motions of the type described by (1.1). These algorithms are demonstrated to be accurate and very efficient. They have been applied with great success to simulations of isotropic grain growth and recrystallization. A matter of ongoing work is the extension of this class of algorithms to simulations of grain growth with unequal surface tensions.

BIBLIOGRAPHY

BIBLIOGRAPHY

[1] Aboav, D. A. The arrangement of grains in a polycrystal. *Metall. 3* (1970), 383–390.

[2] Allen, S. M., and Cahn, J. W. A microscopic theory for antiphase boundary motion and its application to antiphase domain coarsening. *Acta Metall. 27* (1979), 1085–1095.

[3] Almgren, F., Taylor, J. E., and Wang, L. Curvature-driven flows: a variational approach. *SIAM J. Control Optim. 31*, 2 (1993), 387–437.

[4] Anderson, M. P., Grest, G. S., and Srolovitz, D. J. Computer simulation of normal grain growth in three dimensions. *Philos. Mag. B 59*, 3 (1989), 293–329.

[5] Anderson, M. P., Srolovitz, D. J., Grest, G. S., and Sahni, P. S. Computer simulation of grain growth — I. Kinetics. *Acta Metall. 32*, 5 (1984), 783–791.

[6] Avrami, M. Kinetics of phase change. I. General theory. *J. Chem. Phys. 7* (1939), 1103–1112.

[7] Avrami, M. Kinetics of phase change. II. Transformation-time relations for random distribution of nuclei. *J. Chem. Phys. 8* (1940), 212–224.

[8] Avrami, M. Kinetics of phase change. III. Granulation, phase change, and microstructure. *J. Chem. Phys. 9*, 2 (1941), 177–184.

[9] Beck, P. Interface migration in recrystallization. In *Metal Interfaces*, R. Brick, Ed. American Society for Metals, Cleveland, 1952, pp. 208–247.

[10] Bernacki, M., Resk, H., Coupez, T., and Logé, R. E. Finite element model of primary recrystallization in polycrystalline aggregates using a level set framework. *Model. Simul. Mater. Sci. Eng. 17* (2009), 064006.

[11] Burke, J. E., and Turnbull, D. Recrystallization and grain growth. *Prog. Met. Phys. 3* (1952), 220–292.

[12] Cahn, J. W. The significance of average mean curvature and its determination by quantitative metallography. *Trans. Metall. Soc. AIME 239* (1967), 610–616.

[13] Carabello, D. G. *A variational scheme for the evolution of polycrystals by curvature*. PhD thesis, Princeton University, 1997.

[14] Christian, J. W. *Theory of transformations in metals and alloys*, 2 ed. Pergamon, Oxford, 1975. Page 542.

[15] Desch, C. H. The solidification of metals from the liquid state. *J. Inst. Metals 22*, 2 (1919), 241–276.

[16] Detert, K. Secondary recrystallization. In *Recrystallization of Metallic Materials*, F. Haessner, Ed. Riederer Verlag, Stuttgart, 1978, p. 97.

[17] Doherty, R. D., Hughes, D. A., Humphreys, F. J., Jonas, J. J., Jensen, D. J., Kassner, M. E., King, W. E., McNelley, T. R., McQueen, H. J., and Rollett, A. D. Current issues in recrystallization: a review. *Mater. Sci. Eng. A238* (1997), 219–274.

[18] Edwards, S. F., and Pithia, K. D. A note on the Aboav–Weaire law. *Phys. A 205* (1994), 577–584.

[19] Elsey, M., Esedoḡlu, S., and Smereka, P. Diffusion generated motion for grain growth in two and three dimensions. *J. Comp. Phys. 228*, 21 (2009), 8015–8033.

[20] Elsey, M., Esedoḡlu, S., and Smereka, P. Large scale simulation of normal grain growth via diffusion generated motion. *Proc. R. Soc. Lond. A 467* (2011), 381–401.

[21] Elsey, M., Esedoḡlu, S., and Smereka, P. Large scale simulations and parameter study for a simple model of recrystallization. To appear in *Phil. Mag.* (2011).

[22] Esedoḡlu, S., Ruuth, S., and Tsai, R. Diffusion generated motion using signed distance functions. *J. Comp. Phys. 229*, 4 (2010), 1017–1042.

[23] Esedoḡlu, S., and Smereka, P. A variational formulation for a level set representation of multiphase flow and area preserving curvature flow. *Commun. Math. Sci. 6*, 1 (2008), 125–148.

[24] Fan, D., and Chen, L.-Q. Computer simulation of grain growth using a continuum field model. *Acta Mater. 45*, 2 (1997), 611–622.

[25] Fayad, W., Thompson, C. V., and Frost, H. J. Steady-state grain-size distributions resulting from grain growth in two dimensions. *Scr. Mater. 40*, 10 (1999), 1199–1204.

[26] Feltham, P. Grain growth in metals. *Acta Metall. 5* (1957), 97–105.

[27] Fjeldberg, E., and Marthinsen, K. Computer simulations of kinetics and texture of recrystallisation by a 3-D Potts Monte Carlo model. *Mater. Sci. Forum 558–559* (2007), 1069–1074.

[28] Fradkov, V. E., Kravchenko, A. S., and Shvindlerman, L. S. Experimental investigation of normal grain growth in terms of area and topological class. *Scr. Metall. 19*, 11 (1985), 1291–1296.

[29] Fradkov, V. E., Shvindlerman, L. S., and Udler, D. G. Computer simulation of grain growth in two dimensions. *Scr. Metall. 19*, 11 (1985), 1285–1290.

[30] Garcke, H., Nestler, B., and Stoth, B. A multiphase field concept: Numerical simulations of moving phase boundaries and multiple junctions. *SIAM J. Appl. Math. 60*, 1 (1999), 295–315.

[31] Gilbert, E. N. Random subdivisions of space into crystals. *Ann. Math. Stat. 33*, 3 (1962), 958–972.

[32] Glicksman, M. E., Rios, P. R., and Lewis, D. J. Mean width and caliper characteristics of network polyhedra. *Philos. Mag. 89*, 4 (2009), 389–403.

[33] Gottstein, G., and Shvindlerman, L. *Grain Boundary Migration in Metals.* CRC Press, Boca Raton, Florida, 1999. Page 130.

[34] Grayson, M. A. The heat equation shrinks embedded plane curves to points. *J. Differ. Geom. 26* (1987), 285–314.

[35] Harker, D., and Parker, E. Grain shape and grain growth. *Trans. Am. Soc. Met. 34* (1945), 156–201.

[36] Herring, C. Surface tension as a motivation for sintering. In *The Physics of Powder Metallurgy*, W. Kingston, Ed. McGraw–Hill, New York, 1951, pp. 143–179.

[37] Hesselbarth, H. W., and Göbel, I. R. Simulation of recrystallization by cellular automata. *Acta Metall. Mater. 39*, 9 (1991), 2135–2143.

[38] Hilgenfeldt, S., Kraynik, A. M., Koehler, S. A., and Stone, H. A. An accurate von Neumann's law for three-dimensional foams. *Phys. Rev. Lett. 86*, 12 (2001), 2685–2688.

[39] Hillert, M. On the theory of normal and abnormal grain growth. *Acta Metall. 13* (1965), 227–238.

[40] Hull, F. C. Plane section and spatial characteristics of equiaxed β-brass grains. *Mater. Sci. Technol. 4* (1988), 778–785.

[41] Humphreys, F. J., and Hatherly, M. *Recrystallization and Related Annealing Phenomena*, 1 ed. Pergamon, Oxford, 1995. (pages 8, 316, 422).

[42] Hurley, P. J., and Humphreys, F. J. Modelling the recrystallization of single-phase aluminum. *Acta Mater. 51* (2003), 3779–3793.

[43] Janssens, K. G. F., Raabe, D., Kozeschnik, E., Miodownik, M. A., and Nestler, B. *Computational Materials Engineering*. Elsevier, London, 2007.

[44] Johnson, W. A., and Mehl, R. F. Reaction kinetics in processes of nucleation and growth. *Trans. Am. Inst. Min. Metall. Eng. 135* (1939), 416–442.

[45] Kawasaki, K., Nagai, T., and Nakashime, K. Vertex models for two-dimensional grain growth. *Philos. Mag. B 60*, 3 (1989), 399–421.

[46] Kelvin, W. T. On the division of space with minimum partitional area. *Philos. Mag. 24*, 151 (1887), 503–514.

[47] Kim, S. G., Kim, D. I., Kim, W. T., and Park, Y. B. Computer simulations of two-dimensional and three-dimensional ideal grain growth. *Phys. Rev. E 74* (2006), 061605.

[48] Kinderlehrer, D., Lee, J., Livshits, I., Rollett, A., and Ta'asan, S. Mesoscale simulation of grain growth. *Mater. Sci. Forum 467–470* (2004), 1057–1062.

[49] Kinderlehrer, D., Livshits, I., and Ta'asan, S. A variational approach to modeling and simulation of grain growth. *SIAM J. Sci. Comput. 28*, 5 (2006), 1694–1715.

[50] Kolmogorov, A. N. On the statistical theory of crystallization in metals. *Bull. Acad. Sci. USSR. Ser. Math. 3* (1937), 367–368.

[51] Krill III, C. E., and Chen, L.-Q. Computer simulation of 3-D grain growth using a phase-field model. *Acta Mater. 50* (2002), 3057–3073.

[52] Liu, G., Yu, H., Song, X., and Qin, X. A new model of three-dimensional grain growth: theory and computer simulation of topology-dependency of individual grain growth rate. *Mater. Des. 22* (2001), 33–38.

[53] Louat, N. P. On the theory of normal grain growth. *Acta Metall. 22* (1974), 721–724.

[54] MacPherson, R., and Srolovitz, D. The von Neumann relation generalized to coarsening of three-dimensional microstructures. *Nature 446* (2007), 1053–1055.

[55] Mantegazza, C., Novaga, M., and Tortorelli, V. M. Motion by curvature of planar networks. *Ann. Scuola Norm. Super. Pisa–Cl. Sci. 3*, 2 (2004), 235–324.

[56] Marx, V., Reher, F. R., and Gottstein, G. Simulation of primary recrystallization using a modified three-dimensional cellular automaton. *Acta Mater. 47*, 4 (1999), 1219–1230.

[57] Mascarenhas, P. Diffusion generated motion by mean curvature. Tech. rep., UCLA, 1992. CAM Report 92–33.

[58] Meijering, J. L. Interface area, edge length, and number of vertices in crystal aggregates with random nucleation. *Phillips Res. Rep. 8* (1953), 270–290.

[59] Merriman, B., Bence, J. K., and Osher, S. Diffusion generated motion by mean curvature. In *The Computational Crystal Growers Workshop* (1993), J. Taylor, Ed., Am. Math. Soc., pp. 73–83.

[60] Merriman, B., Bence, J. K., and Osher, S. Motion of multiple junctions: a level set approach. *J. Comput. Phys. 112*, 2 (1994), 334–363.

[61] Modica, L. The gradient theory of phase transitions and the minimal interface criterion. *Arch. Ration. Mech. Anal. 98*, 2 (1987), 123–142.

[62] Modica, L., and Mortola, S. Un esempio di γ-convergenza. *Boll. Un. Mat. Ital. 5*, 14–B (1977), 285–299.

[63] Mullins, W. W. Two-dimensional motion of idealized grain boundaries. *J. Appl. Phys. 27*, 6 (1956), 900–904.

[64] Mullins, W. W. Estimation of the geometrical rate constant in idealized three dimensional grain growth. *Acta Metall. 37*, 11 (1989), 2979–2984.

[65] Raabe, D. Cellular automata in materials science with particular reference to recrystallization simulation. *Annu. Rev. Mater. Res. 32* (2002), 53–76.

[66] Radhakrishnan, B., Sarma, G. B., Weiland, H., and Baggethun, P. Simulations of deformation and recrystallization of single crystals of aluminhum containing hard particles. *Modelling Simul. Mater. Sci. Eng. 8*, 5 (2000), 737–750.

[67] Radhakrishnan, B., Sarma, G. B., and Zacharia, T. Modeling the kinetics and microstructural evolution during static recrystallization — Monte Carlo simulation of recrystallization. *Acta Mater. 46*, 12 (1998), 4415–4433.

[68] Reitich, F., and Soner, H. M. Three-phase boundary motion under constant velocities. I: The vanishing surface tension limit. *Proc. R. Soc. Edin. 126A* (1996), 837–865.

[69] Rhines, F. R., and Patterson, B. R. Effect of the degree of prior cold work on the grain volume distribution and the rate of grain growth of recrystallized aluminum. *Metall. Trans. A 13* (1982), 985–993.

[70] Rios, P. R., Dalpian, T. G., Brandão, V. S., Castro, J. A., and Oliveira, A. C. L. Comparison of analytical grain size distributions with three-dimensional computer simulations and experimental data. *Scr. Mater. 54* (2006), 1633–1637.

[71] Rollett, A. D., and Raabe, D. A hybrid model for mesoscopic simulation of recrystallization. *Comput. Mater. Sci. 21* (2001), 69–78.

[72] Russo, G., and Smereka, P. A remark on computing distance functions. *J. Comput. Phys. 163* (2000), 51–67.

[73] Ruuth, S. J. Efficient algorithms for diffusion-generated motion by mean curvature. *J. Comput. Phys. 144* (1998), 603–625.

[74] Sahni, P. S., Srolovitz, D. J., Grest, G. S., Anderson, M. P., and Safran, S. A. Kinetics of ordering in two dimensions. II. quenched systems. *Phys. Rev. B 28*, 5 (1983), 2705–2717.

[75] Smereka, P. The numerical approximation of a delta function with application to level set methods. *J. Comput. Phys 211*, 1 (2006), 77–90.

[76] Smith, C. S. Grain shapes and other metallurgical applications of topology. In *Metal Interfaces*, R. Brick, Ed. American Society for Metals, Cleveland, 1952, pp. 65–108.

[77] Smith, C. S. Some elementary principles of polycrystalline microstructure. *Met. Rev. 9*, 33 (1964), 1–48.

[78] Srolovitz, D. J., Grest, G. S., and Anderson, M. P. Computer simulation of grain growth — V. Abnormal grain growth. *Acta Metall. 33*, 12 (1985), 2233–2247.

[79] Srolovitz, D. J., Grest, G. S., and Anderson, M. P. Computer simulation of recrystallization — I. Homogeneous nucleation and growth. *Acta Metall. 34*, 9 (1986), 1833–1845.

[80] Srolovitz, D. J., Grest, G. S., Anderson, M. P., and Rollett, A. D. Computer simulation of recrystallization — II. Heterogeneous nucleation and growth. *Acta Metall. 36*, 8 (1988), 2115–2128.

[81] Suwa, Y., Saito, Y., and Onodera, H. Parallel computer simulation of three-dimensional grain growth using the multi-phase-field model. *Mater. Trans. 49*, 4 (2008), 704–709.

[82] Taylor, J. E. The motion of multiple-phase junctions under prescribed phase-boundary velocities. *J. Differ. Equ. 119* (1995), 109–136.

[83] Taylor, J. E. A variational approach to crystalline triple-junction motion. *J. Stat. Phys. 95*, 5–6 (1999), 1221–1244.

[84] Thompson, C. V., Frost, H. J., and Spaepen, F. The relative rates of secondary and normal grain growth. *Acta Metall. 35*, 4 (1987), 887–890.

[85] Tsai, Y.-H. R., Cheng, L.-T., Osher, S., and Zhao, H.-K. Fast sweeping algorithms for a class of hamilton–jacobi equations. *SIAM J. Numer. Anal. 41*, 2 (2003), 673–694.

[86] von Neumann, J. Written discussion. In *Metal Interfaces*, R. Brick, Ed. American Society for Metals, Cleveland, 1952, pp. 108–110.

[87] Wakai, F., Enomoto, N., and Ogawa, H. Three-dimensional microstructural evolution in ideal grain growth — general statistics. *Acta Mater. 48* (2000), 1297–1311.

[88] Wakai, F., Shinoda, Y., Ishihara, S., and Dominguez-Rodriguez, A. Topological transformation of grains in three-dimensional normal grain growth. *J. Mater. Res. 16* (2001), 2136–2142.

[89] Weaire, D. Some remarks on the arrangement of grains in a polycrystal. *Metall. 7* (1974), 157–160.

[90] Weaire, D., and Glazier, J. A. Relation between volume, number of faces and three-dimensional growth laws in coarsening cellular patterns. *Philos. Mag. Lett. 68*, 6 (1993), 363–365.

[91] Weygand, D., and Bréchet, Y. Three-dimensional grain growth: a vertex dynamics simulation. *Philos. Mag. B 79*, 5 (1999), 703–716.

[92] Williams, R. E. Space-filling polyhedron: Its relation to aggregates of soap bubbles, plant cells, and metal crystallites. *Science 161*, 3838 (1968), 276–277.

[93] Williams, W. M., and Smith, C. S. A study of grain shape in an aluminum alloy and other applications of stereoscopic microradiography. *Trans. Am. Inst. Min. Met. Eng. 194* (1952), 755–765.

[94] Zhang, C., Suzuki, A., Ishimaru, T., and Enomoto, M. Characterization of three-dimensional grain structure in polycrystalline iron by serial sectioning. *Metall. Mater. Trans. A 35A* (2004), 1927–1933.

[95] Zhao, H.-K. A fast sweeping method for Eikonal equations. *Math. Comput. 74*, 250 (2004), 603–627.

[96] Zhao, H.-K., Chan, T., Merriman, B., and Osher, S. A variational level set approach to multiphase motion. *J. Comput. Phys. 127* (1996), 179–195.